FERROELECTRIC MICROWAVE CIRCUITS

by

LEONG CHING CHENG

A thesis submitted to the University of Birmingham for the degree of
DOCTOR OF PHILOSOPHY

School of Electronic, Electrical and Computer Engineering
College of Engineering and Physical Sciences
The University of Birmingham
June 2009

UNIVERSITY OF
BIRMINGHAM

University of Birmingham Research Archive

e-theses repository

This unpublished thesis/dissertation is copyright of the author and/or third parties. The intellectual property rights of the author or third parties in respect of this work are as defined by The Copyright Designs and Patents Act 1988 or as modified by any successor legislation.

Any use made of information contained in this thesis/dissertation must be in accordance with that legislation and must be properly acknowledged. Further distribution or reproduction in any format is prohibited without the permission of the copyright holder.

ABSTRACT

Ferroelectric materials have been found to be particularly attractive materials for the development of tunable microwave devices over the past few decades due to their distinctive characteristic that is the variation of dielectric constant as a function of electric field. In this research project, the work on how the finite difference method (FDM), a computational technique, is modified to suit the evaluation of the cross-sectional field distribution of a ferroelectric-based transmission line is presented and the results are verified. The modified FDM was employed for determining the effective dielectric constant (ε_{eff}) and the characteristic impedance (Z_o) of ferroelectric-based structures where the spatial variation of dielectric constant was taken into consideration.

A significant portion of this research is focused on the application of ferroelectric materials in designing tunable microwave devices. Two optimised phase shifters incorporating Barium Strontium Titanate ($Ba_{0.5}Sr_{0.5}TiO_3$ or BST) ferroelectric thin-films are designed, fabricated and measured. One is based on simple coplanar waveguide (CPW) transmission line, and another is based on tapered CPW structure.

To date, no work on tunable attenuator using ferroelectric materials has ever been reported, as contrary to other extensively studied ferroelectric-based tunable microwave devices, namely tunable resonators, filters, and phase shifters. In this work, a novel design of tunable attenuator integrating BST thin-films is presented and verified with experimental results from a similar design of tunable attenuator based on Roger/Duroid 6010LM substrate of dielectric constant 10.2. The application of ferroelectric thin-films enables continuous variation of attenuation under controlled bias voltages with significant size and weight reduction in the overall device.

To my mum and dad for their endless love and support…

ACKNOWLEDGEMENT

First and foremost, I would like to express my gratitude to my supervisor, Prof. Michael J. Lancaster for his help, support, guidance and encouragement over the course of my PhD work. His enlightening ideas and passions have greatly inspired me.

I would also like to thank my fellow colleagues in Emerging Device Technology Research Centre. It has been a real honour working with them. I take this opportunity to thank Dr. Phe Suherman, Dr. Yi Wang, Dr. Kenneth Yeo for their advices and stimulating discussions on numerous occasions; Donna Holdom, Cliff Ansell and Dr. Peng Bao for their technical support in device fabrication. A special thanks to my good friend, Dr. Sein Leung Soo, for his comments and corrections on this dissertation.

A huge appreciation to both scholarship bodies: Engineering and Physical Sciences Research Council (EPSRC) scholarship and the Engineering School scholarship of the University of Birmingham. Their financial supports have allowed my dream in pursuing a PhD degree to come true.

Last but not least, an utmost gratitude to my family and friends, both near and far, who have kept me in their thoughts and prayers. Their endless love, patience, encouragement and support have kept me going strong and well throughout my stay in UK.

TABLE OF CONTENTS

LIST OF FIGURES

LIST OF SYMBOLS

C	capacitance
R	resistance
L	inductance
ε_r	relative dielectric constant
ε_{eff}	effective dielectric constant
μ_0	permeability of free space
c_0	speed of light in free space
E	electric field
n	tunability
n_r	relative tunability
tan δ	dielectric loss tangent
Q	quality factor
K	commutation quality factor
Z_c	characteristic impedance
FoM	figure-of-merit
$\Delta\Phi$	differential phase shift
$K(k)$	complete elliptic integral of the first kind
w	strip width
g	gap width of a coplanar line
s	half width of a coplanar line centre strip
GW	in-plane ground width of a coplanar line
h	substrate thickness
t	conductor thickness
σ	conductivity
α_c	attenuation due to conductor loss
α_d	attenuation due to dielectric loss
α_r	attenuation due to radiation loss
R_s	surface resistance
δ	skin depth
ω	angular frequency
γ	complex propagation constant
β	phase constant

LIST OF ABBREVIATIONS

Al_2O_3	alumina (sapphire)
Au	gold
Ba	barium
BST	barium strontium titanate
BTO	barium titanate
CBCPW	conductor-backed coplanar waveguide
CPW	coplanar waveguide
Cu	copper
DC	direct current
EM	electromagnetic
FDM	finite difference method
FEM	finite element method
FET	field-effect transistors
GaAs	galium arsenide
HTS	high temperature superconductor
$LaAlO_3$	lanthanum aluminate
LRRM	load-reflect-reflect-match
MEMS	micro-electro-mechanical systems
MgO	magnesium oxide
MMIC	monolithic microwave integrated circuit
MSL	microstrip-like mode
PIN	positive intrinsic negative
PLD	pulse laser deposition
Q-factor	quality factor
RF	radio frequency
Si	silicon
S-parameters	scattering-parameters
Sr	strontium
STO	strontium titanate
TEM	transverse electromagnetic
Ti	titanium

Chapter 1

Introduction

1.1 Motivation

There has been rapid growth in communication systems including satellite, 3G wireless phones, ultra-wide band and optical networks over the last few decades. Numerous frequency standards have coexisted in different parts of the world, along with an increasingly congested spectrum in the microwave frequencies. Hence, in recent years, there has been an immense interest in developing frequency-agile microwave devices to allow multi-band or multi-bandwidth operation with little impact on the component count. The trend towards these frequency-agile applications often demands high-speed, light-weight, low-operation voltage, compact and miniaturised of devices at a lower cost with high tunability, low loss and low power consumption [1-4].

Ferroelectric materials have been found to be particularly important materials for the development of electrically tunable devices since the 1960s [5-7]. The change in the dielectric constant of ferroelectric materials as a function of electric field is the

key to a wide range of applications. Examples in the field of microwave engineering are tunable resonators, frequency-agile filters, varactors (also known as variable or tunable capacitors), variable power dividers/combiners, variable-frequency oscillators, delay lines and phase-shifters. The latter is the key component in phase-array antennas [8-11].

To the best of author's knowledge, to date, no work on tunable attenuators using ferroelectric materials has been done; where as other ferroelectric-based tunable microwave devices have been studied extensively. Hence, the main objective of this work is to present a novel tunable attenuator device based on Barium Strontium Titanate (BST) ferroelectric thin-film. Alongside this, work on how the finite difference method, a computational technique, is modified to suit the evaluation of the cross-sectional field distribution of a ferroelectrics-based transmission line will be presented.

1.2 Competing Technologies for Tunable Microwave Devices

Traditionally, tuning is done manually or mechanically. Fox [12] proposed the first manually adjustable waveguide phase shifter in 1946. Mechanical circuits are inexpensive, easy to fabricate and have very low loss with good power handling capability. However, they come in large sizes and have rather slow response speed and are therefore cumbersome. Today, many circuit technology options are available whose tunable performance is closely related to the choice of technology. These options essentially include semiconductors, micro-electro-mechanical systems (MEMS), ferrites and ferroelectric materials. The following section will briefly review these technologies and put emphasis on interesting possibilities offered by the use of ferroelectric thin-film materials.

1.2.1 Semiconductors

Semiconductor switching elements such as field-effect transistors (FET), positive intrinsic negative (PIN) diodes and varactor diodes were first introduced in tunable circuits in 1960s [13, 14] and are still the dominant devices for making tunable circuits [15-17]. Advantages they offer are their low cost and compactness and their faster switching speeds, in the order of tens to few hundreds of nanoseconds. In addition, they can be easily integrated with monolithic microwave integrated circuits (MMICs). The main drawback of semiconductors in tuning applications is their low quality factor at microwave frequencies and typically higher insertion loss. Moreover, semiconductors are highly non-linear and have a lower power handling capability. The non-linear response of semiconductors can be of great importance as it is the source of inter-modulation distortion [18].

1.2.2 MEMS

In the early 1990s, interest has emerged in micro-electro-mechanical systems (MEMS) where tunability is obtained by the physical movement of a component which usually changes the capacitance of the device. These devices use electrostatic [19, 20], piezoelectric [21] or thermal effects [22] to produce the movement. In general, MEMS devices offer considerable advantages over semiconductors in terms of performance, power handling capability and power consumption at the expense of slower switching speed. Typical switching speed is in the range of a few to tens of microseconds [23].

Despite a tremendous effort invested in the development of MEMS in the past few decades, the widespread use of MEMS has been impeded by the high cost of packaging and by reliability and lifetime testing issues. MEMS-based devices typically require hermetic packaging as the moving parts of the device tend to be very sensitive to the environmental conditions, such as air moisture, temperature and vibration [23, 24]. This significantly increases the cost over other technologies.

1.2.3 Ferrites

Another technology for making tunable microwave devices is the use of agile materials. Among them, ferrites have been found interesting for their change in permeability with an applied DC magnetic field. The first electronically variable ferrite phase shifter was reported in 1957 [25, 26]. Unfortunately, ferrite-based circuits are generally large, heavy, low switching speed and have high power consumption. In addition, tunable ferrite devices are difficult to integrate with planar circuits such as microstrip and stripline. Although ferrite-based devices are bulkier, their excellent tuning factor and power handling capability remain unsurpassed [25, 26]. The switching speed is in the order of tens of microseconds.

1.2.4 Ferroelectrics

Ferroelectric materials have been studied since the early 1960s in the field of microwave engineering [5-7]. However, it is only relatively recently that the applications in microwave devices are beginning to emerge. This recent renewed interest is due to the monolithically compatible processing of certain ferroelectric thin-film compounds with planar technologies [4, 27]. This has generated great interest and shows promise for the design of a new class of tunable microwave devices which could significantly reduce the cost of production. Contrary to ferrite devices, ferroelectric material-based devices take advantage of the property of the change in dielectric constant of ferroelectric material with an applied DC electric field. The dielectric constant and breakdown voltage of ferroelectric thin-films are intrinsically high, thus allowing increased miniaturisation and high power handling [2, 28]. Ferroelectric-based devices are tuned much faster than ferrite, semiconductors or MEMS type equivalents (< 1 ns) and have a near zero power consumption, but suffer from lower quality factor than MEMS [15, 24].

1.3 Comparison of Competing Technologies

Various technologies mentioned in the previous section have been used for many frequency-agile devices. All have their pros and cons. Therefore, the choice of technology strongly depends on the application, in terms of system specification, cost, ease of integration with other technologies and reliability. A comparison of various competing technologies in light of the parameters typically considered in system design, namely tunability, quality-factor (Q-factor), power consumption, switching time and power handling capability, is shown in Table 1.3.1. The entries reflect data from different literatures [15, 23, 24, 28-31], appropriate to general-purpose, continuously variable varactors and phase shifters, are suitable for microwave operation in a wide assortment of applications.

	Semicond.	**MEMS**	**Ferrite**	**Ferroelectric**
Tunability	High	Low	Very High	Moderate to High
Q-Factor	Moderate 30-60	Very High 100-1000	High 50-100	Moderate < 100
Power Consumption	Low < 10 mW[a] 0.05-0.1 mW[b]	Low << 1 μW	High ~10 W	Low << 1 μW
Switching Time	Fast 1-5 ns[a] 2-10 ns[b]	Slow 2-40 μs[c] 200-3000 μs[d]	Moderate 10-100 μs	Very Fast < 1 ns
Power Handling	High tens of watts	Low < 50 mW	Very High in kW	High > 1 W

Table 1.3.1: Comparison of various competing technologies [15, 23, 24, 28-31].
([a] PIN Diode; [b] FET; [c] Electrostatic type; [d] Thermal/magnetic type)

Ferroelectric materials are favoured for applications which require rapid, continuous tuning and low power consumption as they work using an electric field.

In addition, ferroelectric-based devices are extremely competitive in terms of cost, weight and size, in particular at millimetre wavelength, without a significant sacrifice in performance for many applications, hence making them an excellent candidate for low cost frequency-agile devices.

1.4 Thesis Overview

This thesis presents work done on a novel tunable attenuator device which based on a Barium Strontium Titanate ($Ba_{0.5}Sr_{0.5}TiO_3$ or BST) ferroelectric thin-film on a Magnesium Oxide (MgO) substrate. A number of contributions to the field have been made during the course of this work. To the best of author's knowledge, no work on tunable attenuators based on ferroelectric thin-films has been reported to date. The tunable attenuator in this work is realised into one integrated planar circuit. The properties of the ferroelectric materials (i.e. high dielectric constant) have allowed a significant reduction of device dimensions, weight and cost in mass production. Tunable attenuators has been previously designed using semiconductor tunable varactors in a cascade manner in order to achieve controlled attenuation in a similar piece of work [32]. However, the fabrication process was complicated and time consuming as the device required several layers of metallisation and substrates.

Ferroelectric materials have a non-linear dielectric constant which varies with the application of electric field and this is the key to many frequency-agile and tunable microwave devices. Chapter 2 reviews the fundamentals of ferroelectric materials and various methods of growing and characterisation techniques. This is followed by a brief survey of the ferroelectric-based frequency-agile devices reported in the literature.

Chapter 3 reviews various types of planar transmission lines, namely microstrip, coplanar waveguide (CPW) and conductor-backed coplanar waveguide (CBCPW). Crucial to circuit design, the closed form expression for the effective dielectric constant ε_{eff} and characteristic impedance Z_c of each geometry incorporated

with ferroelectric material is presented. These expressions are derived using conformal mapping techniques where a quasi-static TEM (transverse electromagnetic) mode of propagation along the line is assumed. This section is supported by Appendix A and B, which presents the approximations used in the conformal mapping techniques and the steps involved in deriving the associated conductor loss of CBCPW, respectively.

Chapter 4 discusses the work on how the finite difference method (FDM), a computational technique, is modified to suit the evaluation of the cross-sectional field distribution of a ferroelectric-based transmission line. The derivation of the modified FDM is presented, together with the comparison of modified FDM with present closed form expression in finding ε_{eff} and Z_c for various types of transmission line. A paper has been published [33] in regards to this chapter and can be found in Appendix C.

The fabrication and experimental measurement of CPW phase shifters which based on BST ferroelectric thin-films and MgO substrate are presented in Chapter 5. A DC bias voltage of up to 100 V is applied across the phase shifters which produced a phase shift of 105° at 20 GHz with an insertion loss of about 10.6 dB, giving a figure-of-merit of 14°/dB. The BST thin-films showed a tunability of ~48% at 3.13 $V/\mu m$. This work is carried out as a preliminary step towards using BST ferroelectric thin-films for designing CBCPW phase shifters, which are key components in the tunable attenuator described in Chapter 6. The design and the associated simulated response of CBCPW phase shifters are shown.

Chapter 6 presents the application of the BST ferroelectric phase shifter in a tunable attenuator. This novel topology of tunable attenuator that based on BST ferroelectric thin-films on an MgO substrate demonstrates a continuous variation of attenuation by appropriate control of DC bias voltage. A new design technique has been developed employing the principle of constructive and destructive interference by integrating two tunable phase shifters in parallel to produce attenuation of the signal. The simulation results of the BST tunable attenuator are shown.

In order to verify the simulation results as well as the validity of the operation principle of the BST tunable attenuator, a similar design of tunable attenuator which based on a dielectric substrate of dielectric constant 10.2 is designed and fabricated. The comparison of experimental and simulation results is shown.

Finally, Chapter 7 draws a close to this thesis with a summary and conclusions of the work done. The main findings and the limitations of this work are summarised. The application prospects of the presented tunable attenuator are addressed. Some suggestions of improvements and recommendations for future work are given.

1.5 Conclusions

In this introductory chapter, the motivation for this work was discussed. Various technologies in achieving frequency-agility in tunable microwave devices were reviewed and compared. Finally, an overview of the thesis was given. The next chapter presents the fundamentals of ferroelectric materials in terms of dielectric properties, various forms of ferroelectric materials and thin-film growing techniques. Literature on frequency-agile device using ferroelectric materials will also be discussed.

Chapter 2

Ferroelectric Materials and Tunable Microwave Devices

2.1 Introduction

Ferroelectrics have been studied since the early 1960s for application in microwave engineering [5-7]. The change in the dielectric constant of ferroelectrics as a function of applied electric field is the key to a wide range of applications. Examples in the field of microwave engineering include tunable resonators, frequency-agile filters, varactors, variable power dividers/combiners, variable-frequency oscillators, delay-lines and phase shifters. The latter is the key component in phase-array antennas.

Until very recently, ferroelectrics have been used in the form of bulk ceramics

and, where available, single crystals. The initial idea of utilising bulk ferroelectrics in tunable microwave devices was not very successful as very high voltage is required to achieve a usable tuning range [4, 34]. Furthermore, integration of bulk ferroelectrics in devices is cumbersome. Whilst these materials have proved a robust and reliable solution, producing thin layers or dimensional tolerances better than a few microns has proved impractical [27].

However, there has been a renewed interest in application of ferroelectrics for tunable microwave devices since the 1980s [35]. This resurgent interest is largely due to the advances in thin-film growth techniques and the ability to integrate ferroelectrics with semiconductor and ceramic technologies, and thereby dramatically reduce the cost of the devices.

2.2 Ferroelectric Materials

Ferroelectric materials belong to a class of perovskite oxide materials that exhibit a spontaneous electric polarisation below the Curie temperature T_c. Upon cooling, there is a transition from the paraelectric to the ferroelectric state at T_c, where the maximum dielectric constant is observed. At temperatures below T_c (i.e. in ferroelectric state), a spontaneous electric polarisation is present where there is a relative displacement of ions in ferroelectric materials; this results in a net dipole moment. The orientation of the dipole moment in a ferroelectric can be shifted from one orientation to another under the influence of an applied electric field, causing a change in the dielectric constant of the material [2, 15, 34, 36]. The relation between polarisation and applied electric field is represented by the hysteresis curve shown in Figure 2.2.1. In the ferroelectric state, the polarisation of ferroelectrics remains even in the absence of an applied electric field. In the paraelectric state, there is only polarisation with the application of an external electric field.

Examples of ferroelectric materials are Barium Titanate ($BaTiO_3$) and Barium Strontium Titanate ($Ba_xSr_{1-x}TiO_3$ or BST). Figure 2.2.2 shows the perovskite structure and electric polarisation of a unit cell BST (i.e. shifting of Ti atom) in response to

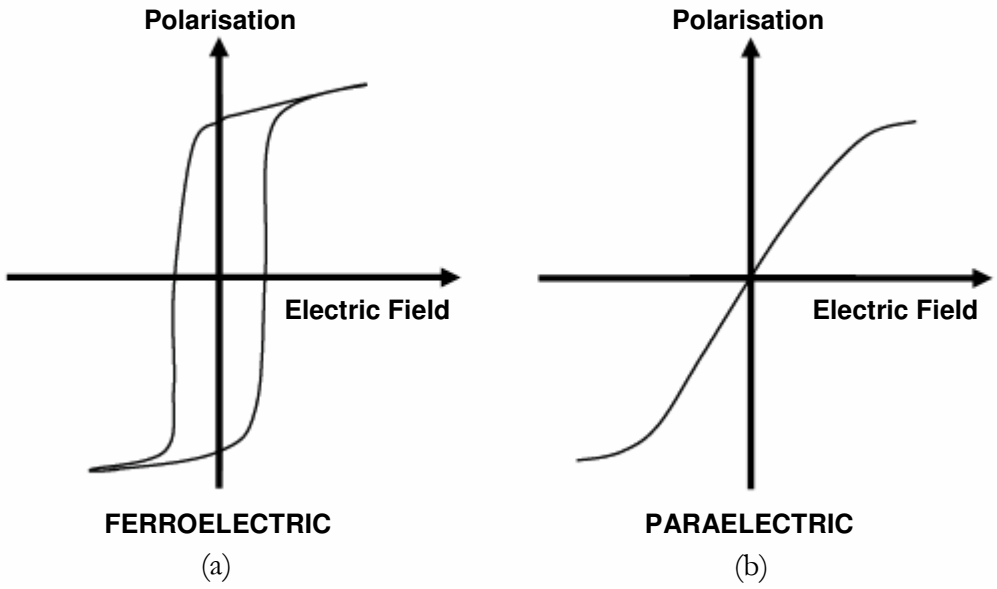

Figure 2.2.1: Polarisation of ferroelectric material in ferroelectric and paraelectric state in response to external applied electric field, showing (a) hysteresis, and (b) no hysteresis.

external electric field. An operating temperature slightly above the Curie temperature in the paraelectric phase is normally preferred for tunable microwave devices as ferroelectrics in this state are free from the hysteretic effect and have moderate loss [15, 34]. Despite this technical distinction, ferroelectrics used in the paraelectric phase for tunable microwave devices are still referred to as ferroelectric materials.

2.2.1 Dielectric Properties

Ferroelectrics are essentially a non-linear dielectric due to their dielectric constant dependency with external applied electric field and temperature.

2.2.1.1 Field Dependent Dielectric Constant

Several ferroelectric materials are suited for integration with monolithic microwave integrated circuits (MMICs) and perhaps the most studied material for microwave application is $Ba_xSr_{1-x}TiO_3$ (BST), where x can vary from 0 to 1. BST is a

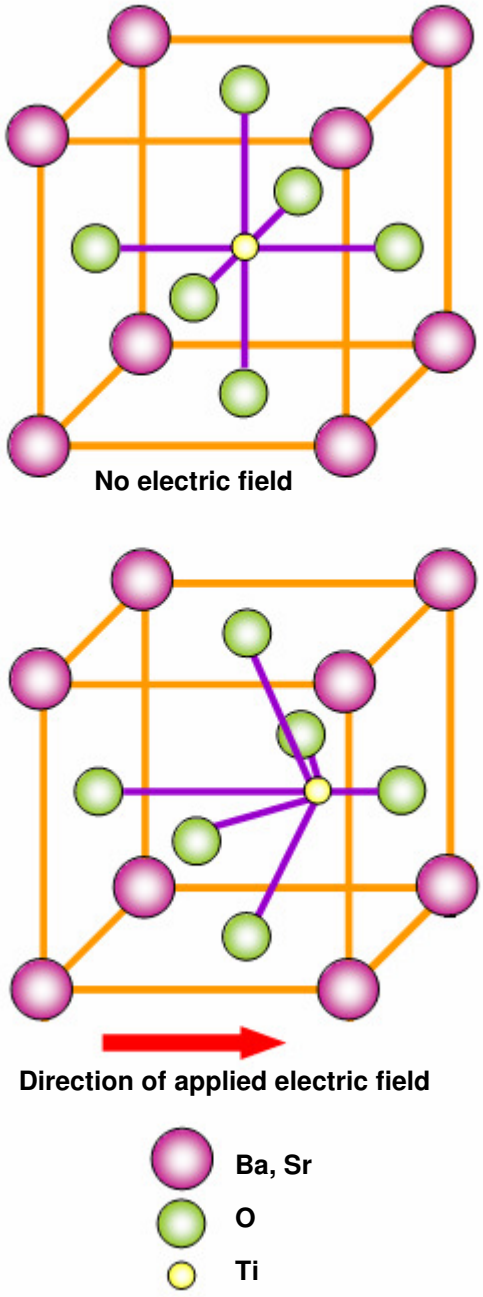

Figure 2.2.2: Perovskite structure and electric polarisation of a unit cell Barium Strontium Titanate (Ba,Sr)TiO_3 in response to external applied electric field [37].

composition where Barium (Ba) ions are introduced into pure Strontium Titanate ($SrTiO_3$ or STO) to attempt to improve the microwave properties. Pure STO is particularly attractive due to its crystalline compatibility with high temperature superconductors (HTSs) and it is in the paraelectric state at all temperature, hence, there is no Curie temperature above 0 K. On the other hand, Barium Titanate (BTO) has a Curie temperature of about 400 K. Different composition ratio allows tailoring of the Curie temperature. Generally, a value of x = 0.4 – 0.6 is used to optimised its properties for room temperature, and a value of around x = 0.1 – 0.2 is used when the material is used in conjunction with HTS films [1, 2, 38-40].

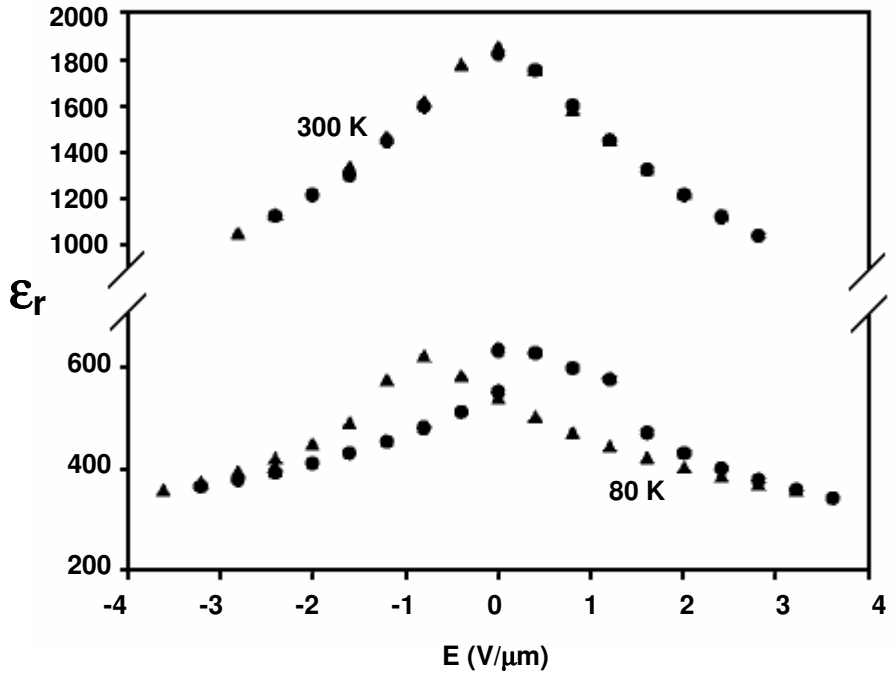

Figure 2.2.3: Dielectric constant curve of a BST thin-film at 80 K and 300 K, adopted from [41]. ⑩ and ③ represent the dielectric constant when voltage was swept up and down, respectively in order to demonstrate any hysteresis behaviour.

Figure 2.2.3 depicts the variation of the relative dielectric constant ε_r of $Ba_{0.5}Sr_{0.5}TiO_3$ (BST) thin-film as a function of electric field and temperature [41]. As shown in the figure, the dielectric constant of BST decreases with increasing electric field and temperate. At 300 K, BST thin-films have a ε_r in the range of 1000-2000

with no hysteresis [41]. This show the thin-films are in the paraelectric state. As temperature cools down to 80 K, ε_r drops to below 700 and hysteresis is observed as the voltage was swept up and down. This is expected as the BST thin-film is in the ferroelectric state.

2.2.1.2 Tunability

As mentioned earlier, one of the most important properties of ferroelectric material is the strong dependence of their dielectric constant on external applied electric field E. This characteristic is commonly described by the tunability n, defined as the ratio of the dielectric constant of the material at zero electric field to its dielectric constant at non-zero electric field, as expressed by equation (2.2.1). The relative tunability n_r in percentage is defined by equation (2.2.2).

$$n = \frac{\varepsilon(0)}{\varepsilon(E)} \tag{2.2.1}$$

$$n_r = \frac{\varepsilon(0) - \varepsilon(E)}{\varepsilon(0)} \cdot 100\% \tag{2.2.2}$$

2.2.1.3 Loss Tangent

Ferroelectric materials, like any other dielectrics, commonly suffer from dielectric losses. To express this mathematically, the dielectric constant of ferroelectrics can be represented in complex form with both real ε' and imaginary parts ε'' as follow.

$$\varepsilon = \varepsilon' + j\varepsilon'' \tag{2.2.3}$$

The imaginary part of the dielectric constant ε'' accounts for the loss factor, governed by the lag in polarisation upon application of the electric field and the

energy dissipation associated with charge polarisation. This loss factor is characterised by the ratio of the imaginary and the real part of the dielectric constant, which commonly known as loss tangent, tan δ.

$$\tan\delta = \frac{\Im(\varepsilon)}{\Re(\varepsilon)} = \frac{\varepsilon''}{\varepsilon'} = \frac{1}{\mathrm{Q}} \tag{2.2.4}$$

where Q is the quality factor of the material. Ideally, materials with high tunability and low loss tangent at microwave frequencies are greatly desired in the field of microwave engineering application. However, in conjunction with high tunability, most ferroelectrics possess high loss and temperature dependency as well [42, 43]. The correlation between the tunability and the loss tangent often forces designers to choose the material with the optimal trade-off between these two parameters for best device performance.

2.2.2 Bulk, Thick-Film and Thin-Film

Ferroelectrics come in several forms, namely bulk, thick-film and thin-film. Each of these forms has its pros and cons. Bulk ferroelectrics are usually in the 500-2000 μm range thickness. Due to their very high dielectric constant, typically in the order of few to tens of thousands, bulk ferroelectrics are useful in substantial size reduction of microwave devices. Bulk ferroelectrics have been used in many applications such as tunable dielectric resonators [44, 45], tunable filters [46, 47], varactors [48] and a lens antenna [49]. The major drawback of bulk ferroelectrics, however, is that very high tuning voltages, in the order of hundreds of volts to tens of kilovolts [4, 34], is required to achieve a usable tuning range. This greatly limits their use in tunable microwave devices. Nonetheless, as will be pointed out later, bulk ferroelectrics generally exhibits lower loss tangent values than other form of ferroelectrics.

Thick-films relate to thickness of greater than about 1 μm. In addition to this

thickness stipulation, they are usually of a polycrystalline form. Ferroelectric thick-films are considered a more practical form than bulk as substantially lower tuning voltage is required (few hundreds of volts). Furthermore, with the development of tape casting [11] or screen-printing technology [50], the production cost of thick-film has significantly decreased, hence, making thick-film a good candidate for cost-effective tunable device. Many tunable devices, such as phase shifters [50, 51], varactors [15, 52] and tunable filters [53] have demonstrated the use of thick-film. These results, though promising, are not as good as that obtained with thin-film in terms of tunability.

A thickness of less than 1 μm is often referred to as thin-film and they are usually more crystalline in nature being made from sputtering, laser ablation or other thin-film processing technique. Ferroelectric thin-films are very attractive for microwave tunable application due to their relatively low production cost and most importantly, low tuning voltage requirement, typically between 2 and 200 volts, depending on the thin-film composition and film thickness. The dielectric response of ferroelectric thin-films is usually different from that of bulk ferroelectric materials in terms of dielectric constant and tunability. According to the literatures [4, 34], the dielectric constant of the thin-films is usually lower and the loss tangent, tan δ is always higher than in their bulk or thick-film counterparts. Nonetheless, the much lower tuning voltage and other integration benefits still make ferroelectric thin-film a very feasible candidate in tunable microwave devices. The quality of the ferroelectric thin-films is also strongly depends on the substrates used for film deposition. Substrates such as Magnesium Oxide (MgO), Alumina or Sapphire (Al_2O_3), and Lanthanum Aluminate ($LaAlO_3$) are often used as substrate in ferroelectric film-based components due to their low loss tangent and their good lattice matching with the film.

2.2.3 Thin-Film Growth Techniques

Ferroelectric thin-films can be grown by various deposition techniques, each of

which has its merits and disadvantages. Generally, these techniques can be classified into three groups:

- Physical vapour deposition (PVD) – this includes RF and magnetron sputtering, molecular beam epitaxy and pulsed laser deposition (PLD)
- Chemical vapour deposition (CVD) – this includes metal-organic chemical vapour deposition (MOCVD) and atomic layer deposition (ALD)
- Chemical solution deposition (CSD) – this includes sol-gel and metal-organic decomposition

Pulse laser deposition (PLD) has several characteristics that made it remarkably competitive in the complex thin-film arena as compared to other film growth techniques. The distinct attractive feature that makes PLD technique so favourable is its ability to preserve the stoichiometry of compound materials (i.e. the deposited film has the same chemical structure as the target material) [35, 54]. Furthermore, PLD technique offers simplicity of use, relatively high deposition rate and it is more economical than other deposition techniques. It is not the intention of this thesis to elaborate PLD technique in detail but rather to have a brief overview of the methodology.

2.2.3.1 Pulsed Laser Deposition

The Pulsed Laser Deposition (PLD) technique has been widely used to grow various thin-films and multi-layers of complex materials for many years. Although the PLD technique is unable to make uniform film coating on large scale wafers and for mass production, it still has appeal for many researchers for the fabrication of high-quality films of ferroelectric materials [35, 54].

As shown in Figure 2.2.4, PLD consists of a target holder and a substrate heater housed in a vacuum chamber. A high power pulsed-laser beam, used as an external energy source, is focused inside the vacuum chamber to strike a target of the desired composition. Material is then vaporised in the form of an ionised plume from

the target, resulting in thin-film growth on the substrate. This process can occur in ultra high vacuum or in the presence of a background gas, such as oxygen which is commonly used when depositing oxides to oxygenate deposited films.

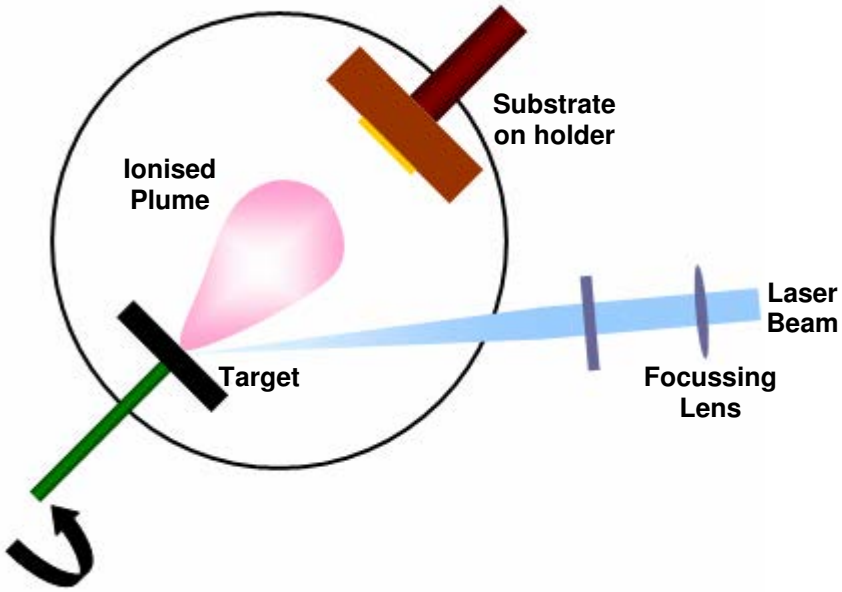

Figure 2.2.4: Schematic of PLD system for deposition of thin-films [54].

2.2.3.2 BST Thin-Film

A great deal of works on ferroelectric $Ba_xSr_{1-x}TiO_3$ (BST) thin-films growth using the PLD technique has been reported over the years [38, 40, 55-58]. BST thin-films are considered to be one of the most promising candidates for tunable microwave devices because of their large nonlinearity of dielectric constants with the applied electrical field and the adjustable dielectric properties from different doping ratio of Strontium (Sr) and Barium (Ba). BST thin-films with x = 0.4 – 0.6 are typically used as they demonstrates a large electric field effect at room temperature.

The dielectric constant and the loss tangent are the two most important parameters affecting the practical applications of BST thin-films in tunable

microwave devices. These parameters strongly depend on the quality of the film as well as the substrate used for film deposition [56, 58]. Single crystal (001) MgO substrate is often selected for the growth of BST thin-films due to its excellent dielectric properties in terms of low loss tangent, and also, its good durability and low-cost compared to other substrates.

2.3 Applications of Ferroelectric Materials

Ferroelectric materials have been receiving tremendous attention over the past decade due to the increasing demand for smaller size, lighter weight, higher speed, lower cost and higher power capability frequency-agile components. The change of dielectric constant of ferroelectric materials with the applied electrical field holds the key to a wide range of application such as varactor, phase shifter and tunable filter. This section aims to give a brief overview of the application of ferroelectric, BST thin-film in particular.

2.3.1 Varactor

A varactor, also known as variable or tunable capacitors, is by far the simplest component that can be produced by ferroelectric materials. There are essentially two categories of thin-film varactors, namely, planar varactors and parallel-plate varactors, as shown in Figure 2.3.1, although they are some variations in the exact configurations in the literatures [4, 44, 59-62].

The parallel-plate varactors have the advantage of using the tunability of the film more efficiently and require a relatively small voltage for effective tuning (1-20 *V*) since the electric fields are better confined in the film as the bias voltage is applied across the film thickness. However, parallel-plate varactors involved a more elaborate process and require bottom electrode patterning. In addition, the electrodes in parallel-plate structure contribute to a higher loss than in the case of planar structure.

For planar varactors, the electric field is applied along the ferroelectric film across the gap. The electrodes need to be close together in order to maximise the field within the ferroelectric film. The capacitance value can be completely controlled by the metallisation patterns and geometrical parameters on one metal layer. An interdigital finger structure has been used to increase the tunability of the varactor [63-65]. Figure 2.3.2 shows an example of the layout of an interdigital varactor.

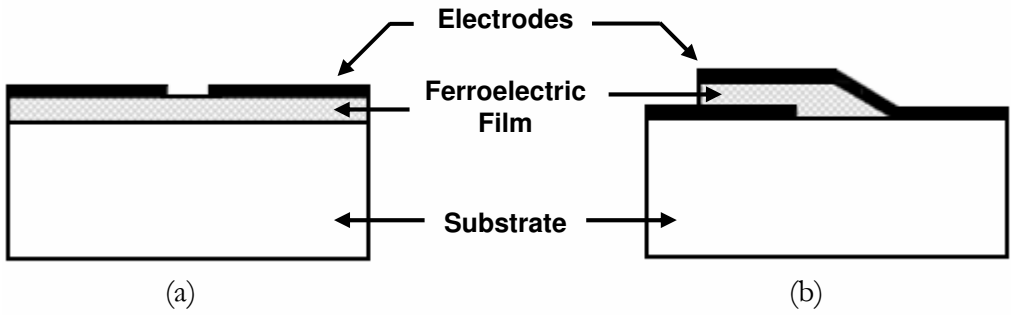

Figure 2.3.1: (a) Planar, and (b) parallel-plate varactor based on ferroelectric film [34].

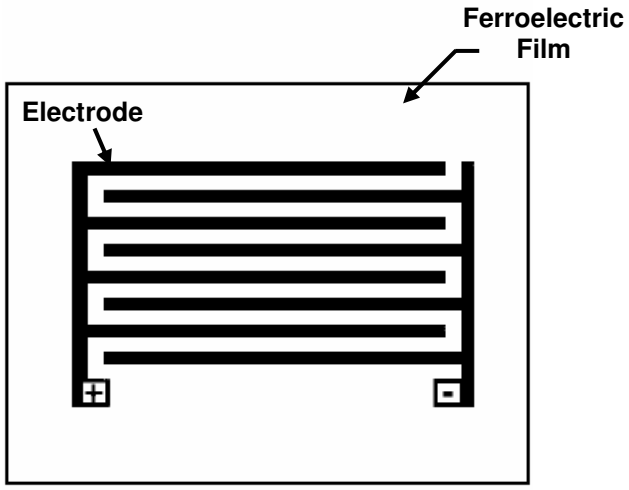

Figure 2.3.2: Layout of the interdigital varactor on ferroelectric film [65].

The characteristic of a varactor is based on two main parameters: tunability of the varactor and the loss factor, tan δ of the ferroelectric materials. This is described as Commutation Quality Factor *K* [66], defined as

$$K = \frac{(n-1)^2}{n \cdot \tan \delta_1 \cdot \tan \delta_2} \tag{2.3.1}$$

where *n* is the tunability of the varactor as defined in equation (2.2.1), and $\tan \delta_{1,2} = \omega C_{1,2} R_{1,2}$ is the loss tangent of the varactor, determined by the value of the capacitance *C* and the series resistance *R* at zero and non-zero electric field, (denoted by subscript 1 and 2), respectively.

2.3.2 Phase Shifter

The ferroelectric phase shifter is by far the most widely studied tunable ferroelectric component and hence, has been reported in many papers [1, 8-10, 38-40, 67, 68]. A phase shifter is simply a device that provides a shift in phase angle of a microwave signal without depreciating the magnitude. They play a crucial role in phased array antennas for wireless and satellite communications system.

A phased array refers to an antenna configuration, composed of a large number of elements that emit phased signals, which can be served by thousands of phase shifters, to form the beam. The phase shifters are used to electronically steer and control the position of the beam. Traditionally, phase shifters in phased array antenna system are constructed using ferrites which strong magnetic fields are required for tuning. Implementing ferrite phase shifters in phase arrays are extremely costly, bulky and heavy for commercial applications. In addition, ferrite phase shifters are slow to respond to control signals hence, cannot be used in applications where rapid beam scanning is required. For these reasons, the application of ferroelectric phase shifters in phased array antenna is greatly favoured due to their potential for better performance in terms of tuning speed and power handling

capability, as well as smaller size and lower cost.

Ferroelectric phase shifters can be classified into two categories, analogue and digital. Analogue ferroelectric phase shifters have a single analogue input control voltage, giving a theoretical infinite resolution. The simplest form of analogue ferroelectric phase shifter is the use of a simple coplanar line structure patterned on a ferroelectric thin-film coated substrate, as shown in Figure 2.3.3. This type of phase shifter can also be called a delay-line. The phase velocity of the electromagnetic wave travelling through the line is varied by controlling the external applied electric field as the dielectric constant of the ferroelectric thin-film changes depending on the magnitude of the electric field strength, thus producing the phase shift.

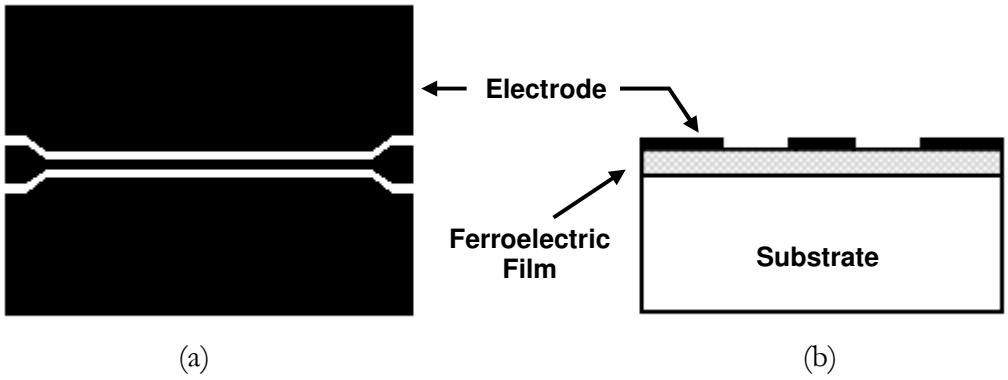

Figure 2.3.3: Layout and cross section of a ferroelectric delay-line type analogue phase shifter in double layer substrate coplanar waveguide structure [68].

Another method is by loading the transmission line with a ferroelectric varactor where the phase velocity of the electromagnetic wave can be continuously tuned by biasing the varactor, providing necessary phase shift (Figure 2.3.4) [59]. This is contrast to the previous case where the coplanar line is homogeneously loaded with ferroelectric film. Analogue ferroelectric phase shifters are low cost and a precise phase shift can be obtained with single analogue control voltage.

Digital ferroelectric phase shifters have digital input signals, offering a limited resolution or a fixed phase shift (e.g. 45°, 90° or 180°) [69]. Figure 2.3.5 shows the layout of a digital reflection type phase shifter, which consist of a transforming circuit that is terminated by a coplanar 3-electrode capacitor. The advantage of the digital phase shifters is a better impedance matching with the 50 Ω external impedance and also lower amplitude modulation distortions [69].

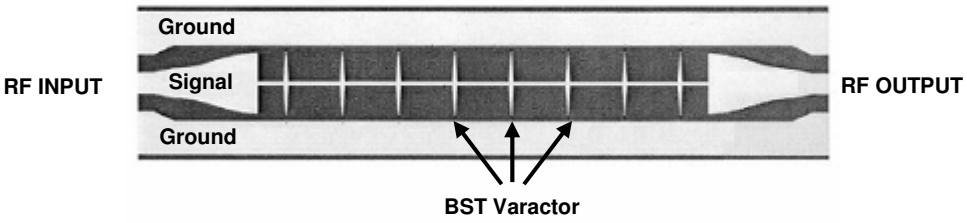

Figure 2.3.4: Layout of a loaded-line phase shifter with BST varactor [59].

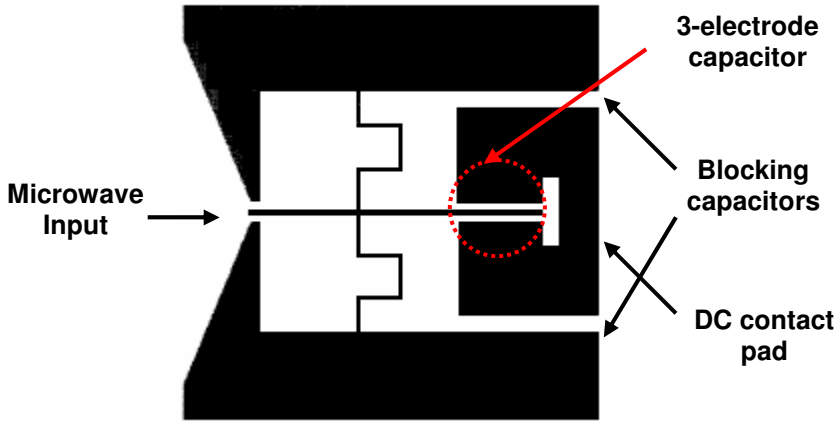

Figure 2.3.5: Layout of the 180° ferroelectric reflection type digital phase shifter [69].

The performance of the phase shifter is determined by the amount of phase shift $\Delta\Phi$ and the insertion loss of the phase shifter in both states $IL_{1,2}$ (i.e. zero and non-zero electric field). This is commonly described as figure-of-merit *FoM*, expressed by the following equation [16].

$$FoM = \frac{\Delta\Phi}{\sqrt{IL_1 \cdot IL_2}} \left(^\circ/\mathrm{dB}\right) \tag{2.3.2}$$

For a phase shifter based on ferroelectric varactor and lossless non-tunable components, the *FoM* of the phase shifter then depends on the Commutation Quality Factor (*K*) of the ferroelectric varactor only, as defined in equation (2.3.1), and turns into [16]:

$$FoM = B(m) \cdot \sqrt{K} \left(^\circ/\mathrm{dB}\right) \tag{2.3.3}$$

where *B(m)* is the coefficient depending on the types of phase shifter. This is shown in Table 2.3.1.

Number of bits, m	**1**	**2**	**3**	**4**	**>>1**
$B(m)$ for a digital phase shifter	10.36	9.11	8.68	8.50	8.36
B for a analogue phase shifter	6.6				

Table 2.3.1: Coefficient *B(m)* for the figure-of-merit of a digital or analogue phase shifter [16].

2.3.3 Tunable Filter

Tunable filters are a more recent frequency-agile component implemented using ferroelectric materials. They have been reported in [3, 70-73]. These filters have been demonstrated in microstrip, coplanar waveguide (CPW) or conductor-backed coplanar waveguide (CBCPW) structure. The characteristic of the tunable band pass filter is determined by two most important parameters: in-band insertion loss of the

filter in both states and the shift of the central frequency due to the tuning. The figure-of-merit of the tunable band pass filter FoM_{BPF} can be expressed in the following form [66]:

$$FoM_{BPF} = \frac{\omega_{02} - \omega_{01}}{\sqrt{\Delta\omega_1 \cdot \Delta\omega_2}} \cdot \frac{1}{\sqrt{IL_1 \cdot IL_2}} \left(\mathrm{dB}^{-1}\right) \tag{2.3.4}$$

where $\omega_{01,02}$ are the central frequencies of the filter, $\Delta\omega_{1,2}$ are the band widths of the filter and $IL_{1,2}$ are the insertion loss of the filter at both states (i.e. zero and non-zero electric field). An example of a tunable band-pass filter based on ferroelectric materials [73] is presented in Figure 2.3.6. The dielectric substrate of the filter consists of two layers: a 1 μm thick of BST film and a 0.5 mm thick of alumina/sapphire (Al_2O_3) substrate. The thickness of the copper microstrip is 4 μm. The ferroelectric capacitors are formed by gaps in the microstrip lines. A figure-of-merit of 0.34 dB^{-1} is obtained with a 150 V biasing voltage at room temperature.

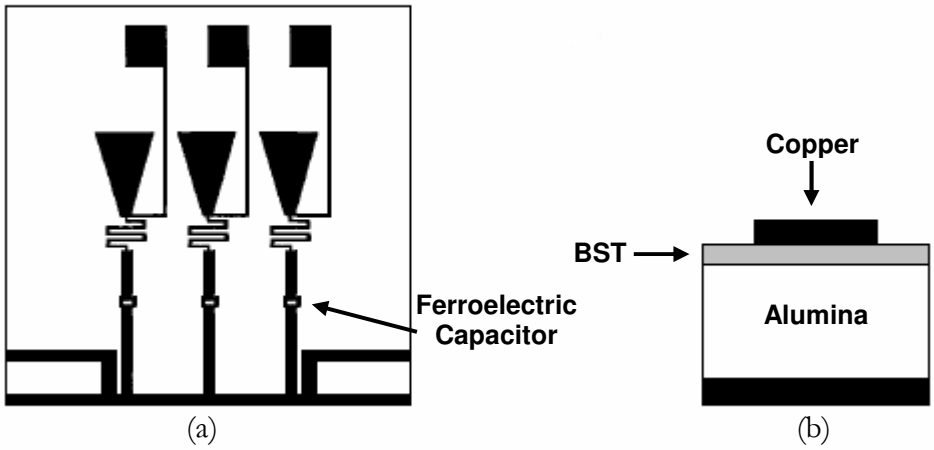

Figure 2.3.6: (a) Layout and (b) cross section of a tunable filters on BST film [73].

2.4 Conclusions

The fundamentals of ferroelectric materials in terms of dielectric properties, various forms of ferroelectric material and thin-film growing techniques have been presented. A brief survey of ferroelectric-based frequency-agile devices reported in the literatures has been reviewed. Many works on BST tunable microwave devices has been reported over the years. BST thin-films are particularly attractive due to their large nonlinearity of dielectric constant with the applied electrical field and their adjustable dielectric properties from different doping ratio of Strontium (Sr) and Barium (Ba). This allows tailoring of device operation at various temperatures. Pulsed laser deposition (PLD) technique is often used to grow BST thin-film. Such a growth method has been widely used in many research laboratories.

In the next chapter, a review of microstrip and coplanar waveguide will be presented. As crucial to circuit design, analytical expression for each geometry relevant to the inclusion of thin ferroelectric layers will be shown.

Chapter 3

Planar Transmission Lines

3.1 Introduction

A number of planar transmission lines will be briefly reviewed in this chapter and in particular, models of single and multilayer configuration will be presented. These models will be employed in Chapter 5 and 6 to predict the properties of the ferroelectric thin-film, as well as the performance of the ferroelectric phase shifter and tunable attenuator.

3.2 Planar Transmission Line Overview

A planar transmission line has conducting metal strips that lie entirely in parallel planes. This implies that the characteristics of the planar transmission lines can be determined by considering the dimensions in single or multiple planes. Ease of fabrication by photolithographic and printed circuit technique allows it to be used for a wide variety of circuit components. Planar transmission lines have played a

leading role in the development of both microwave integrated circuits (MICs) and monolithic microwave integrated circuits (MMICs). Examples of the most commonly used planar transmission lines are shown in Figure 3.2.1.

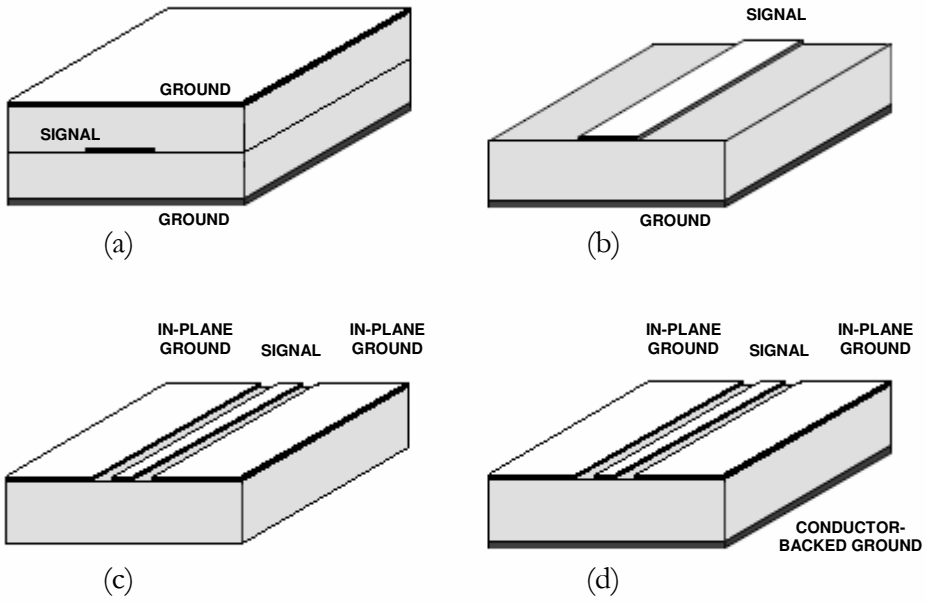

Figure 3.2.1: Main types of planar transmission line (a) stripline, (b) microstrip, (c) coplanar waveguide (CPW), and (d) conductor-backed CPW (CBCPW).

A stripline consists of a conducting strip embedded in a dielectric medium between two ground planes (Figure 3.2.1(a)). This construction supports a pure transverse electromagnetic (TEM) propagation mode as the conductor strip is completely surrounded by the dielectric medium (i.e. homogenous dielectric). The presence of both top and bottom ground planes provides good isolation from other signals. From a fabrication standpoint, a stripline is not as easily fabricated compared to a microstrip and coplanar waveguide. In practice, a small air gap can occur between the substrates during the fabrication process which would introduce an inhomogeniety in the stripline dielectric, and is often the reason for unexpected spurious transmission line performance.

Apart from benefits on the fabrication front, microstrip is one of the most popular planar transmission lines, primarily due to its integration compatibility with other microwave devices. A microstrip consists of a thin layer of conducting strip constructed on a dielectric substrate with a ground plane at the bottom (Figure 3.2.1(b)). Unlike the stripline however, this geometry does not support a pure TEM wave as the dielectric substrate does not fill the air region above the strip. As a result of the open structure of the microstrip, the electromagnetic field or energy transmitted in the microstrip may be radiated into space or adjacent lines.

A mutual drawback for both the stripline and microstrip is that for a given substrate thickness, the line widths cannot be arbitrarily chosen for a certain characteristic impedance. Coplanar waveguide (CPW) of the type shown in Figure 3.2.1(c), on the other hand, offers some degree of freedom as the characteristic impedance is determined by the ratio of strip and gap width and is less dependent on substrate thickness. Therefore, by keeping an appropriate strip-to-gap ratio, different line widths can be chosen for a specific characteristic impedance [74]. As the ground of the CPW structure is in the same plane as the conducting strip, it eliminates the need for via holes during surface mounting of the microwave device. In addition, CPW features the lowest cross talk or interference levels from other signals among these three planar transmission lines due to the presence of the ground plane between any two adjacent lines. As a result, CPW circuits can be fabricated more compact than microstrip and stripline circuits, making it an ideal circuit structure for MIC, as well as MMIC applications.

Figure 3.2.1(d) depicts the conductor-backed coplanar waveguide (CBCPW), a modification of CPW. The additional lower ground plane of CBCPW provides several advantages in the construction of MMIC such as improved mechanical support to the substrate and to act as a heat sink for circuits with active devices. However, the introduction of the conductor backing could potentially establish an unwanted parasitic parallel-plate mode leakage between the upper in-plane and lower ground plane, depending on frequency, substrate thickness and dielectric constant [75].

Two substrate configurations will be implemented in the ferroelectric phase shifter and tunable attenuator in this work. The first is a multilayer substrate configuration, which consists of a layer of ~0.35 μm thick ferroelectric BST thin-film with dielectric constant, ε_r of 1800 at zero bias voltage on top of a 500 μm thick MgO substrate (ε_r = 9.8). The second configuration is a single layer Duroid substrate of thickness 254 μm with ε_r of 10.2. In the following sections, models of both the single and multilayer configurations will be presented and subsequently be used for circuit design described in later chapters.

3.3 Microstrip

The general structure of a microstrip is illustrated in Figure 3.3.1. A conducting strip with a width *w* and a thickness *t* is constructed on a dielectric substrate that has a relative dielectric constant ε_r and a thickness *h*, and the bottom of the substrate is a ground (conducting) plane.

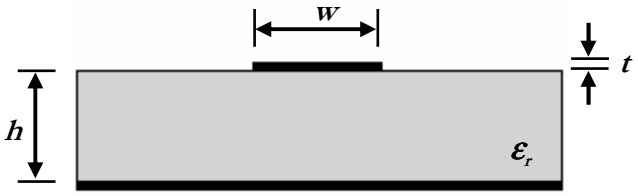

Figure 3.3.1: Microstrip configuration.

Microstrip has its field lines distributed within two media – air above and dielectric below. For this reason, the microstrip structure is inhomogeneous and does not support a pure TEM wave. With the presence of the dielectric-air interface, the wave propagation velocity in a microstrip will not only depend on its material properties, i.e. the dielectric constant ε and the permeability μ, but also on the

physical dimensions of the microstrip [76]. In microstrip, most of the electromagnetic (EM) field is concentrated between the strip conductor and the ground plane in the substrate. The field in the air region or fringing field components are usually much smaller compared to the main field (within the substrate below the strip). In this situation, the dominant mode in a microstrip behaves like a TEM mode, and thus, TEM transmission line theory is applicable. This is usually referred to as quasi-TEM approximation and is valid over most of the operating frequency ranges of a microstrip.

In the quasi-TEM approximation, the inhomogeneous dielectric-air media of microstrip is replaced by a homogenous dielectric material with an effective dielectric constant. Transmission characteristics of the microstrip, namely, the effective dielectric constant ε_{eff} and characteristic impedance Z_c can then be obtained by using quasi-static analysis [77]. With this technique, the fundamental mode of wave propagation in a microstrip is assumed to be pure TEM. This analysis was found to be adequate for designing circuits at frequencies below the X-band where the strip width and the substrate thickness are many orders of magnitude smaller than the wavelength in the dielectric materials [77].

For a single layer microstrip structure, as depicted in Figure 3.3.1, the closed-form expressions for ε_{eff} and Z_c reported by [78] are given as follows.

$$\varepsilon_{eff} = \frac{\varepsilon_r + 1}{2} + \frac{\varepsilon_r - 1}{2}\left(1 + \frac{10}{u}\right)^{-ab} \tag{3.3.1}$$

$$Z_c = \frac{\eta_0}{2\pi\sqrt{\varepsilon_{eff}}} \ln\left[\frac{F}{u} + \sqrt{1 + \left(\frac{2}{u}\right)^2}\right] \tag{3.3.2}$$

where $u = w/h$, $\eta_0 = \sqrt{\mu_0 / \varepsilon_0} \approx 120\pi$, and

$$a = 1 + \frac{1}{49}\ln\left(\frac{u^4 + \left(\frac{u}{52}\right)^2}{u^4 + 0.432}\right) + \frac{1}{18.7}\ln\left[1 + \left(\frac{u}{18.1}\right)^3\right]$$

$$b = 0.564\left(\frac{\varepsilon_r - 0.9}{\varepsilon_r + 3}\right)^{0.053}$$

$$F = 6 + (2\pi - 6)\exp\left[-\left(\frac{30.666}{u}\right)^{0.7528}\right]$$

In this single layer microstrip model, the thickness of the conductor is assumed to be very thin (i.e. $t \to 0$). The accuracy of ε_{eff} is better than 0.2% for $\varepsilon_r \leq 128$ and $0.01 \leq u \leq 100$, while the accuracy of Z_c is better than 0.01% for $u \leq 1$ and 0.03% for $u \leq 1000$.

3.3.1 Multilayer Microstrip

Figure 3.3.2 illustrates a multilayer microstrip which is composed of two different dielectrics ε_{r1} and ε_{r2} below the conducting strip of width w; they have thickness h_1 and h_2, respectively.

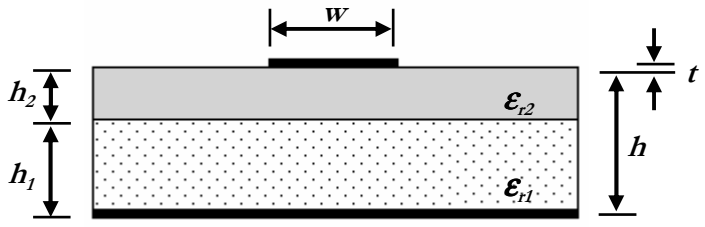

Figure 3.3.2: Multilayer microstrip configuration.

The closed-form expressions for determining the effective dielectric constant ε_{eff} and the characteristic impedance Z_c of a multilayer microstrip are derived using the conformal mapping technique [77]. The principles of this technique assumes quasi-TEM wave propagation in the line, the conductor thickness t is assumed zero with infinite conductivity (i.e. perfect conductors) and that properties of each individual layers are assumed to be linear, homogenous and isotropic. The presence of additional layers of different dielectrics will only alter the effective dielectric constant of the multilayer microstrip.

The closed-form expressions using conformal mapping technique for determining ε_{eff} of a multilayer microstrip reported in [79] are as follows.

$$\varepsilon_{eff} = 1 - q_1 - q_2 + \varepsilon_{r1}\varepsilon_{r2} \cdot \frac{(q_1 + q_2)^2}{\varepsilon_{r1} q_2 + \varepsilon_{r2} q_1} \tag{3.3.3}$$

The filling factor q_1 and q_2 involving the strip width and substrate thickness for a wide microstrip line ($w/h \geq 1$) are

$$q_1 = \frac{1}{2} \cdot \frac{\pi}{4} \left[1 + \frac{\pi}{4} - \frac{h}{w_e} \ln \left(\frac{\pi}{h} \cdot w_e \frac{\sin\left(\pi h_1 / 2h \right)}{\pi h_1 / 2h} + \cos\left(\pi h_1 / 2h \right) \right) \right]$$

$$q_2 = 1 - q_1 - \frac{1}{2} \cdot \frac{\ln\left(\pi w_e / h - 1 \right)}{w_e / h}$$

where $\eta_0 = \sqrt{\mu_0 / \varepsilon_0} \approx 120\pi$ and the effective line width is

$$w_e = w + \frac{2h}{\pi} \ln \left[17.08 \left(\frac{w}{2h} + 0.92 \right) \right]$$

For a narrow microstrip line ($w/h \leq 1$), the filling factors are

$$q_1 = \frac{\ln\left(\dfrac{1+h_e}{1-h_e+w/4h}\right)}{2\cdot\ln\left(\dfrac{8h}{w}\right)}\cdot\left[1+\frac{\pi}{4}-\frac{1}{2}\cos^{-1}\left(\frac{w\cdot h_e}{8h}\sqrt{\frac{1+h_e}{1-h_e+w/4h}}\right)\right]$$

$$q_2 = \frac{1}{2}+\frac{0.9}{\pi\cdot\ln\left(\dfrac{8h}{w}\right)}-q_1$$

where $h_e = h_1/h$. The corresponding characteristic impedance Z_c is given by:

$$\begin{aligned} Z_c &= \frac{\eta_0}{\sqrt{\varepsilon_{eff}}}\cdot\frac{h}{w_e} \qquad \text{for } w/h \geq 1 \\ Z_c &= \frac{60}{\sqrt{\varepsilon_{eff}}}\cdot\ln\left(\frac{8h}{w}\right) \quad \text{for } w/h \leq 1 \end{aligned} \tag{3.3.4}$$

This multilayer microstrip model is accurate to better than 1% for $w/h \geq 1$, and 3.5% for $w/h \leq 1$ [79]. This model will be used in Chapter 6 to predict the performance of the ferroelectric tunable attenuator.

By employing the aforementioned single and multilayer microstrip models, the calculated effective dielectric constant ε_{eff} and the characteristic impedance Z_c as a function of strip width w is detailed in Figure 3.3.3. The red line represents a multilayer microstrip with a 0.35 μm thick BST thin-film (ε_{r2} = 1800) on a 500 μm thick MgO (ε_{r1} = 9.8) substrate, while blue lines denote a microstrip on a single layer of 254 μm or 1 mm thick Duroid (ε_r = 10.2) substrate. It can be observed that as the conducting strip width w increased, ε_{eff} increased with a corresponding decline of Z_c. This result was expected as more fields are confined in the substrate between the strip and ground plane for wider strip width. For a given w dimension, a microstrip with a thicker substrate would be expected to have a smaller ε_{eff} and larger Z_c. This is because the field strength in the substrate will fall as the substrate thickness increases, hence, fewer fields will be concentrated between the strip and ground plane.

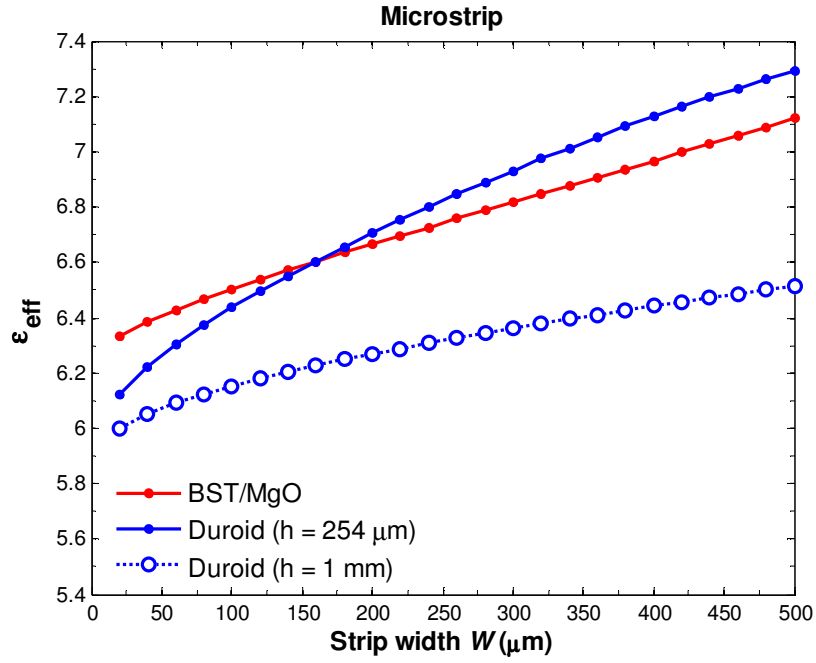

(a)

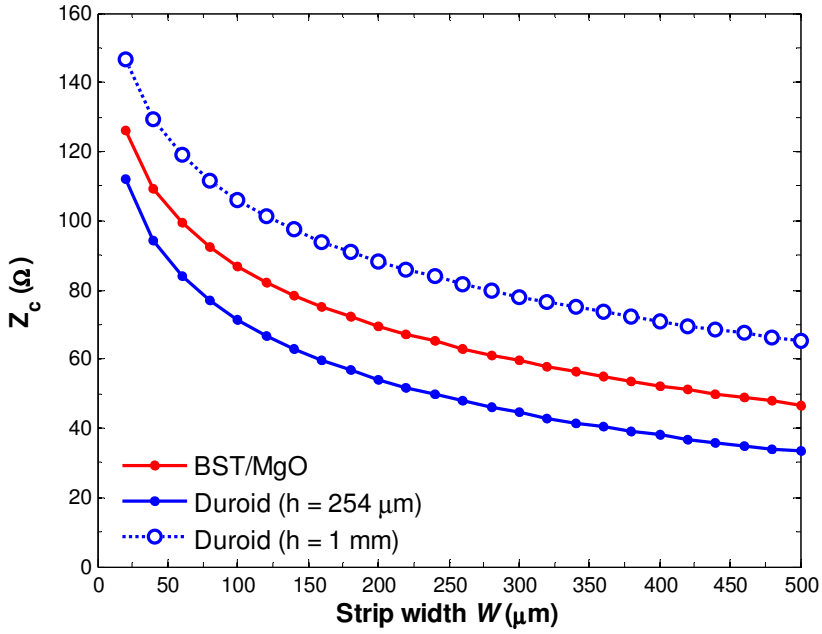

(b)

Figure 3.3.3: Variation of (a) the effective dielectric constant ε_{eff}, and (b) the characteristic impedance Z_c of a microstrip as a function of strip width w.
(BST/MgO: h_1=500μm, h_2=0.35μm, ε_1=9.8, ε_2=1800)
(Duroid: h=254μm or 1mm, ε_r=10.2)

Table 3.3.1 lists a number of calculated parameters for a 50 Ω single and multilayer microstrip line together with corresponding results from Sonnet simulations [80], a planar method-of-moments (MoM) EM simulator, for comparison. In the Sonnet simulations, conductors were assumed to have zero thickness with infinite conductivity, and the simulation cell size was 2 μm, i.e. the line width w was divided into 120 cells for the 240 μm line and 220 cells for the 440 μm line. The simulated values were obtained at 10 GHz. As observed from the table, the calculated values for Duroid-based microstrip showed extremely good agreement with the simulated results. This was expected as the accuracy of the single layer microstrip model, as expressed in equation (3.3.2), is better than 0.01% for $w/h \leq 1$. For the multilayer BST/MgO microstrip, however, the conformal mapping calculation showed a larger deviation when compared to the simulation results. For instance, the analytical solution predicted a width of 440 μm was required to obtain a 50 Ω line, whereas the Sonnet simulation results showed a lower value of 48.5 Ω. This deviation was largely due to the limitation of the multilayer microstrip model employed in equation (3.3.4), which is only accurate to better than 3.5% for $w/h \leq 1$. These parameters will be used in the tunable attenuator in Chapter 6 for single and multilayer configuration, respectively.

Configuration	w (μm)	Calculation method	ε_{eff}	Z_c (Ω)
Microstrip - Duroid (h=254μm, ε_r=10.2)	237	Analytical equation (3.3.2)	6.79	50.0
		Sonnet simulation	6.80	50.0
	240	Analytical equation (3.3.2)	6.80	49.7
		Sonnet simulation	6.81	49.7
Microstrip - BST/MgO (h_1=500μm, ε_1=9.8, h_2=0.35μm, ε_2=1800)	440	Conformal mapping (3.3.4)	7.03	50.0
		Sonnet simulation	7.60	48.5
	400	Conformal mapping (3.3.4)	6.97	52.3
		Sonnet simulation	7.61	50.5

Table 3.3.1: Parameters obtained from calculations based on (3.3.2) or (3.3.4), and simulations.

3.3.2 Microstrip Discontinuities

It is inevitable that discontinuities will have to be used in most microwave circuits. These discontinuities include bends, step changes in widths and tee-junctions, which often cause degradation in circuit performance if improperly treated. In this section, several types of microstrip discontinuities, such as right-angle bend and tee-junction, will be investigated. In order to improve the circuit performance, these discontinuities will be optimised using Sonnet and will be compared with the existing analytical model in the literature. The improved discontinuities will then be used in the ferroelectric tunable attenuator circuit design in Chapter 6, where meandered path and tee-junction is required.

3.3.2.1 Right-angle Bend or Corner

Bends are necessary in many microstrip circuits. The current distribution of a right-angle microstrip bend, together with its equivalent circuit is shown in Figure 3.3.4 [77]. In the plot of the current distribution, the red contour represents a high current density with blue denoting the opposite.

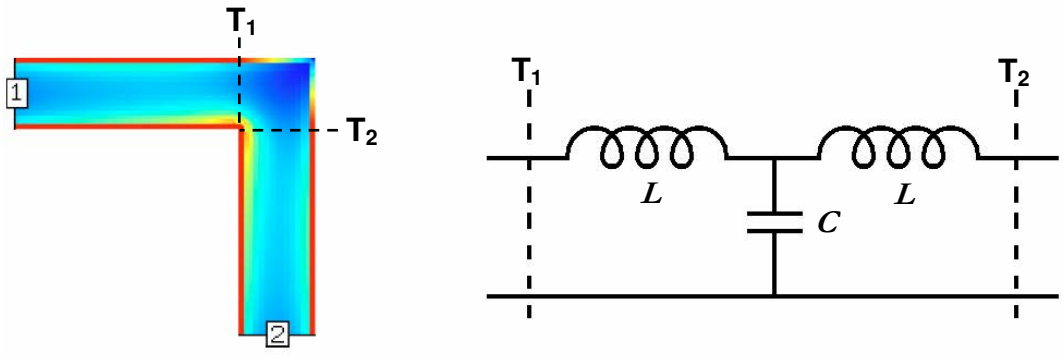

(a) (b)

Figure 3.3.4: Right-angle microstrip bend
(a) current distributions (b) equivalent circuit.

An abrupt right-angle bend in a microstrip causes a significant portion of the signal on the strip to be reflected back towards its source, with only a fraction of the signal being transmitted on around the bend. As shown in Figure 3.3.4(a), the bulk of current flow is concentrated within the vicinity of the inner corner with little or negligible current flowing at the outer corner of the bend. Such a current distribution has contributed to an undesired shunt capacitance that formed between the ground plane and the bend in the microstrip, as depicted in Figure 3.3.4(b).

Several techniques have been investigated in an attempt to eliminate the capacitance effect at the bend. A possible solution would be to specify a smooth swept bend with a radius $r \geq 3w$ [81] without any reduction in conductor area. This arrangement would, however, occupy greater area. A more space-effective compensation method is to chamfer or mitre the bend, which can be of an arbitrary angle [82]. Figure 3.3.5 depicts the current distribution of a 45° mitred right-angle microstrip bend, together with its equivalent circuit. Mitring the bend reduces the area of conductor, and hence removes the excess capacitance at the discontinuity. From Figure 3.3.5(a), it is clear that mitring resulted in a more evenly distributed flow of current around the corner of the bend.

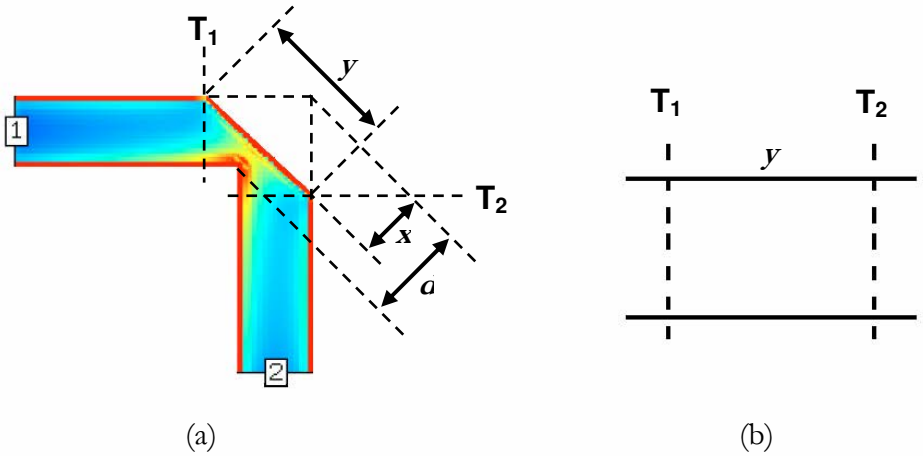

Figure 3.3.5: Mitred right-angle microstrip bend
(a) current distributions (b) equivalent circuit.

The mitre percentage is defined as the cut-away fraction of the diagonal between the inner and outer corners of an equivalent unmitred bend:

$$M = \frac{x}{d} \cdot 100\% \tag{3.3.5}$$

The optimum mitre for a wide range of microstrip geometries has been determined experimentally by Douville and James [82] . They found that a good fit for the optimum mitre percentage *M*, which is illustrated in Figure 3.3.6, is given by,

$$M = \left(52 + 65e^{-1.35\frac{w}{h}} \right)\% \tag{3.3.6}$$

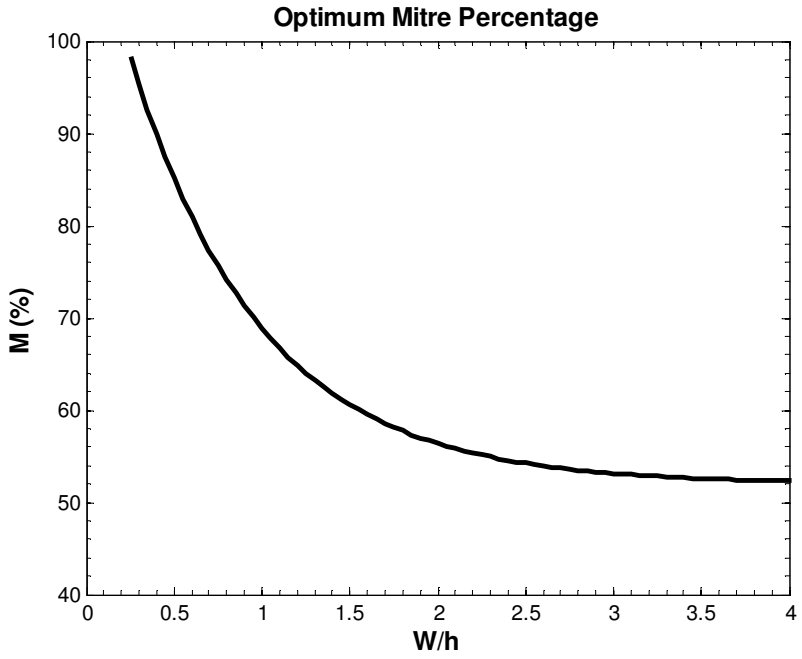

Figure 3.3.6: Optimum mitre percentage as a function of normalised line width [82].

It should be noted that equation (3.3.6) is entirely independent of ε_r and is valid to within 4% for $w/h \geq 0.25$ and $\varepsilon_r \leq 25$. As indicated in Figure 3.3.6, narrower

lines have higher optimum mitre percentage. Thus, extra caution should be taken during the process of fabrication in order to avoid any accidental loss of continuity or over compensation due to poor control of etching.

The plots of results throughout this work will be presented in scattering-parameters unless otherwise stated. The parameters S_{11} and S_{22}, also known as the reflection coefficients, are commonly referred to as the return loss (*RL*); whereas the parameters S_{12} and S_{21}, also called the transmission coefficients, are often referred to as the insertion loss (*IL*). They are with relation to each other as follows [76]:

$$\begin{aligned} RL &= 20\log|S_{nn}|\,\mathrm{dB} \qquad n=1,2 \\ IL &= -20\log|S_{mn}|\,\mathrm{dB} \qquad m,n=1,2(m\neq n) \end{aligned} \tag{3.3.7}$$

Figure 3.3.7 demonstrates the Sonnet simulated return loss ($|S_{11}|$) for a 50 Ω microstrip bend as a function of mitre percentage *M*. The analytical model for optimal mitre percentage given in equation (3.3.6) is included in the figure for comparison. Red and blue line represents a multilayer (BST/MgO) and single layer (Duroid) microstrip, respectively, and Ⓢ denotes the optimal mitre percentage given by the analytical model. Substrates used in multilayer microstrip are a layer of BST ferroelectric thin-film (ε_2 = 1800, tan δ_2 = 0.12, h_2 = 0.35 μm) on top of an MgO substrate (ε_1 = 9.8, tan δ_1 = 1×10^{-4}, h_1 = 500 μm) with 300 nm thick silver metallisation of conductivity 6.17×10^7 S/m, while single layer microstrip consists of a layer of Duroid substrate (ε_r = 10.2, tan δ = 2.8×10^{-3}, h = 254 μm) with 17 μm thick copper conductor of conductivity 5.8×10^7 S/m. The simulated values were obtained at 10 GHz with simulation cell size of 10 μm and 5 μm for multilayer (BST/MgO) and single layer (Duroid) microstrip, respectively.

It was found that when M = 0, i.e. the bend is unmitred, a peak return loss $|S_{11}|$ was obtained, which gradually reduced to a minimum value as *M* increased and approached its optimal level. This was predicted to be 77% and 74% for the BST/MgO and Duroid substrate respectively and compared favourably with calculated values of 74% (BST/MgO with w/h = 0.8) and 70% (Duroid with

w/h = 0.94). As detailed previously, the reduction of conductor area as a consequence of mitring the bend minimised the capacitance between the ground plane and bend. Further increase in M beyond its optimal point however, resulted in diminished performance as the line was over-compensated.

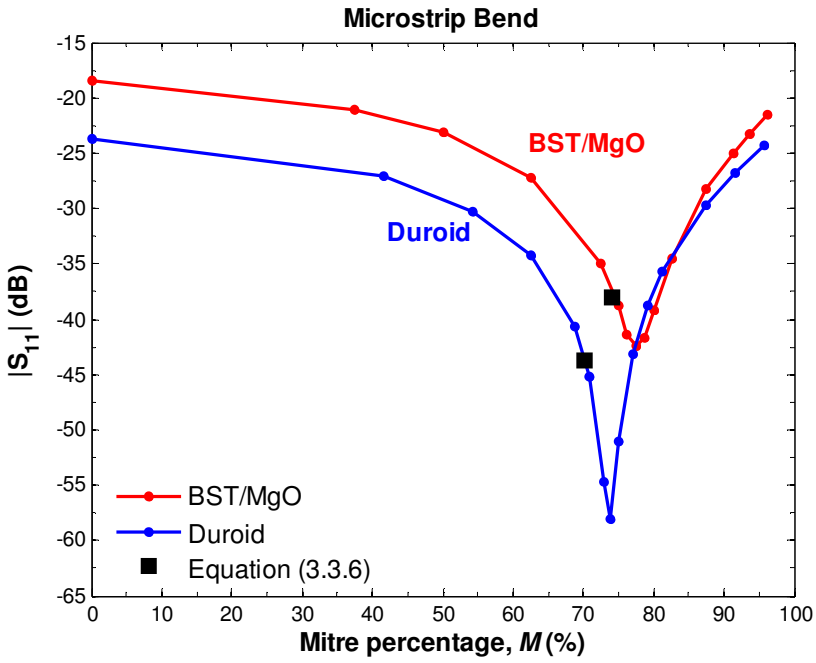

Figure 3.3.7: Simulated S_{11} of a 50 Ω microstrip bend as a function of mitre percentage M. (BST/MgO: w=400μm, h=500.35μm); (Duroid: w=240μm, h=254μm)

3.3.2.2 Tee-junction

A tee-junction is another important microstrip discontinuity and is used to split a signal into two paths. The current distribution of an unequal-impedance microstrip tee-junction, together with its equivalent circuit is presented in Figure 3.3.8. The impedance of the branch line Z_{c2} of width w_2 in the junction is a factor of $\sqrt{2}$ to the main line impedance Z_{c1} of width w_1. With the red and blue contours representing high and low current density respectively, it can be seen that current flow tended to concentrate around the corners with very little at the centre of the junction across

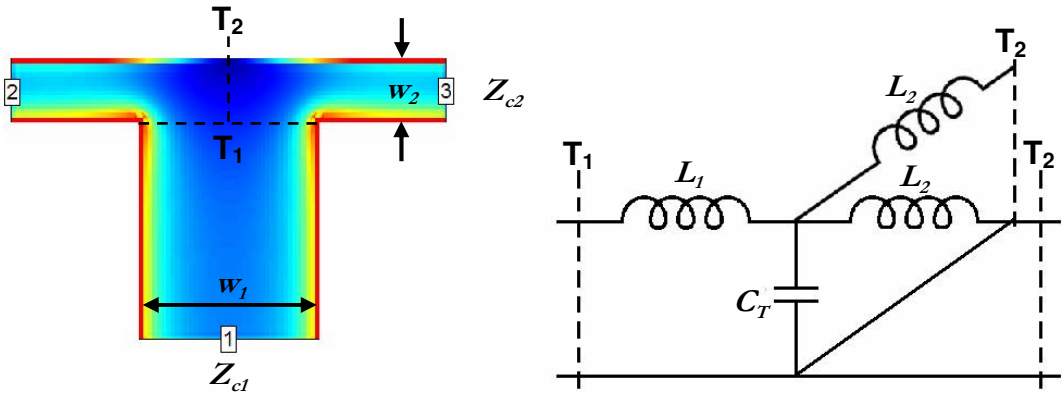

(a) (b)

Figure 3.3.8: Unequal-impedance microstrip tee-junction
(a) current distributions (b) equivalent circuit (impedance ratio $1:\sqrt{2}:\sqrt{2}$).

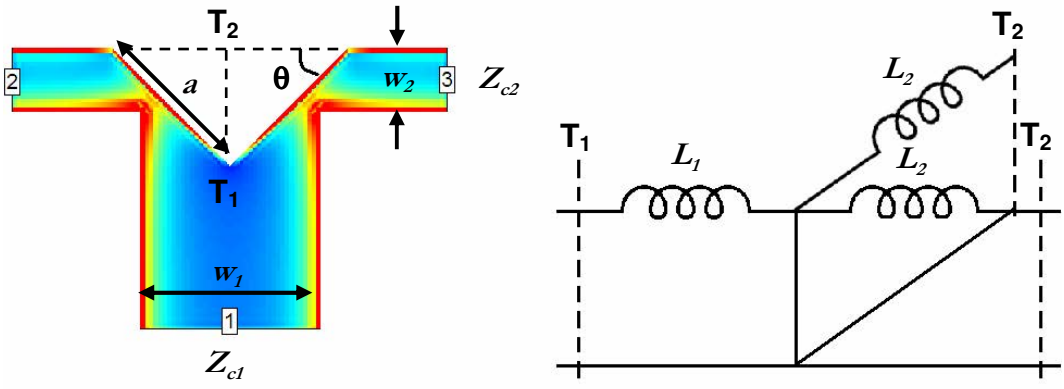

(a) (b)

Figure 3.3.9: Mitred unequal-impedance microstrip tee-junction
(a) current distributions (b) equivalent circuit (impedance ratio $1:\sqrt{2}:\sqrt{2}$).

from the main line. Such an uneven current distribution has created the unwanted discontinuity reactance C_T in the tee-junction.

To compensate for the discontinuity reactance in the tee-junction, Chadha and Gupta [83] proposed the removal of a triangular portion from the junction in the shape of an isosceles triangle. The current distribution for the suggested mitred unequal-impedance microstrip tee-junction together with its equivalent circuit is shown in Figure 3.3.9. The mitred configuration resulted in a more evenly distributed flow of current as the previous 'dead' area was removed.

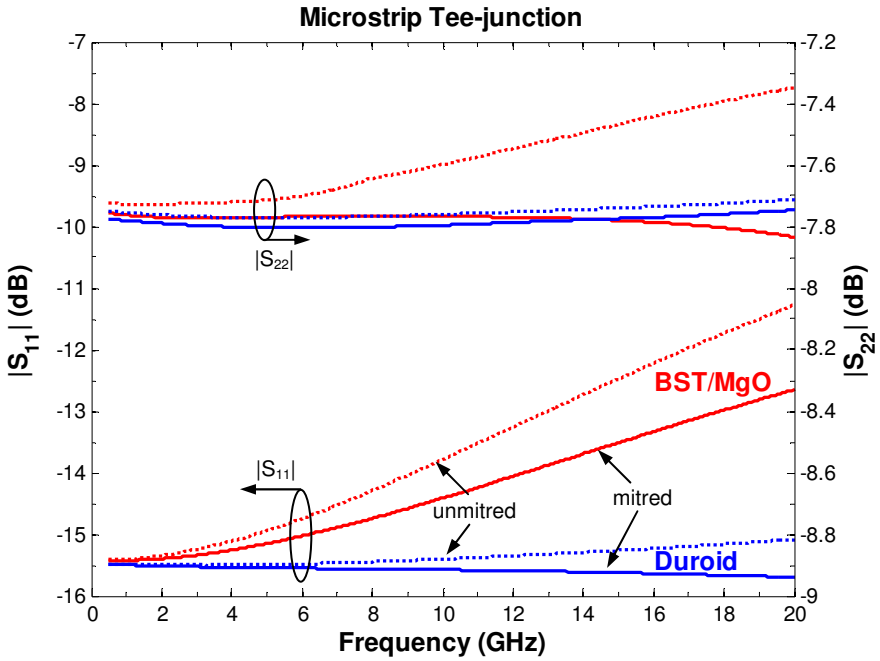

Figure 3.3.10: Simulated S_{11} and S_{22} of unmitred (dotted line) and mitred (solid line) microstrip tee-junction on BST/MgO (w_1=400μm, w_2=140μm, a=368μm), and Duroid substrate (w_1=240μm, w_2=90μm, a=212μm).

Figure 3.3.10 shows the simulated return losses (S_{11} and S_{22}) of unmitred and mitred microstrip tee-junction on multilayer (BST/MgO) and single layer (Duroid) substrates, respectively. The branch line impedances are a factor of $\sqrt{2}$ to the main line impedance (50 Ω : 70.7 Ω : 70.7 Ω), where θ = 45°. The simulation cell size,

substrate and conductor parameters used were the same to the parameters in the simulation of microstrip bend previously used in plotting Figure 3.3.7.

The amount of compensation chosen in the simulation were greater than that recommended in [83], with the tee-junctions optimised by making several runs at 10 GHz using various *a* values. It was found that in order to achieve sufficient improvement in performance without triggering over compensation, the optimum value of *a* for BST/MgO- and Duroid-based tee-junctions were 368 μm and 212 μm, respectively. As observed from the figure, the improvements of the mitred microstrip tee-junction were more pronounced at higher frequencies, particularly for tee-junction on BST/MgO substrate. These optimised tee-junctions will be used in the tunable attenuator in Chapter 6 for power splitting and power combining.

3.4 Coplanar Waveguide

The basic structure of a coplanar waveguide (CPW), as illustrated in Figure 3.4.1, consists of a dielectric substrate with all conductors on the top surface. The centre strip of width 2*s* is separated by a narrow gap *g* from two ground planes on either side, and constructed on a dielectric substrate that has a relative dielectric constant ε_r. This basic structure has become known as the coplanar waveguide (CPW). There are several other variants of this basic structure and will be presented in the following sections.

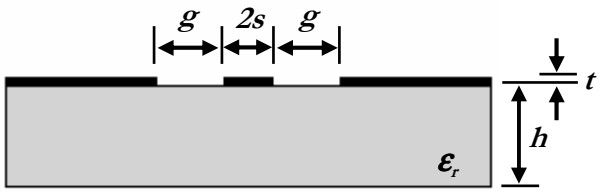

Figure 3.4.1: CPW configuration.

3.4.1 Multilayer CPW

Figure 3.4.2 depicts a multilayer CPW structure, which is composed of a layer of ferroelectric thin-film and another layer of dielectric substrate below the conductors. The closed-form analytical expressions for the effective dielectric constant ε_{eff} and the characteristic impedance Z_c for CPW are derived using conformal mapping techniques [84, 85]. This model has proved to be a good approximation for frequencies above $f = 1/(\mu_0 \sigma t s)$, where t, s, and σ are the thickness, half width of the CPW centre strip, and its conductivity, respectively [86]. In addition, due to the used of quasi-TEM approximation, the model is valid provided the lateral dimensions of the CPW (strip width $2s$ and gap size g) are less than one tenth of the wavelength in the line [86].

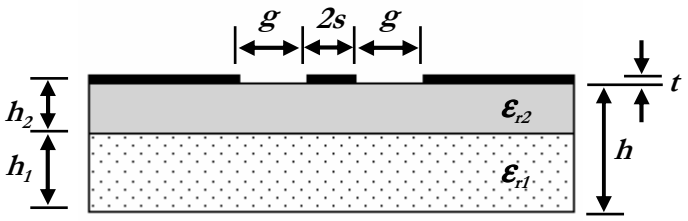

Figure 3.4.2: Multilayer CPW configuration.

The closed-form expressions for ε_{eff} and Z_c given in [84] are as follow.

$$\varepsilon_{eff} = 1 + (\varepsilon_{r1} - 1)q_1 + (\varepsilon_{r2} - \varepsilon_{r1})q_2 \tag{3.4.1}$$

$$Z_c = \frac{30\pi}{\sqrt{\varepsilon_{eff}}} \cdot \frac{K(k_0')}{K(k_0)} \tag{3.4.2}$$

where the filling factor q_i for $i = 1, 2$ is given by

$$q_i = \frac{1}{2}\frac{K(k_i)}{K(k_i')}\frac{K(k_0')}{K(k_0)} \tag{3.4.3}$$

$$k_0 = \frac{s}{s+g} \qquad k_i = \frac{\sinh[\pi s/2h_i]}{\sinh[\pi(s+g)/2h_i]}$$

$K(k)$ is the complete elliptic integral of the first kind, $K'(k) = K(k')$ and $k' = \sqrt{1-k^2}$. Approximations for elliptic integrals ratio of the first kind, $K(k)/K(k')$, can be found in Appendix A.

Some computational difficulties may be encountered when attempting to evaluate dielectric filling factors q_i for very thin ferroelectric layer, where the ratio of the line dimensions to the layer thickness becomes extremely large ($s, g >> h_i$). In this case, the limiting form [84] can be employed.

$$q_i = \frac{h_i}{2g}\frac{K(k_0')}{K(k_0)} \tag{3.4.4}$$

This multilayer CPW model will be used in Chapter 5 to predict the properties of the ferroelectric thin-film, as well as to determine the performance of the ferroelectric phase shifter.

3.4.2 Conductor-Backed Coplanar Waveguide

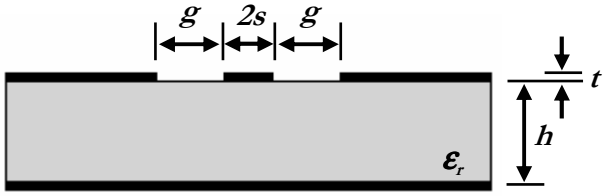

Figure 3.4.3: CBCPW configuration.

For a conductor-backed coplanar waveguide (CBCPW) with the structure shown in Figure 3.4.3, the closed-form expressions for ε_{eff} and Z_c are as follow [74, 84]:

$$\varepsilon_{eff} = 1 + (\varepsilon_r - 1)q \tag{3.4.5}$$

$$Z_c = \frac{60\pi}{\sqrt{\varepsilon_{eff}}} \cdot \left[\frac{K(k_1)}{K(k_1')} + \frac{K(k_0)}{K(k_0')} \right]^{-1} \tag{3.4.6}$$

$$q = \frac{K(k_1)}{K(k_1')} \left[\frac{K(k_1)}{K(k_1')} + \frac{K(k_0)}{K(k_0')} \right]^{-1} \tag{3.4.7}$$

$$k_0 = \frac{s}{s+g} \qquad k_1 = \frac{\tanh[\pi s/2h]}{\tanh[\pi(s+g)/2h]}$$

This single layer CBCPW model will be used in Chapter 6 to predict the performance of the tunable attenuator based on a single layer Duroid substrate.

3.4.3 Multilayer CBCPW

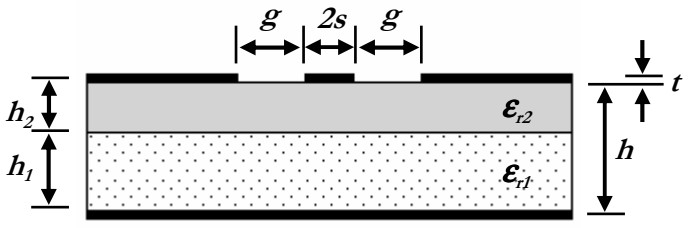

Figure 3.4.4: Multilayer CBCPW configuration.

For a multilayer CBCPW structure, as shown in Figure 3.4.4, the ε_{eff} can be expressed as [84]:

$$\varepsilon_{eff} = 1 + (\varepsilon_{r1} - 1)q_1 + (\varepsilon_{r2} - \varepsilon_{r1})q_2 \tag{3.4.8}$$

$$q_i = \frac{K(k_i)}{K(k_i')}\left[\frac{K(k_i)}{K(k_i')} + \frac{K(k_0)}{K(k_0')}\right]^{-1} \tag{3.4.9}$$

$$k_0 = \frac{s}{s+g} \qquad k_1 = \frac{\tanh[\pi s/2h_1]}{\tanh[\pi(s+g)/2h_1]} \qquad k_2 = \frac{\sinh[\pi s/2h_2]}{\sinh[\pi(s+g)/2h_2]}$$

Z_c is given in equation (3.4.6) with the use of ε_{eff} from equation (3.4.8). This multilayer CBCPW model will be used in Chapter 6 to predict the performance of the tunable attenuator based on ferroelectric thin-film.

3.4.4 Dielectric Loaded CBCPW

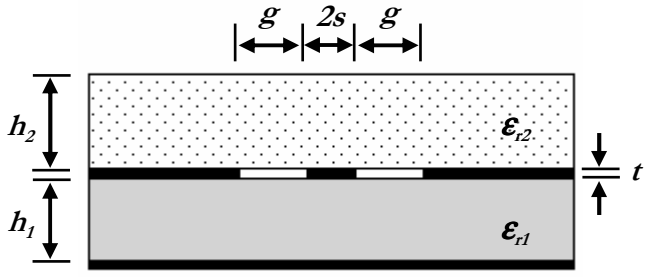

Figure 3.4.5: Dielectric loaded CBCPW configuration.

A dielectric loaded CBCPW structure, as shown in Figure 3.4.5, is composed of a dielectrics substrate ε_{r1} of thickness h_1 below the coplanar conductors, and

another dielectric substrate ε_{r2} of thickness h_2 above the coplanar conductors. The ε_{eff} can be expressed as [84]

$$\varepsilon_{eff} = 1 + (\varepsilon_{r1} - 1)q_1 + (\varepsilon_{r2} - 1)q_2 \tag{3.4.10}$$

where the dielectric filling factors $q_{1,2}$ and $k_{0,1,2}$ are the same as for a multilayer CBCPW structure, given in equation (3.4.9). Z_c is as shown in equation (3.4.6), with adoption of ε_{eff} from equation (3.4.10). This model will be employed and described in Chapter 6 to predict the performance of the phase shifter based on single layer Duroid substrate with other dielectric material placed on its top surface.

By utilising the aforementioned models, the gap width g as a function of strip width $2s$ can be found for a 50 Ω CPW and CBCPW line on multilayer (BST/MgO) and single layer (Duroid) substrates. These results are plotted in Figure 3.4.6.

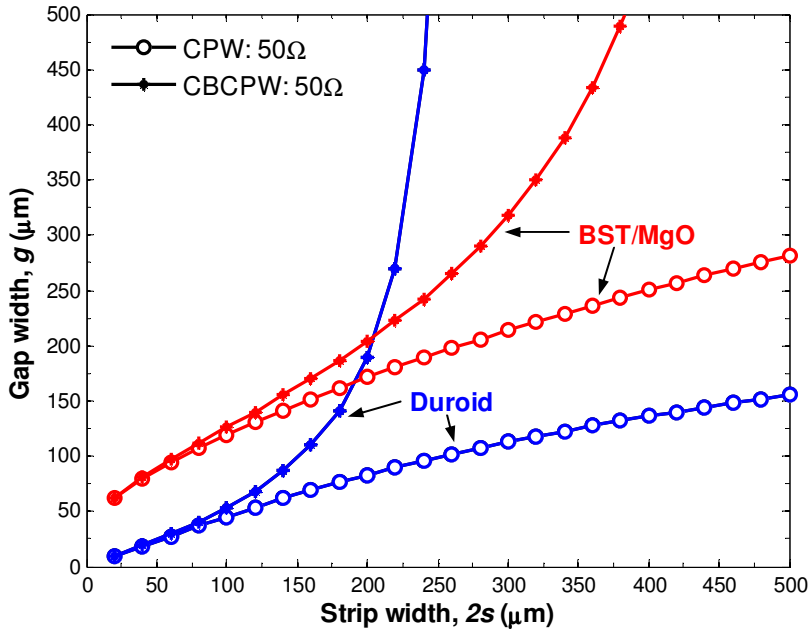

Figure 3.4.6: The strip width versus gap width curves for 50 Ω CPW and CBCPW. (BST/MgO, h_1=500μm, ε_{r1}=9.8, h_2=0.35μm, ε_{r2}=1800); (Duroid, h=254μm, ε_r=10.2)

When strip width $2s$ is less than 100 μm, where both the strip and gap widths were considerably smaller than the substrate thickness, the presence of the conductor backing had negligible effect on the characteristic impedance. The influence of the conductor-backing however became prominent as $2s$ increased. With the same dimensions, CBCPW had a lower characteristic impedance than CPW structure. In the region where $2s$ is greater than 200 μm, a dramatic increase in gap width was required for the CBCPW in order to maintain a 50 Ω line. This was because as gap width became comparable to substrate thickness, the electric field tended to converge between the strip and conducting backing instead of the gaps, thus resulting in the emerged of the microstrip-like mode (MSL) in the CBCPW line. In the situation where the gap is sufficiently wide, the MSL mode may dominate which results in the structure losing its flexibility to maintain a certain Z_c by adjusting the strip-to-gap ratio. The achievable impedance therefore reverts to that of a microstrip structure. In the case of the single layer Duroid substrate, the CBCPW line is 50 Ω only if the strip width is 240 μm. Therefore, any strip exceeding this cannot maintain a 50 Ω impedance by any means and results in a rapid divergence of the curve for the CBCPW line on 254 μm Duroid as shown in Figure 3.4.6. It should be noted that the accuracy of the quasi-TEM formulas employed could suffer if the gap width is too wide to be treated as a magnetic wall, hence the observed divergence may also be partly related to the failure of the formulation.

Several of the calculated parameters for CPW and CBCPW structures on single (Duroid) and multilayer (BST/MgO) substrates are listed in Table 3.4.1. These parameters will be used in the ferroelectric phase shifter and tunable attenuator described in Chapters 5 and 6. The results from Sonnet simulations are also included in the table for comparison.

In the Sonnet simulations, conductors were assumed to have zero thickness with infinite conductivity, and the simulation cell size was 2 μm. The values were obtained at 10 GHz. As detailed in the table, the calculated and simulated results showed a reasonably good agreement with one another.

Configuration	2s (μm)	g (μm)	Calculation method	ε_{eff}	Z_c (Ω)
CBCPW - Duroid (h=254μm, ε_r=10.2)	120	60	Conformal mapping Sonnet simulation	5.77 5.86	48.4 48.5
	60	120	Conformal mapping Sonnet simulation	5.79 5.94	71.4 71.3
CBCPW - BST/MgO (h_1=500μm, ε_1=9.8, h_2=0.35μm, ε_2=1800)	80	110	Conformal mapping Sonnet simulation	10.27 10.65	49.7 49.6
	20	40	Conformal mapping Sonnet simulation	20.27 20.65	39.7 39.8
CPW - BST/MgO (h_1=500μm, ε_1=9.8, h_2=0.35μm, ε_2=1800)	50	78	Conformal mapping Sonnet simulation	12.50 13.14	47.3 47.2

Table 3.4.1: Parameters obtained from conformal mapping calculations and Sonnet simulations.

3.5 CBCPW-to-Microstrip Transition

In order to characterise the microstrip structured circuits described in Chapter 6 using on-wafer coplanar waveguide (CPW) probes (a coplanar ground-signal-ground structure), a probing pad from CPW-to-microstrip transition is necessary.

There are primarily two types of CPW-to-microstrip transitions: via and via-less. A via transition directly interconnects the top layer CPW ground planes with the lower microstrip ground plane via conductor plated holes. Although via holes transitions are compact and broadband, complications with fabrication techniques and associated costs coupled with parasitic inductance problems has caused via holes transition not to be used to any great extent [87, 88]. Conversely, a via-less transition is realised by establishing a strong capacitive coupling between the top layer CPW probe ground and the lower microstrip ground. A number of researchers [89-92] have reported the development of via-less transition based on stepped patch and

stubs. The stepped patch transition often involves patterned lower ground plane or step structures, which complicates the design and fabrication.

A simple taper, via-less CBCPW-to-microstrip transition to allow probing of microstrip structures is developed by Zheng *et al.* [93] and subsequently optimised by Wang and Lancaster [94], is shown in Figure 3.5.1. This taper transition structure does not require any alteration or patterning on the lower ground plane and has proved to have a superior wideband capability compared to the radial stubs design, provided that the patch size of the CBCPW in-plane ground is properly optimised.

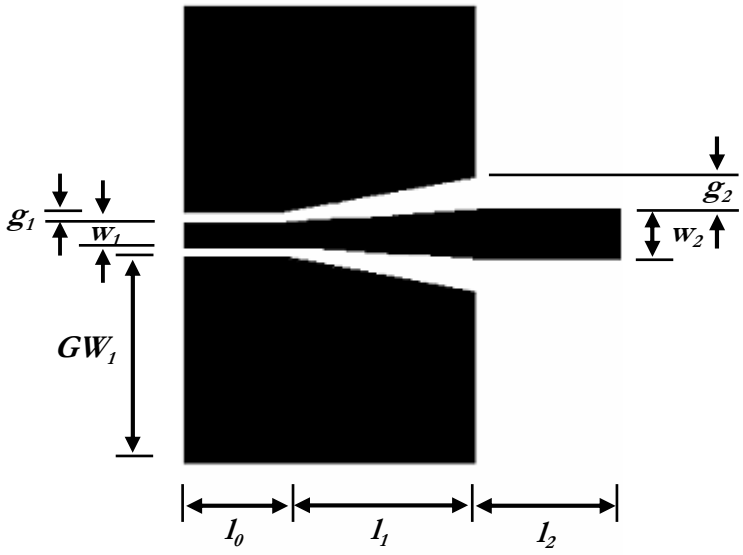

Figure 3.5.1: Layout of taper structure via-less CBCPW-to-microstrip transition.

The complete structure consists of a CBCPW section, a CBCPW-to-microstrip section, and a microstrip section. The 50 Ω coplanar line and a similar microstrip line often have different signal line widths. In the intermediate transition section, the width of the CBCPW signal strip w_1 is increased gradually to match the width of the microstrip w_2 whilst ensuring the strip-to-gap ratio (w/g) retains a constant 50 Ω characteristic impedance along the taper. Nonetheless, a good impedance-matched

transition does not guarantee continuous return currents or minimal reflections in the taper. In [94], the size of the CBCPW in-plane ground patches defined by GW_1, l_0, l_1 *and* g_2, is taken into design consideration. The size of the CBCPW in-plane ground should be sufficiently large to achieve a strong capacitive coupling between the CBCPW in-plane ground and the microstrip ground. Consequently, at high frequencies, the electrical reactance between the CBCPW in-plane ground and the microstrip ground will be sufficiently small to generate low impedance between the CBCPW in-plane ground and the microstrip ground contacts [92, 93]. However, to prevent parasitic ground plane patch resonances in a parallel-plate mode emerging in the band of interest, the CBCPW in-plane ground width, GW_1 should be much smaller than $\lambda/2$ [75].

In order to facilitate on-wafer measurements of the circuits described in Chapter 6, two CBCPW-to-microstrip transitions are designed and are laid out in back-to-back configuration in order to be tested. The simulated S_{11} and S_{21} for back-to-back CBCPW-to-microstrip transitions on BST/MgO and Duroid substrates are shown in Figure 3.5.2. The inset shows the layout of the back-to-back transition configuration. The metallisation layer is entirely underside of the substrate to provide the ground plane. The simulation cell size, substrate and conductor parameters used were identical to the parameters in the simulation of microstrip bend and tee-junction previously used in plotting Figure 3.3.7 and Figure 3.3.10.

As expected, high return losses were observed at low frequencies due to the large electrical reactance of the capacitive coupling between the CPW probe ground and microstrip ground, resulting in open-circuit behaviour. With Duroid substrate, the return loss observed was better than 24 dB between 2.5 to 8.5 GHz while transitions on the BST/MgO substrate only achieved a return loss of better than 15 dB in the same frequency band. This was attributed to the size of the CBCPW in-plane ground patches on the latter substrate material, which were insufficiently large to provide a strong capacitance between the CPW ground plane and microstrip ground plane, due to the limitation of the usable area on a 1×1 cm^2 BST/MgO substrate.

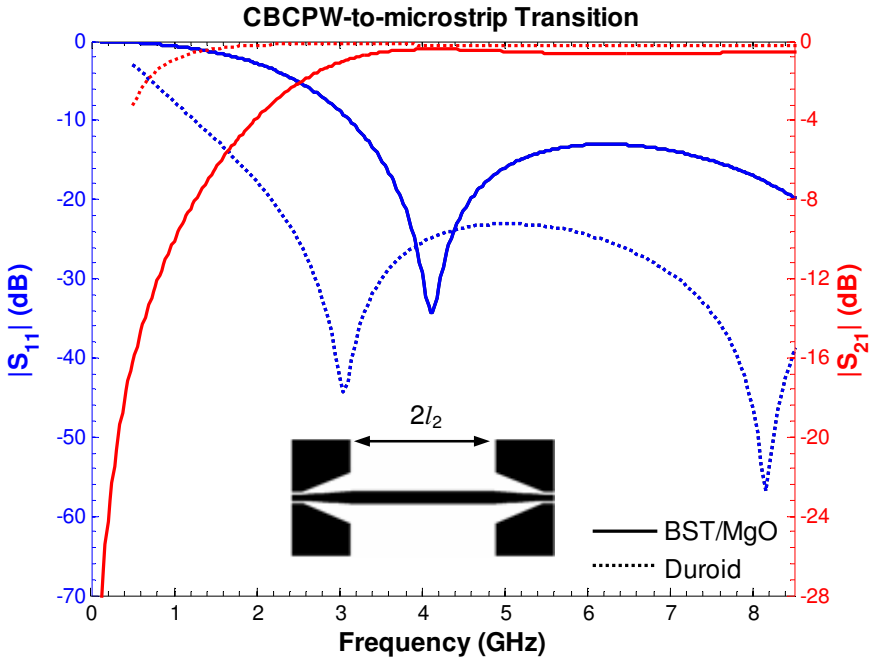

Figure 3.5.2: Simulated scattering-parameters of back-to-back CBCPW-to-microstrip transition on BST/MgO (solid line) and Duroid (dotted line) substrate. (BST/MgO: GW_1=3.86mm, l_0=40μm, l_1=840μm, l_2=3.11mm, w_1=80μm, g_1=100μm, w_2=400μm, g_2=1.7mm); (Duroid: GW_1=5.61mm, l_0=510μm, l_1=990μm, l_2=4.11mm, w_1=120μm, g_1=60μm, w_2=240μm, g_2=180μm)

3.6 Attenuation in Microstrip and CPW

The losses in a transmission line are primarily contributed by three components: conductor (or ohmic) loss α_c, dielectric loss α_d and radiation loss α_r. The total attenuation often expressed in decibels per metre (dB/m) and is given by

$$\alpha = \alpha_c + \alpha_d + \alpha_r \tag{3.6.1}$$

This section briefly covers the losses in microstrip and CPW variants. Where available, closed-form analytical expressions for respective structures will be shown and reviewed.

3.6.1 Conductor Loss

Conductor losses are a result of several factors relating to the properties of the metallic material which make up the conducting strip and ground plane, namely, finite conductivity, skin effect and surface roughness of the conductors. For the microstrip, the closed-form expression for the attenuation due to conductor loss (dB/m) given by [95] is

$$\alpha_c^{MS} = \frac{8.686 \cdot R_s (A_1 + A_2)}{2Z_c} \tag{3.6.2}$$

A_1, A_2 and the surface resistance R_s in ohms per square for conducting strip and ground plane are given by

$$A_1 = \frac{L_R}{w}\left[\frac{1}{\pi} + \frac{1}{\pi^2}\ln\left(\frac{4\pi w}{t}\right)\right]$$

$$A_2 = \frac{1}{h \cdot \left(\frac{w}{h} + 5.8 + 0.03\frac{h}{w}\right)} \qquad 0.1 \le \frac{w}{h} \le 10$$

$$L_R = 1 \qquad \text{for } \frac{w}{h} \le 0.5$$

$$L_R = 0.94 + 0.132\frac{w}{h} - 0.0062\left(\frac{w}{h}\right)^2 \qquad \text{for } 0.5 \le \frac{w}{h} \le 10$$

$$R_s = \sqrt{\frac{\omega\mu_0}{2\sigma}} \tag{3.6.3}$$

where Z_c is the characteristic impedance of the microstrip with width w, R_s represents the surface resistance for the conducting strip and ground plane, σ is the conductivity of the conductors, μ_0 is the permeability of free space, and ω is the angular frequency. According to [95], equation (3.6.2) predicts somewhat higher

theoretical attenuation than that obtained from the formula developed by Pucel *et al.* [96] using Wheeler's incremental inductance rule and the equation appears to be in better agreement with experimental results.

For CPW structure, the attenuation caused by conductor loss is given in [97]:

$$\alpha_c^{CPW} = \frac{8.686 \cdot R_s \sqrt{\varepsilon_{eff}}}{480\pi K(k_0)K(k_0')(1-k_0^2)} \cdot \left\{ \frac{1}{a}\left[\pi + \ln\left(\frac{8\pi a(1-k_0)}{t(1+k_0)}\right)\right] + \frac{1}{b}\left[\pi + \ln\left(\frac{8\pi b(1-k_0)}{t(1+k_0)}\right)\right]\right\} \tag{3.6.4}$$

where $a = s$, $b = s + g$, and $k_0 = a/b$. R_s is the surface resistance given in equation (3.6.3) and Z_c is the characteristic impedance of CPW line. The above equation assumes the metal thickness as $t > 3\delta$, $t << a$ and $(b - a)$, where δ is the skin depth, given as

$$\delta = \sqrt{\frac{2}{\omega\mu_0\sigma}} \tag{3.6.5}$$

Equation (3.6.4) is valid for symmetric CPW configurations with finite and infinite dielectric thicknesses and for multilayered structures as well [77].

There has not been any formulation available to evaluate the conductor loss of CBCPW in the literature to date. An analytical expression which accounts for the attenuation attributed by the conductor-backed ground of CBCPW has been developed by Wang [98] using incremental-inductance method. The simplified expression can be expressed as:

$$\alpha_c^{CBCPW} = \frac{8.68}{60\pi^2\mu_0 c_0} R_s \varepsilon_{eff} Z_c^{CBCPW} \left(X_1 Y_1 + X_2 Y_2\right) \tag{3.6.6}$$

X_1, Y_1, X_2 and Y_2 together with the detailed derivation are given in Appendix B for completeness.

3.6.2 Dielectric Loss

With the assumption of isotropic substrate, the attenuation due to the dielectric loss in a microstrip can be determined by [77, 95]

$$\alpha_d^{MS} = \frac{8.686\pi}{c_0}\frac{\varepsilon_r}{\sqrt{\varepsilon_{eff}}}\left(\frac{\varepsilon_{eff}-1}{\varepsilon_r-1}\right)\tan\delta\cdot f \quad \text{(dB/m)} \tag{3.6.7}$$

where tan δ denotes the loss tangent of the dielectric substrate, and f is the operating frequency. The effective dielectric constant ε_{eff} is given by equation (3.3.1).

In the case of a multilayer CPW structure, as shown in Figure 3.4.2, the total dielectric losses introduced by the dielectric substrate ε_{r1} with tan δ_1, and ferroelectric film $\varepsilon_{r2}(E, T)$ with tan $\delta_2(E, T)$ can be approximated by [99]

$$\alpha_d^{CPW} = \frac{8.686\pi}{c_0\sqrt{\varepsilon_{eff}}}\left[\varepsilon_{r1}\tan\delta_1(q_1-q_2)+\varepsilon_{r2}(E,T)\cdot\tan\delta_2(E,T)\cdot q_2\right]\cdot f \tag{3.6.8}$$

where ε_{eff} and the filling factors $q_{1,2}$ are given by equation (3.4.1) and equation (3.4.3), respectively.

3.6.3 Radiation Loss

An ideal microstrip, being open to a semi-infinite air space, tends to radiate energy. These radiation losses depend on the dielectric constant, the thickness of substrate, and the circuit geometry of the microstrip. With the use of high-dielectric-constant or thin thickness substrate, radiation losses can be reduced as most of the EM field is concentrated in the dielectric between the conducting strip and the ground plane, with minimal energy radiating in the air space.

In the case of CPW structure, the attenuation due to radiation losses is usually dominant at high frequencies (typically above several tens of gigahertz) for line

dimensions in the order of a few tens of microns [100, 101]. As the operating frequency range of the ferroelectric phase shifter and tunable attenuator described in Chapter 5 and 6 is only up to 10 GHz, the radiation loss is negligibly small compared to conductor and dielectric loss of the structure, and hence, can be neglected.

The attenuation of multilayer CPW line calculated using equation (3.6.4) and (3.6.8) are plotted in Figure 3.6.1 for different strip widths 2*s*. Substrates used are a layer of BST ferroelectric (ε_2 = 1800, tan δ_2 = 0.06 or 0.12, h_2 = 0.35 μm) on top of an MgO substrate (ε_1 = 9.8, tan δ_1 = 1×10^{-4}, h_1 = 500 μm). A silver metallisation of thickness 300 nm and conductivity of 6.17 × 10^7 S/m is assumed. The gap width *g* is fixed at 54 μm.

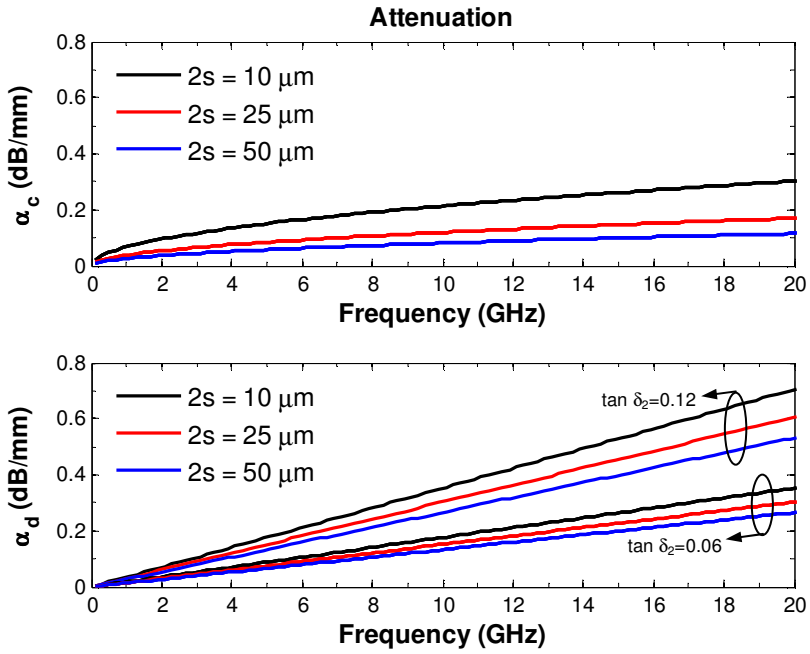

Figure 3.6.1: Calculated conductor, α_c and dielectric loss, α_d for CPW line on BST/MgO substrate with different strip widths. (g=54μm)

In Figure 3.6.1, the radiation loss of CPW can be neglected due to the large effective dielectric constant and the much smaller line width of CPW compared with EM wavelength. The dielectric losses from the MgO substrate can generally be

disregarded due to its low-loss properties (loss tangent < 10^{-4}). Consequently, the total loss of the CPW is primarily contributed by the conductor loss and dielectric loss in the ferroelectric layer. It was observed that the losses were inversely proportional to the strip width 2*s*. α_d was comparable to α_c due to the very high loss tangent of the ferroelectric layer.

Figure 3.6.2 depicts the conductor loss of CPW and CBCPW lines with the same dimensions (fixed gap width *g* of 54 μm and different strip widths 2*s*) on BST/MgO substrates, calculated using the incremental-inductance method in (3.6.6). Solid and dotted lines represent the CPW and CBCPW structures, respectively. With identical substrate and conductor parameters as the earlier plot, it was found that the additional conductor-backed ground plane attributed to approximately 14-25% increased of conductor losses.

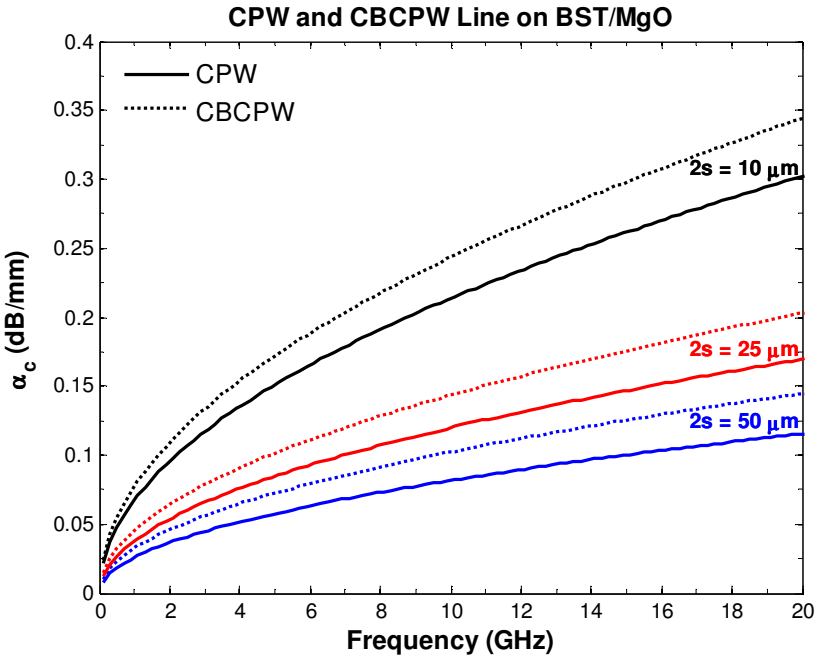

Figure 3.6.2: Calculated conductor loss for CPW and CBCPW line on BST/MgO substrate with different strip widths. (*g*=54μm)

3.6.4 Parasitic Modes in CBCPW

Apart from the aforementioned losses, another vital concern in CBCPW circuits in practice is the possible excitation of other unwanted parasitic modes, namely the slotline mode, parallel-plate and microstrip mode [75, 102-104].

3.6.4.1 Slotline Mode

A discontinuity or asymmetry in the transmission line such as right-angle bends and T-junctions often excites the slotline mode in the coplanar circuits [102, 103]. Slotline mode is induced by the unequal potentials between the two in-plane grounds alongside of the signal line. These unbalanced in-plane ground were a result of the difference in path length between the inner slot and the outer slot of the guided CPW mode, as illustrated in Figure 3.6.3(a).

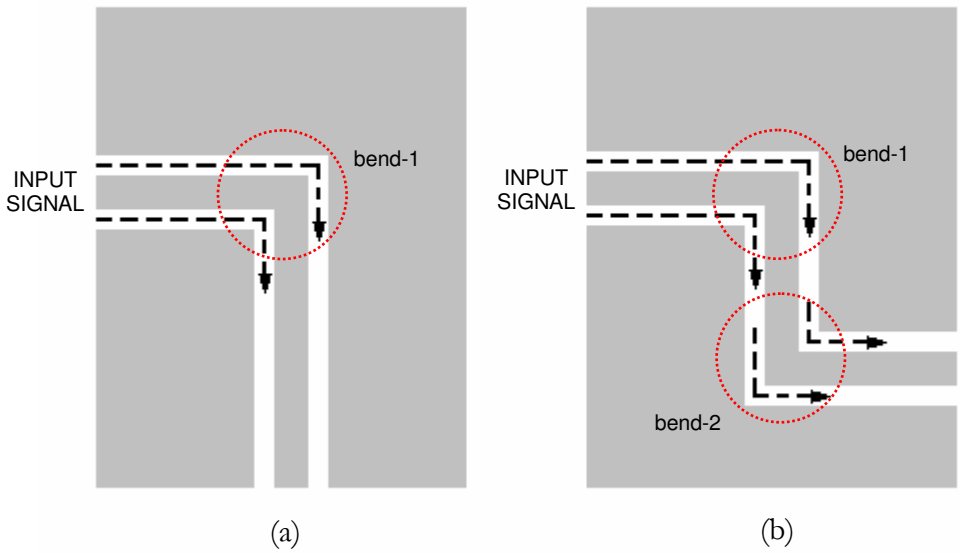

Figure 3.6.3: Illustration of the signal paths in the slots of a CPW line. The transient signals in the two slots are asynchronous after travelling through (a) a single bend, but may be synchronised again after passing through (b) the pair of oppositely oriented bends [98].

There are a number of possible ways to suppress this mode. Some are by means of imposing equal potentials on the unbalanced grounds; others are by compensating the path difference or attempt to attenuate the slotline mode while maintaining the dominant CPW mode. The conventional way to suppress the slotline mode in CPW circuits is the use of wire-bond or air-bridge, which is essentially a conductor crossovers interconnecting the unbalanced in-plane grounds [105]. This method, however, possesses high losses and may trigger the occurrence of resonances between bonds or bridges. Further, such method is costly, especially for a complex CPW circuit where a large number of crossovers may be required.

To compensate for the path difference, one method is to slow down the wave travelling in the inner slot, which is shorter in length, so that it emerges from the bend in phase with the wave in the outer slot. This can be achieved by placing a dielectric medium over the inner slot, also known as dielectric overlay [103]. Although such method has shown to be broad band capable, the use for a complex circuit with many bends has found to be impractical. In addition, the introduction of dielectric overlay inevitably increases the loss.

Alternatively, the asynchronous signal after travelling through the slots of different path length can be re-synchronised again after passing through a similar but oppositely oriented bends [98], as illustrated in Figure 3.6.3(b). Such method re-established the symmetric CPW mode, although some signal distortion and reflection experienced at the bends is irreversible.

3.6.4.2 Parallel-plate Mode

There exists two dominant parasitic modes in CBCPW structure: CPW and parallel-plate mode below a critical frequency [75], as illustrated in Figure 3.6.4. If the in-plane ground of a CBCPW is sufficiently wide and has a finite dielectric thickness, a parallel-plate mode may be established between the upper in-plane and lower ground plane. This undesirable parallel-plate mode, if unsuppressed, could result in deterioration of circuit performance. One method to suppress this mode is to ensure proper interconnection between the upper in-plane and lower ground plane [106,

107]. Alternatively, Tien *et al.* [75] reported that the detrimental phenomenon could also be avoided by ensuring that the physical dimensions of the CBCPW circuit were significantly smaller than half the EM wavelength.

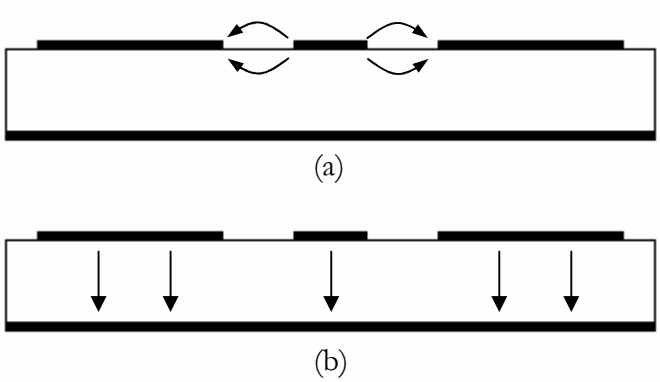

Figure 3.6.4: Dominant modes in a CBCPW structure with infinite-width in-plane ground and finite-width substrate. (a) CPW mode, (b) parallel-plate mode [75].

3.6.4.3 Microstrip-like Mode (MSL)

As opposed to parallel-plate mode, in the case where the in-plane ground of the CBCPW line is too narrow or that the gap width is comparable to substrate thickness, a mode conversion from CPW to microstrip-like mode may be established. This mode results in the structure losing its CPW flexibility to maintain certain impedance by adjusting the strip-to-gap ratio. The achievable impedance would revert to that of a microstrip structure.

Table 3.6.1 summarises the possible excitation of parasitic modes in CBCPW.

	Finite substrate thickness		**Infinite substrate thickness**
	Infinite in-plane ground	**Finite in-plane ground**	
CBCPW	Parallel-plate mode	Slotline mode Microstrip-like mode	-

Table 3.6.1: Summary of the possible excitation of parasitic modes in CBCPW.

3.7 Conclusions

Microstrip and variants of coplanar waveguide transmission lines have been briefly reviewed. In particular, models of single and multilayer configurations have been presented. These models, which employ quasi-static analysis and conformal mapping technique, will be used to predict the properties of ferroelectric thin-film as well as to predict the performance of the ferroelectric phase shifter and tunable attenuator in Chapters 5 and 6.

In the following chapter, the work on how the finite difference method (FDM), a computational technique, is modified to suit the evaluation of ferroelectric transmission lines will be discussed. The results will be verified and compared with the existing closed-form analytical models showed in this chapter.

Chapter 4

Finite Difference Method

4.1 Introduction

Work on adapting the iterative computational based finite difference method (FDM) to enable the evaluation of both microstrip and several variants of coplanar waveguides composed of ferroelectric layers is discussed in this chapter. The spatial variation of the ferroelectric dielectric constant is often ignored in the literature and is considered here in the calculation of the effective dielectric constant ε_{eff} and characteristic impedance Z_c of the transmission lines. The results were verified and compared with the closed-form analytical models detailed in the previous chapter. They are used to predict the performance of ferroelectric phase shifter and tunable attenuator to be described in Chapters 5 and 6.

Conventional finite difference equations cannot be used for studying ferroelectric-based transmission lines as the variation of dielectric constant with electric field complicates the problem. Here, the derivation of a modified finite difference equation which is required to account for the electric-field dependency of

the ferroelectric material will be presented.

The new finite difference calculation accommodates the spatial variation of the dielectric constant within the ferroelectric layer as opposed to the often-employed solution of assuming a fixed value [2, 99, 108, 109]. Application of this newly derived ferroelectric finite difference method to calculate the potential distribution across a number of different ferroelectric-based transmission line configurations is demonstrated. The results show the dielectric constant as being small in the vicinity of the edges of the signal line and increases with distance from the signal line due to the diminishing electric field strength.

4.2 Outline of the Finite Difference Method

The finite difference method (FDM), sometimes called the relaxation method, is a well-known computational technique for finding the solution to a boundary value problem [110-113], and is particularly suited for the evaluation of the cross-sectional field distribution of a transmission line. This iterative technique makes use of an arbitrary "fictitious" boundary drawn close to the regions of physical interest. The region within the specified boundary is first divided into a grid of nodes called mesh points. Figure 4.2.1 depicts the mesh points within the cross section of a microstrip.

An initial guess of the potential is made on this boundary as well as for all interior mesh points. Appropriate finite difference equations are applied to each of the mesh points within the boundary, thereby creating a set of simultaneous equations. This set of simultaneous equations is then solved using an iterative process, where the potential ϕ at each point are calculated from its surrounding potential. Each step of this process involves evaluating a new potential at each node of the grid from the finite difference equation, and using this new value in the calculation of all subsequent potentials. This iterative process ends when there are no further changes in potential in the entire region, that is, when the finite difference equations are solved exactly and satisfied at every node. The magnitude of the

electric field, E in this case and permittivity $\varepsilon(E)$ at each node on the ferroelectric-based structure can then be computed from the potentials.

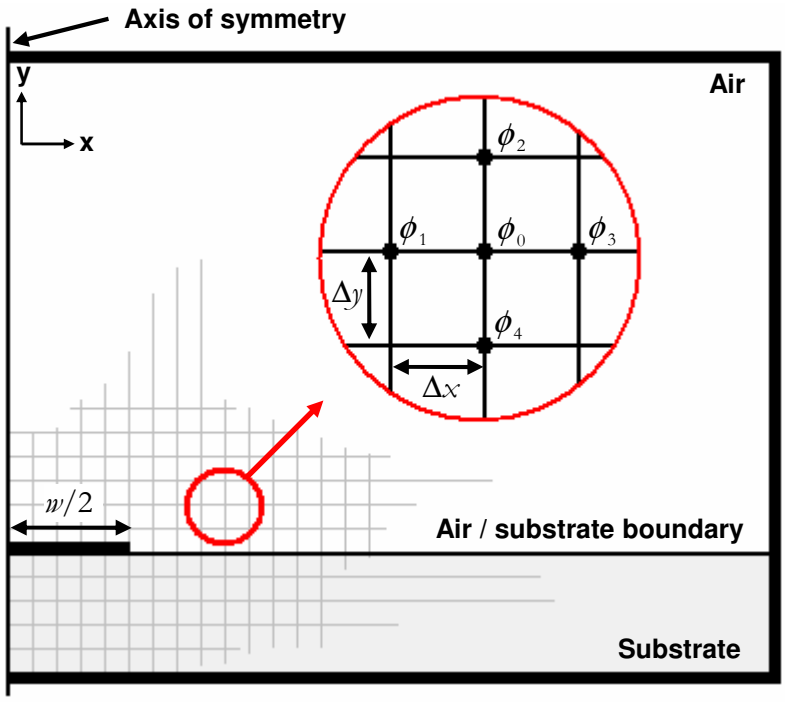

Figure 4.2.1: Illustration of mesh points on the cross-sectional microstrip line.

In order to obtain a more accurate result for any open space or boundary structure (such as a microstrip), the fictitious boundary of the structure is moved sufficiently far from the conductors such that the computed solutions are virtually independent of boundary positions, with boundary walls essentially equivalent to 0 V. Nonetheless, such boundaries however, also known as the Dirichlet boundary condition, often create a large number of grid points which significantly increases the computational time. In an attempt to avoid this problem, several researchers have proposed imposing a fictitious boundary of unknown potential values having distances much closer to the region of interest [110, 111]. Instead of a given boundary solution, the potential values on such boundaries were specified from its normal derivative and this is known as the Neumann boundary condition [110]. To further reduce memory requirements and computational time, the potentials within

the boundary can be obtained by solving half of the whole structure through consideration of axis of symmetry as a magnetic wall, as shown in Figure 4.2.1.

In the FDM, the two-dimensional Laplace's equation is solved along the cross section of the transmission line to obtain the potential ϕ at every node and then calculate the effective dielectric constant ε_{eff} and characteristic impedance Z_c. This is achieved by expanding the Laplace's equation given below to form a simultaneous difference equation.

$$\nabla^2\phi = \frac{\partial^2\phi}{\partial x^2} + \frac{\partial^2\phi}{\partial y^2} = 0 \tag{4.2.1}$$

The following sections will show how the difference equation can be derived from the Laplace equation in the cases of equal and unequal grid size.

4.2.1 Equal-arm Grid

Figure 4.2.2 illustrates the equal-arm grid mesh points where ϕ_0 is the potential at the point of interest surrounded by ϕ_1, ϕ_2, ϕ_3, and ϕ_4. The difference equation for this five-point equal-arm grid, where $\Delta x = \Delta y = h$, is [110, 111];

$$\begin{aligned}\frac{\partial^2\phi}{\partial x^2} + \frac{\partial^2\phi}{\partial y^2} &= \frac{\left(\frac{\phi_3 - \phi_0}{\Delta x}\right) - \left(\frac{\phi_0 - \phi_1}{\Delta x}\right)}{\Delta x} + \frac{\left(\frac{\phi_2 - \phi_0}{\Delta y}\right) - \left(\frac{\phi_0 - \phi_4}{\Delta y}\right)}{\Delta y} \\ &= \frac{\phi_1 + \phi_2 + \phi_3 + \phi_4 - 4\phi_0}{h^2}\end{aligned} \tag{4.2.2}$$

Thus, the finite difference equation at each mesh point is given by:

$$\phi_0 = \frac{1}{4}\left(\phi_1 + \phi_2 + \phi_3 + \phi_4\right) \tag{4.2.3}$$

According to Laplace's equation, if the potential ϕ_1, ϕ_2, ϕ_3, and ϕ_4 are known, the

potential ϕ_0 is as given by the above equation. In other words, the physical significance of Laplace's equation is simply that the potential at a point must be the average of the potential at four surrounding points.

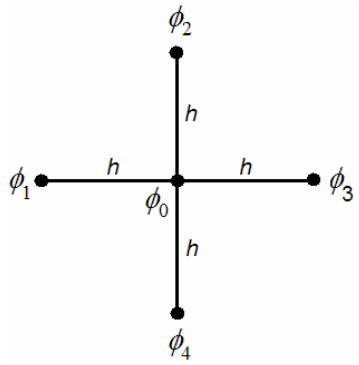

Figure 4.2.2: Equal-arm grid mesh points.

4.2.2 Unequal-arm Grid

In circumstances where the boundary of the domain of interest (where a solution of ϕ is desired) does not fit to the regular mesh structure required by the equal-arm formula (3.3.1), a very fine mesh may be utilised to minimise distortion of the shape of the boundary. Alternatively, a different finite difference formula for a five-point unequal-arms grid can be used [110].

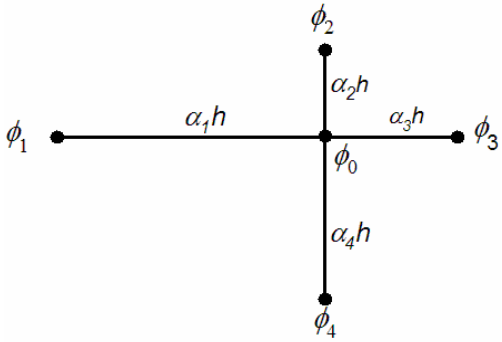

Figure 4.2.3: Unequal-arm grid mesh points.

For the geometry shown in Figure 4.2.3 the difference representation of the Laplace's equation is given by,

$$\begin{aligned}\nabla^2\phi &= \frac{\partial^2\phi}{\partial x^2}+\frac{\partial^2\phi}{\partial y^2} \\ &= \frac{2}{h^2}\left[\frac{\phi_1}{\alpha_1(\alpha_1+\alpha_3)}+\frac{\phi_3}{\alpha_3(\alpha_1+\alpha_3)}+\frac{\phi_2}{\alpha_2(\alpha_2+\alpha_4)}+\frac{\phi_4}{\alpha_4(\alpha_2+\alpha_4)}\right] \\ &\quad -\left(\frac{1}{\alpha_1\alpha_3}+\frac{1}{\alpha_2\alpha_4}\right)\phi_0\end{aligned} \tag{4.2.4}$$

4.3 Ferroelectric Finite Difference Equation

The unevenly distributed electric field applied across the microstrip and coplanar waveguides (due to the inhomogeneous dielectric-air media) used in this work causes an associated uneven dielectric constant distribution within the ferroelectric layer, which varies according to the magnitude of the applied electric field. This distinctive property of ferroelectric materials restricts the use of conventional finite difference equations to accurately determine the potential distribution, effective dielectric constant ε_{eff} and characteristic impedance Z_c of the transmission lines, hence the motivation for the research to incorporate an electric-field dependency in the formulation described in this section.

In a charge free region, as illustrated in Figure 4.3.1, the two dimensional Gauss' Law is given by,

$$\nabla \cdot D = \frac{\partial D_x}{\partial x}+\frac{\partial D_y}{\partial y} = 0 \tag{4.3.1}$$

where D is electric flux density. In the x-direction, D can be written as:

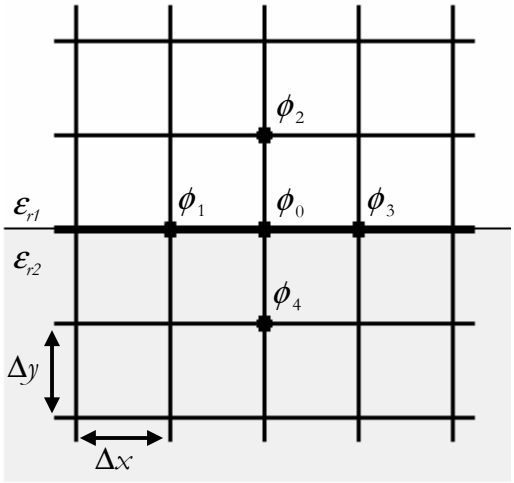

Figure 4.3.1: Illustration of mesh points on the boundary.

$$D_x = \varepsilon(E_x)E_x = \varepsilon_x E_x \tag{4.3.2}$$

where E is electric field of the ferroelectric material. Partially differentiating (4.3.2) gives:

$$\begin{aligned}\frac{\partial D_x}{\partial x} &= E_x \frac{\partial \varepsilon_x}{\partial x} + \varepsilon_x \frac{\partial E_x}{\partial x} \\ &= E_x \frac{\partial \varepsilon_x}{\partial E_x}\frac{\partial E_x}{\partial x} + \varepsilon_x \frac{\partial E_x}{\partial x}\end{aligned} \tag{4.3.3}$$

where $\partial\varepsilon_x / \partial E_x$ is a characteristic of the ferroelectric material. Electric field in x-direction as expressed in finite difference form is given by

$$E_x = -\nabla\phi_x = \frac{\phi_3 - \phi_1}{2\Delta x} \tag{4.3.4}$$

Hence,

$$\frac{\partial E_x}{\partial x} = -\nabla^2 \phi_x = \frac{\phi_1 + \phi_3 - 2\phi_0}{\Delta x^2} \tag{4.3.5}$$

Substitution of (4.3.4) and (4.3.5) into (4.3.3) gives:

$$\frac{\partial D_x}{\partial x} = \frac{\partial \varepsilon_x}{\partial E_x} \cdot \left(\frac{\phi_3 - \phi_1}{2\Delta x} \right) \cdot \left(\frac{\phi_1 + \phi_3 - 2\phi_0}{\Delta x^2} \right) + \varepsilon_x \left(\frac{\phi_1 + \phi_3 - 2\phi_0}{\Delta x^2} \right) \tag{4.3.6}$$

Similarly in *y*-direction:

$$\frac{\partial D_y}{\partial y} = \frac{\partial \varepsilon_y}{\partial E_y} \cdot \left(\frac{\phi_2 - \phi_4}{2\Delta y} \right) \cdot \left(\frac{\phi_2 + \phi_4 - 2\phi_0}{\Delta y^2} \right) + \varepsilon_y \left(\frac{\phi_2 + \phi_4 - 2\phi_0}{\Delta y^2} \right) \tag{4.3.7}$$

Assuming $\Delta x = \Delta y = h$ and using (4.3.1), the special finite difference equation for ferroelectric-based transmission lines at each mesh point is

$$\phi_0 = \frac{K_x \left(\phi_3^2 - \phi_1^2 \right) + K_y \left(\phi_2^2 - \phi_4^2 \right) + 2h\varepsilon_x (\phi_1 + \phi_3) + 2h\varepsilon_y (\phi_2 + \phi_4)}{2\left(K_x (\phi_3 - \phi_1) + K_y (\phi_2 - \phi_4) \right) + 4h\left(\varepsilon_x + \varepsilon_y \right)} \tag{4.3.8}$$

where $K_x = \partial \varepsilon_x / \partial E_x$ and $K_y = \partial \varepsilon_y / \partial E_y$. Note that this equation is reduced to constant dielectric materials by taking $K_x = K_y = 0$.

The inhomogeneous structure of the microstrip and different coplanar waveguides detailed in Chapters 5 and 6 dictates that the potential distribution needs to be computed across several different media having dissimilar dielectric constants. To account for this potential discontinuity, three regions are defined on which different finite difference equations will be used. These regions are defined according to location of the point of interest, whether it lies;

I. within the ferroelectric layer,
II. in air, within substrate, or on the air/substrate boundary,
III. on the air/ferroelectric or ferroelectric/substrate boundary.

While the technique proposed can be easily applied to anisotropic ferroelectric materials, for simplicity, the analysis given below assumes that the ferroelectric material and substrate used to be isotropic, where their electrical properties do not vary with direction, i.e. $\varepsilon_x = \varepsilon_y$ and $K_x = K_y$ and therefore the results are only approximate. Nonetheless, the approximation is sufficiently valid as the applied electric field across the geometry of the ferroelectric thin film in this work was predominantly in one direction only. The finite difference equations for the three cases are as follows;

Case I:

Point lies within the ferroelectric layer: $\varepsilon_x = \varepsilon_y = \varepsilon_f$, and $K_x = K_y = K_f = \partial\varepsilon_f/\partial E$.

$$\phi_0 = \frac{K_f\left(\phi_3^{\,2} - \phi_1^{\,2} + \phi_2^{\,2} - \phi_4^{\,2}\right) + 2h\varepsilon_f\left(\phi_1 + \phi_3 + \phi_2 + \phi_4\right)}{2K_f\left(\phi_3 - \phi_1 + \phi_2 - \phi_4\right) + 8h\varepsilon_f} \tag{4.3.9}$$

Case II:

Point lies in air, within a fixed dielectric constant substrate, or on the air/substrate boundary: ($\varepsilon_x = \varepsilon_y$, and $K_x = K_y = 0$)

$$\phi_0 = \frac{1}{4}\left(\phi_1 + \phi_2 + \phi_3 + \phi_4\right) \tag{4.3.10}$$

Case III:

Point lies on the air/ferroelectric or ferroelectric/substrate boundary:

$$\phi_0 = \frac{K_a\left(\phi_3^{\,2} - \phi_1^{\,2}\right) + \left(\phi_2 - \phi_4\right)\left(K_1\phi_2 + K_2\phi_4\right) + 2h\left[\varepsilon_{r1}\phi_2 + \varepsilon_{r2}\phi_4 + \varepsilon_a\left(\phi_1 + \phi_3\right)\right]}{2K_a\left(\phi_3 - \phi_1 + \phi_2 - \phi_4\right) + 8h\varepsilon_a} \tag{4.3.11}$$

where ε_{r1} and ε_{r2} is the upper and lower dielectric, respectively, $K_1 = \partial\varepsilon_{r1}/\partial E$ and $K_2 = \partial\varepsilon_{r2}/\partial E$. The dielectric constant along the boundary is then taken to be the average

of the two, $\varepsilon_a = (\varepsilon_{r1} + \varepsilon_{r2})/2$ and $K_a = (K_1 + K_2)/2$.

Thus, for an air/ferroelectric boundary where the upper dielectric is air, $\varepsilon_{r1} = 1$ and the lower dielectric is the ferroelectric material, $\varepsilon_{r2} = \varepsilon_f$, by substituting $\varepsilon_a = (1 + \varepsilon_f)/2$ and $K_a = K_f/2$ into (4.3.11) gives

$$\phi_0 = \frac{\frac{K_f}{2}\left(\phi_3^{\,2} - \phi_1^{\,2}\right) + (\phi_2 - \phi_4)(K_f\phi_4) + 2h\left(\phi_2 + \varepsilon_f\phi_4\right) + h\left(1 + \varepsilon_f\right)(\phi_1 + \phi_3)}{K_f(\phi_3 - \phi_1 + \phi_2 - \phi_4) + 4h\left(1 + \varepsilon_f\right)} \tag{4.3.12}$$

Similarly, for a ferroelectric/substrate boundary where the upper dielectric is the ferroelectric material, $\varepsilon_{r1} = \varepsilon_f$ and the lower dielectric is a fixed dielectric constant substrate, ε_{r2}, by substituting $\varepsilon_a = (\varepsilon_f + \varepsilon_{r2})/2$ and $K_a = K_f/2$ into (4.3.11) gives

$$\phi_0 = \frac{\frac{K_f}{2}\left(\phi_3^{\,2} - \phi_1^{\,2}\right) + (\phi_2 - \phi_4)(K_f\phi_2) + 2h\left(\varepsilon_f\phi_2 + \varepsilon_{r2}\phi_4\right) + h\left(\varepsilon_f + \varepsilon_{r2}\right)(\phi_1 + \phi_3)}{K_f(\phi_3 - \phi_1 + \phi_2 - \phi_4) + 4h\left(\varepsilon_f + \varepsilon_{r2}\right)} \tag{4.3.13}$$

For the metal boundary, the potential on the signal conducting strip is the applied voltage V having an arbitrary, non-zero value whilst conversely, 0 V was specified for the ground conducting plane.

With the assumption of TEM mode of propagation in the transmission lines, the transmission parameters, namely the effective dielectric constant ε_{eff} and characteristic impedance Z_c, are evaluated as follows.

$$\varepsilon_{eff} = \frac{C}{C_0} \qquad Z_c = \frac{1}{c_o\sqrt{CC_0}} \tag{4.3.14}$$

where c_o is the velocity of light in free space (~3 x 10^8 ms^{-1}), C_0 and C is the line capacitance per unit length for air-filled and dielectric/ferroelectric-filled transmission line respectively. Calculation of the line capacitance is computed from the potential distribution obtained through Gauss' law, and the total charge enclosed

by surface S which can be expressed as;

$$q = \oint_S \varepsilon E_n \cdot dS = -\oint_c \varepsilon \cdot \nabla \phi \cdot dc = -\oint_c \varepsilon \cdot \frac{\partial \phi}{\partial n} \cdot dc \tag{4.3.15}$$

where E_n is the magnitude of the normal electric field at each node calculated from the potentials on adjacent nodes. The closed surface S in (4.3.15) was replaced by the closed contour c resulting in a charge q in coulombs per unit length. Figure 4.3.2 illustrates the closed contour c of a microstrip. With the conductor strip enclosed within the contour, q is calculated from the discrete node values of ϕ as follows:

$$\varepsilon_{r1}\left(\frac{\phi_2 - \phi_1}{2h}\right)h + \left(\frac{\varepsilon_{r1} + \varepsilon_{r2}}{2}\right)\left(\frac{\phi_4 - \phi_3}{2h}\right)h + \varepsilon_{r2}\left(\frac{\phi_6 - \phi_5}{2h}\right)h + \ldots = q \tag{4.3.16}$$

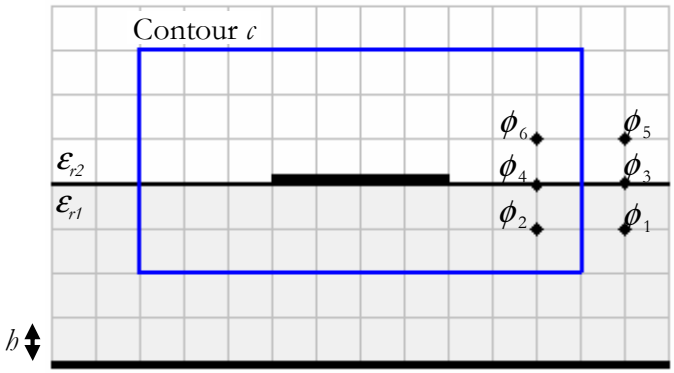

Figure 4.3.2: Illustration of contour c for calculation of capacitance [110].

The line capacitance with an applied voltage of V is given as:

$$C = \frac{q}{V} \tag{4.3.17}$$

It should be noted that the error bounds of the FDM calculations are dictated by both mesh and the finite number of iterations. The mesh error, which is a function of the mesh length *h*, occurs as the finite difference operator is used in place of the Laplacian, where high-order *h* terms are neglected. In addition to the mesh error, the FDM is subject to iteration error when the finite difference equations are not fully satisfied at every node. The amount the assumed value deviates from the computed value determined by the four surrounding nodes, is called the residual. Numerically, this is given by:

$$\delta_0 = \phi_0 - \frac{1}{4}(\phi_1 + \phi_2 + \phi_3 + \phi_4) \tag{4.3.18}$$

The iteration process terminates when all node residuals satisfy $|\delta_{\max}| < m$, where m is a positive constant. When decreasing the mesh size of the grid however, the maximum residual, m, must be decreased proportionately in order to satisfy the same iteration error bound although this will generally lead to a higher number of iteration cycles. It is not the intention of this work to address these errors in detail and more information can be found in [114, 115].

The computation of a large set of simultaneous linear equations iteratively are often time consuming and creates huge and sparse matrices with large number of unknowns to be solved. In the light of improving the convergence rate of the equations and also reducing the number of unknowns, several methods such as non-uniform grid, matrix eigenvalue problem and successive over-relaxation (SOR) can be employed [110, 113, 115-118]. These methods will be briefly mentioned as follow.

A non-uniform grid, previously shown in equation (4.2.4), can be applied to solution where region of interest or a particular direction within the structure requires different mesh size than others [110]. The size and density of matrices is of prime importance when solving a large set of simultaneous equations. Instead of direct storing all matrix elements which will thus lead to a large number of unknowns, the matrix elements of the huge and sparse matrices can be more

effectively stored and solved when transposed into eigenvalues and associated eigenvectors with appropriate matrix inversion. Further information regarding matrix eigenvalue problem and matrix inversion can be found in [116-118].

Successive over-relaxation (SOR) method, on the other hand, uses accelerating factor in order to improve the rate of convergence of the simultaneous equations and thereby decrease the number of iteration cycle. This relaxation method is illustrated by the following expression [113, 115]:

$$\phi_0 = \phi_0' - \alpha\delta_0 \tag{4.3.19}$$

ϕ_0 and ϕ_0' denote the potential value at a particular grid point from the current and previous iteration cycle respectively, α is the accelerating factor and δ_0 is the residual. The difference between any two successive ϕ_0 values corresponds to a correction term by a factor α to be applied in updating the current estimate. The accelerating factor is adjusted to an optimum value for which convergence is most rapid and α typically lies between 1 and 2 [118].

The following sections illustrate how the newly derived ferroelectric finite difference method was employed in solving problems for ferroelectric-based microstrip and several variants of coplanar waveguide transmission lines. The FDM calculations are validated by comparing the computed ε_{eff} and Z_c with existing closed-form analytical models discussed in the previous chapter in which the expressions were derived through conformal mapping techniques with the assumption of a quasi-static TEM mode of propagation along the line.

4.3.1 FDM on Microstrip

The variation of BST dielectric constant ε_{BST} as a function of applied electric field E at 300 K reported in [41] was employed in all the FDM calculations in this work. The BST dielectric constant curve adopted from [41] can be approximated using the following expression and is illustrated in Figure 4.3.3.

$$\varepsilon_{BST}(E) = 1010 \cdot \exp\left(\frac{-(E+0.6)^2}{7}\right) + 865 \tag{4.3.20}$$

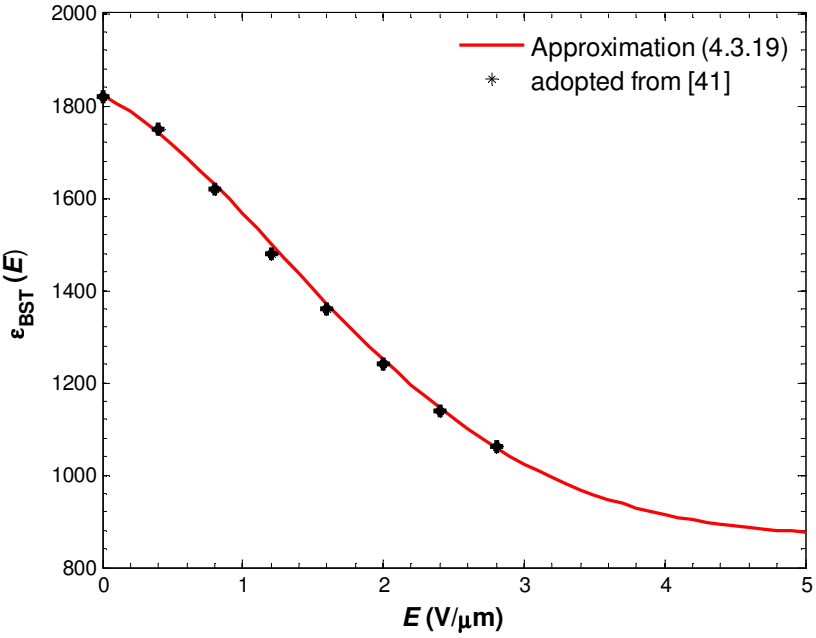

Figure 4.3.3: Approximated and experimental BST dielectric constant curve with respect to applied electric field adopted from [41].

Throughout the FDM calculations performed in this work, a metallisation of zero thickness and maximum residual value m of 10^{-6} were assumed. In addition, a fictitious boundary of unknown potential values with a distance much closer to the region of interest was implemented and the potentials within the boundary were obtained by solving half of the complete structure through consideration of its axis of symmetry as a magnetic wall. The potential distribution across the microstrip was computed by employing the appropriate ferroelectric finite difference equations detailed in the previous section, depending on the medium of the point of interest. Following determination of the potential distribution, the corresponding electric field E and dielectric constant ε distributions were evaluated.

Figure 4.3.4 (a and b) shows the distributions of electric field and dielectric constant across a 100 μm thick $Ba_{0.5}Sr_{0.5}TiO_3$ (BST) single layer ferroelectric microstrip under an applied voltage of 100 *V* and 200 *V,* respectively. Unequal mesh grid of size Δx = 5 μm and Δy = 1 μm were used in the figure. The microstrip signal strip w and ground plane w_G width was 100 μm and 1 mm respectively, with both BST and air height h_a equivalent to 100 μm. By solving half of the microstrip structure through its axis of symmetry, a total of 100 × 200 grids was created within the boundary. As observed from Figure 4.3.4(a), the uneven distribution of the electric field was due to the inhomogeneous dielectric-air media of the microstrip. This resulted in the variation of the ferroelectrics' dielectric constant as shown in Figure 4.3.4(b). The dielectric constant was found to be at its lowest value around the edges of the upper conducting strip, which corresponded to the electric field at its highest intensity. When a sufficiently large voltage was applied as in the case of 200 *V*, the variation of ε_{BST} was clearly observed to be increasingly significant.

Similarly, for a multilayer ferroelectric microstrip comprising a 5 μm thick BST ferroelectric layer on a 100 μm thick MgO substrate as shown in Figure 4.3.5, equivalent mesh grid sizes were specified i.e. Δx = 5 μm and Δy = 1 μm. In addition, identical dimensions of signal strip w, ground plane w_G width and air height h_a was applied, which generated a total of 100 × 205 grids. A visible variation in the BST layers' dielectric constant due to the changing electric field was observed in Figure 4.3.5(b). However, in contrast to the single ferroelectric layer configuration, the magnitude of the variation was substantially reduced, even with an applied voltage of 200 *V*. This was attributed to differential boundary conditions of electric flux density D and electric field E at the interface between the two materials. At the BST/MgO boundary, consider the components of D and E to be normal to the interface with the former being equivalent on either side of the boundary as shown below.

$$\begin{aligned} D_{BST} &= D_{MgO} \\ \varepsilon_{BST} E_{BST} &= \varepsilon_{MgO} E_{MgO} \end{aligned} \tag{4.3.21}$$

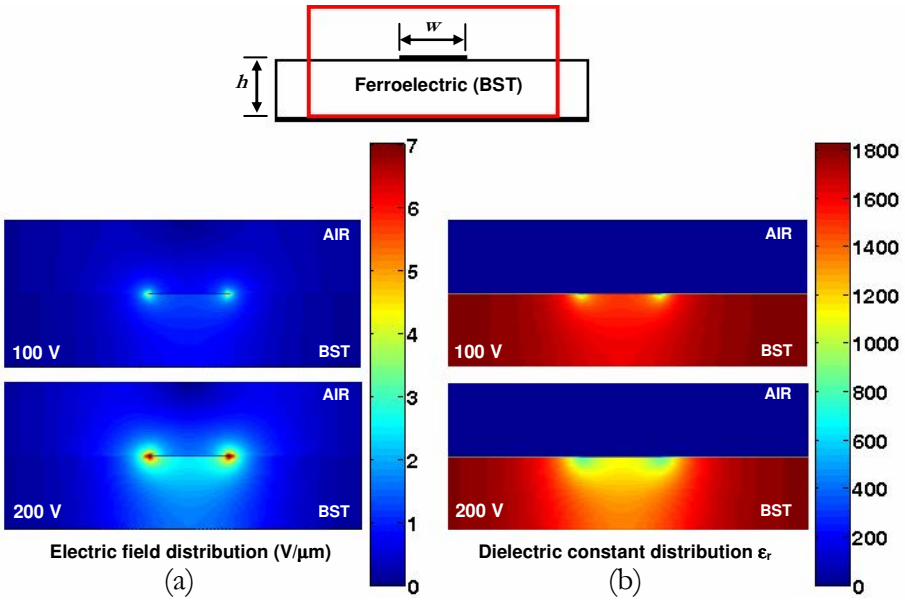

Figure 4.3.4: (a) Electric field and (b) dielectric constant distribution of a cross-sectional BST microstrip with $100V$ or $200V$ applied voltage. (w=100μm, h_1=100μm, w_G=1mm, h_a=100μm, Δx=5μm, Δy=1μm)

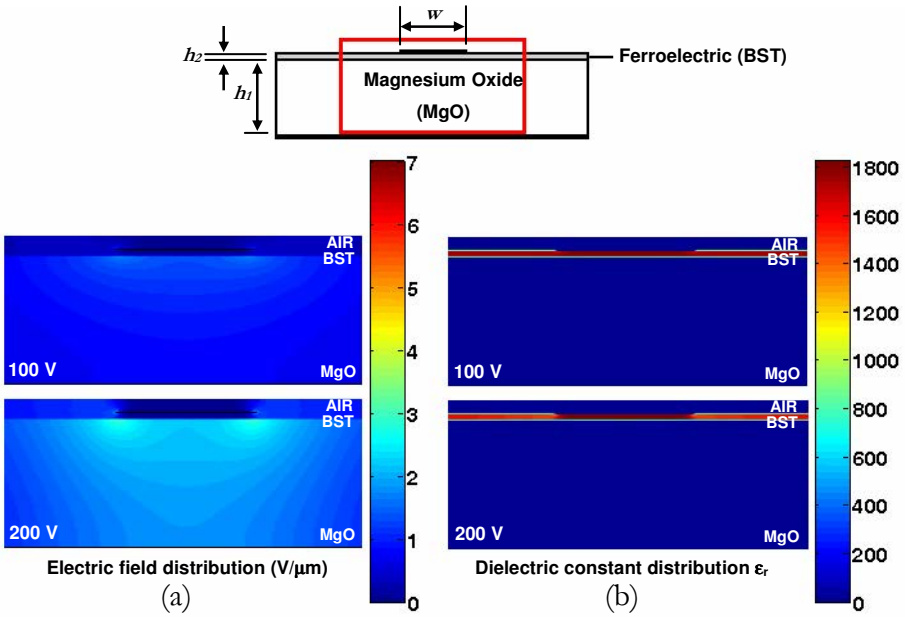

Figure 4.3.5: (a) Electric field and (b) dielectric constant distribution of a cross-sectional BST/MgO microstrip with $100V$ or $200V$ applied voltage. (w=100μm, h_1=100μm, h_2=5μm, w_G=1mm, h_a=100μm, Δx=5μm, Δy=1μm)

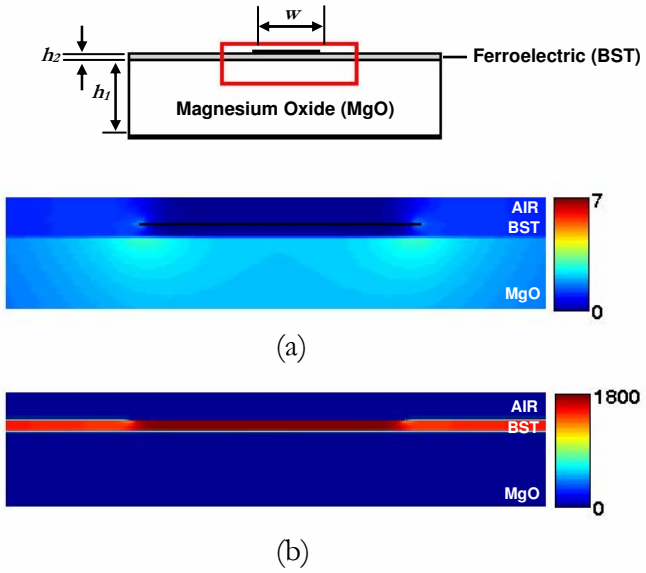

Figure 4.3.6: Enlarged view of the (a) electric field and (b) dielectric constant distribution of a BST/MgO microstrip around the centre conductor at 200V.

Due to the very high ε_{BST}, the electric fields were seen to be mostly concentrated within the MgO substrate region and as $|E_{BST}| << |E_{MgO}|$, relatively little variation in dielectric constant was experienced in the BST ferroelectric layer. Figure 4.3.6 illustrates the enlarged view of the E and ε_r distribution of BST/MgO microstrip around the centre conductor at applied voltage of 200 V.

As detailed above, the spatial variation of the dielectric constant within a ferroelectric layer can be obtained through finite difference calculations. In the majority of published work however, this variation in dielectric constant is usually ignored [2, 99, 108, 109]. Typically, a constant value is specified which is assumed to be the dielectric constant generated by an infinitely wide parallel plate under a constant applied voltage.

The computed characteristic impedance Z_c of a BST microstrip as a function of strip width-to-height w/h ratio is shown in Figure 4.3.7. Results were calculated using the newly derived ferroelectric finite difference equations with a varying $\varepsilon_{\mathrm{BST}}(E)$ and

were compared against that generated using a constant ε_{BST} value. The condition under which the latter was obtained was a voltage of 200 V applied across a microstrip of 100 μm thick BST ferroelectric substrate, which resulted in an electric field having a magnitude of 2 V/μm across the plates. By referring to Figure 4.3.3, the dielectric constant of BST generated was found to be approximately 1250. The existing closed-form analytical model given in equation (3.3.2) was also included in the graph for validation. In the FDM calculations shown below, equal mesh grid sizes, $\Delta x = \Delta y = h = 5$ μm were used for $w/h < 2$, and 20 μm for $w/h > 2$, with an air height h_a of 200 μm and microstrip ground plane w_G equivalent to 10 times the respective signal strip width w.

As observed from Figure 4.3.7, the computed impedance using the finite difference method where no spatial variation of the dielectric constant ($\varepsilon_{BST} = 1250$) was assumed showed extremely good agreement with the existing closed-form analytical model. When a varying dielectric constant was employed however, the calculated Z_c was lower at the corresponding strip width-to-height ratios. With narrow microstrip lines ($w/h < 1$), the disparity in the calculated impedance between constant and varying dielectric constant was approximately 11%. This difference was seen to decrease as the width-to-height ratios increased, with the Z_c value gradually converging as the w/h ratio approached ~ 4. Here, the behaviour of the microstrip line was analogous to parallel plates under the influence of a uniform electric field. For relatively wide microstrip lines ($w/h > 4$), the negligible difference in the calculated Z_c between constant and varying BST dielectric constants indicates that the current technique of assuming a fixed ferroelectric dielectric constant is valid. Nonetheless, the demonstrated methodology for determining accurate values of circuit impedance is a useful tool in enhancing the design and performance of ferroelectric-based devices, when the spatial variation of the ferroelectric dielectric constant as a function of the applied electric field is taken into consideration particularly for narrow lines. A recent paper relating to the technique outlined in this chapter has been published by the author [33] and can be found in Appendix C.

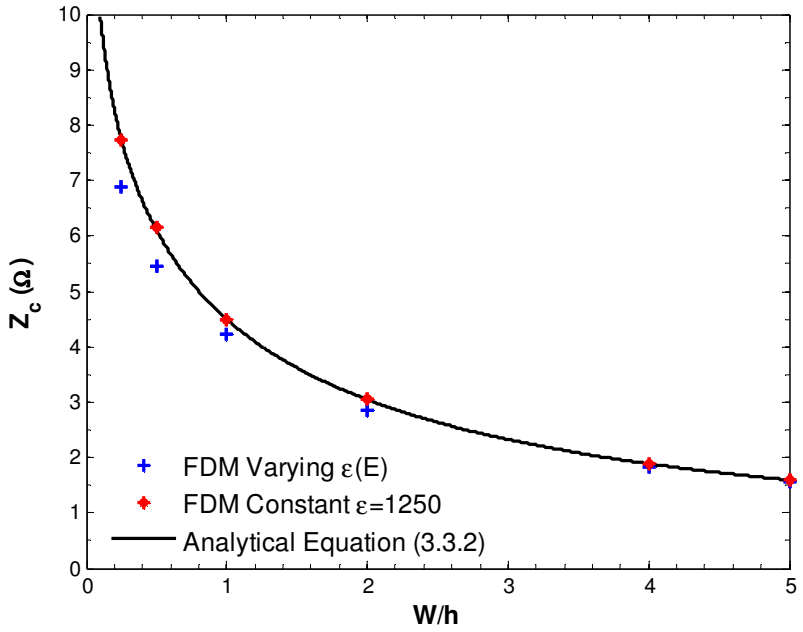

Figure 4.3.7: Computed characteristic impedance against w/h for microstrip on a layer of isotropic BST at 300 K (h=100μm, V=200V).

Key FDM calculated parameters for microstrip structures on single (Duroid) and multilayer (BST/MgO) substrates having dimensions similar to that utilised in the tunable attenuator to be described in Chapter 6 are listed in Table 4.3.1. The results from existing closed-form analytical models (equation (3.3.2) and (3.3.4)) and Sonnet simulations in the previous chapter are also included in the table for comparison. For the BST/MgO microstrip, the variation of BST dielectric constant under an uneven electric field were evaluated, with the results compared against data generated using a constant BST dielectric constant (ε_{BST} = 1250). In the Sonnet simulations, conductors were assumed to have zero thickness and infinite conductivity, with a simulation cell size of 2 μm.

As detailed in Table 4.3.1, the FDM calculations for both the single and multilayer configurations utilising a constant dielectric constant show good agreement with the analytical models and simulation results. However, when allowing for the spatial variation of the BST dielectric constant, the impedance of the

BST/MgO microstrip (w/h = 0.8) was found to be lower, with a difference of approximately 3%.

Configuration	w (μm)	Calculation method	ε_{eff}	Z_c (Ω)
Microstrip - Duroid (h=254μm, ε_r=10.2)	240	Analytical equation (3.3.2)	6.80	49.7
		Sonnet simulation	6.81	49.7
		† FDM	6.82	49.7
Microstrip - BST/MgO (h_1=500μm, ε_1=9.8, h_2=0.4μm, ε_2=1250)	400	Conformal mapping (3.3.4)	6.97	52.4
		Sonnet simulation	7.33	51.5
		†† FDM : ε_{BST} = 1250	7.21	51.5
		†† FDM : ε_{BST} (E)	7.66	49.9

Table 4.3.1: Comparison of calculated parameters obtained from existing closed-form models, sonnet simulations and finite difference method.

† Δx=40μm, Δy=2μm, w_G=1200μm and h_a=50μm

†† Δx=50μm, Δy=0.2μm, w_G=2000μm and h_a=30μm

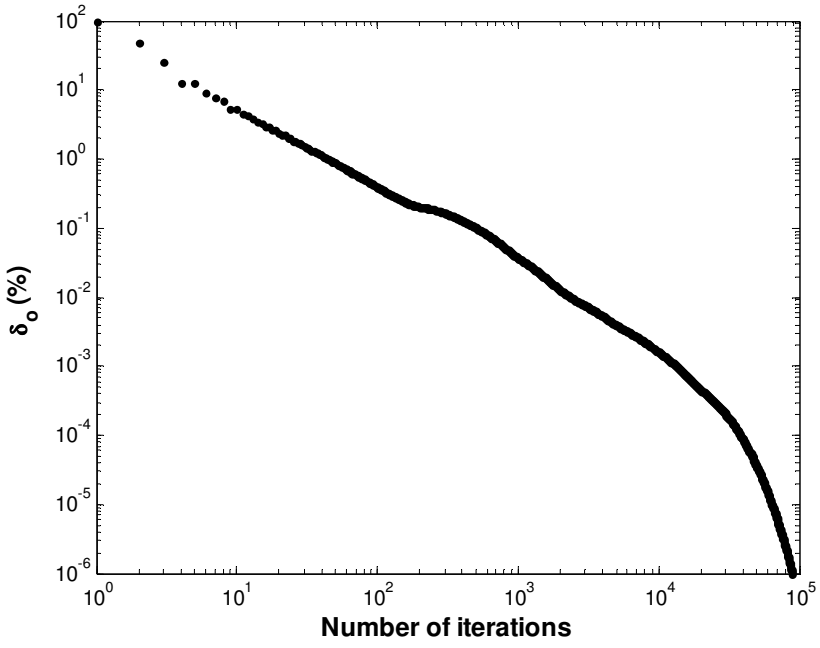

Figure 4.3.8: Convergence of residuals in the mesh grids for Duroid microstrip.

To test for convergence of the computed potentials in a cross sectional area, Figure 4.3.8 depicts the residual value in the mesh grids against the number of iterations for the case of the aforementioned Duroid microstrip configurations. As observed from the figure, the residual δ_0 (in percentage) decreases with increasing number of iterations. This indicates that the value of potential at the nodes converges to a solution when all node residuals have satisfied the defined criterion $|\delta_{max}| < m$, i.e. termination of iteration process.

4.3.2 FDM on CPW and CBCPW

Following successful application on microstrip, the finite difference method (FDM) was subsequently employed on several variants of coplanar waveguide geometry and were verified / compared with existing closed-form analytical models given in the previous chapter. This was done in order to predict the performance of the proposed ferroelectric phase shifter and tunable attenuator design in Chapter 5 and 6.

Figure 4.3.9 to Figure 4.3.12 illustrates the E and ε distribution of a coplanar waveguide (CPW) and conductor-backed coplanar waveguide (CBCPW) on single layer (100 μm thick BST) and multilayer (5 μm thick BST on 100 μm thick MgO substrate of dielectric constant 9.8) configurations, respectively. A voltage of 50 V, 100 V and 200 V was applied across the conductor plates. Unequal mesh grid of size Δx = 2 μm and Δy = 1 μm were used in all the figures. The signal strip w, gap g and in-plane ground w_g width was 100 μm, 20 μm and 80 μm respectively, with air height equivalent to 20 μm. By solving half the structure through its axis of symmetry, a total of 75 × 120 and 75 × 125 grids were created within the boundary for BST and BST/MgO configurations, respectively. As observed from all the figures, the variations of the BST dielectric constant under the influence of the uneven electric field are clearly visible, particularly at 200 V. Similar to the microstrip layout, the dielectric constant was lowest where the electric field was most intense, i.e. around

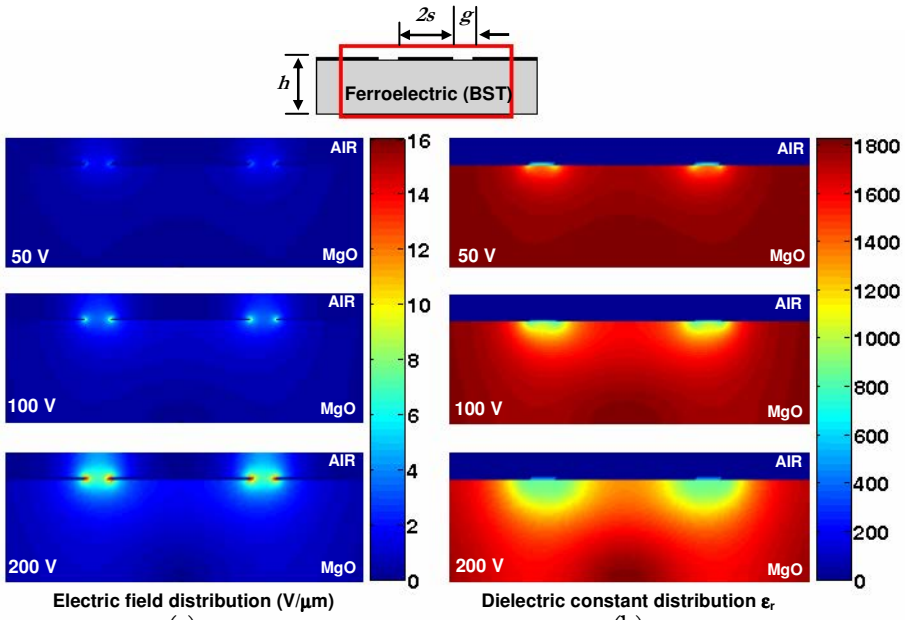

Figure 4.3.9: (a) Electric field and (b) dielectric constant distribution of a cross-sectional BST CPW with various applied voltage.
($2s$=100μm, g=20μm, w_G=80μm h=100μm, h_a=20μm, Δx=2μm, Δy=1μm)

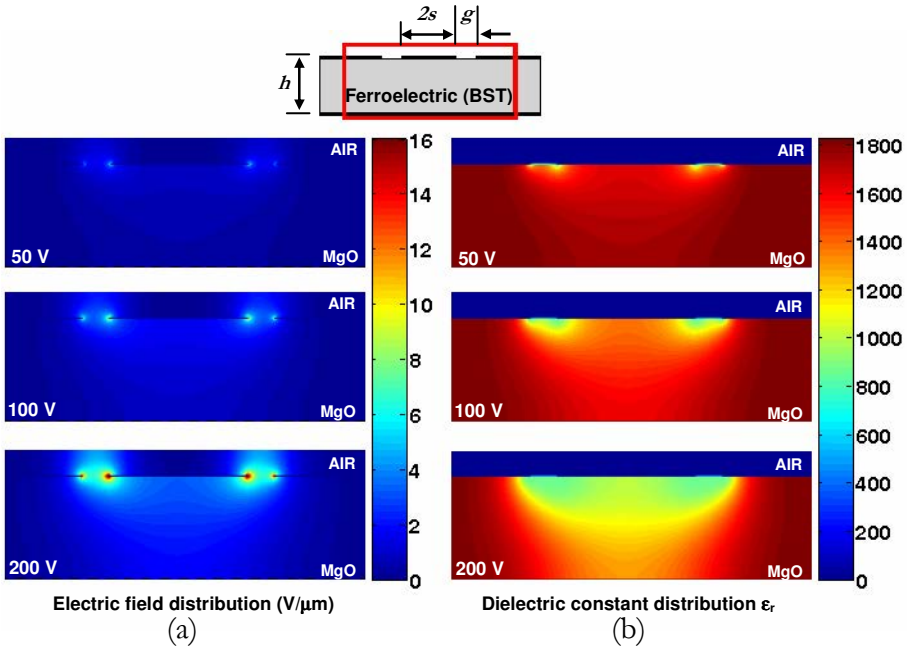

Figure 4.3.10: (a) Electric field and (b) dielectric constant distribution of a cross-sectional BST CBCPW with various applied voltage.
($2s$=100μm, g=20μm, w_G=80μm h=100μm, h_a=20μm, Δx=2μm, Δy=1μm)

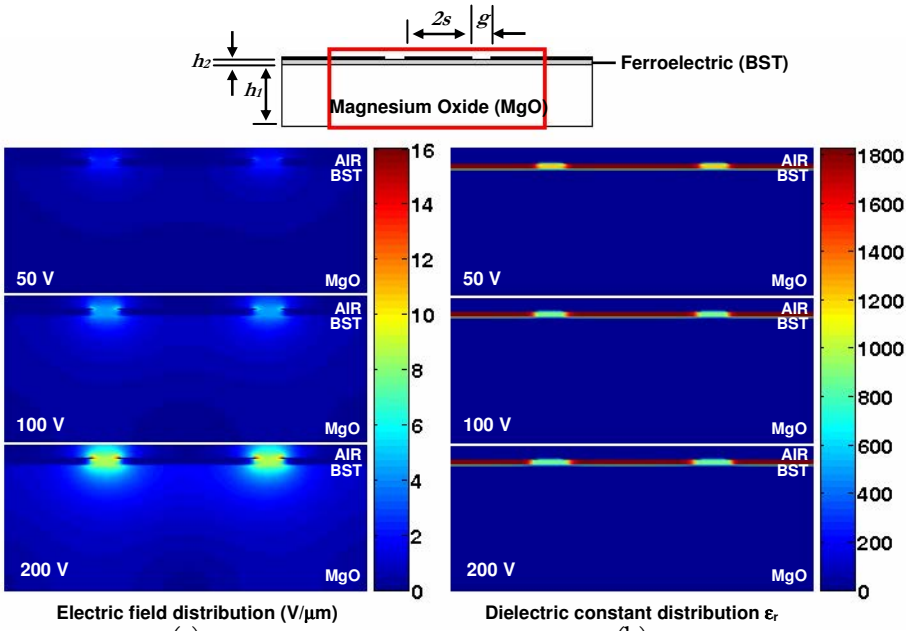

Figure 4.3.11: Enlarged view of (a) electric field and (b) dielectric constant distribution of a cross-sectional BST/MgO CPW around the centre conductor with various applied voltages.
($2s$=100μm, g=20μm, w_G=80μm h_1=100μm, h_2=5μm, h_a=20μm, Δx=2μm, Δy=1μm)

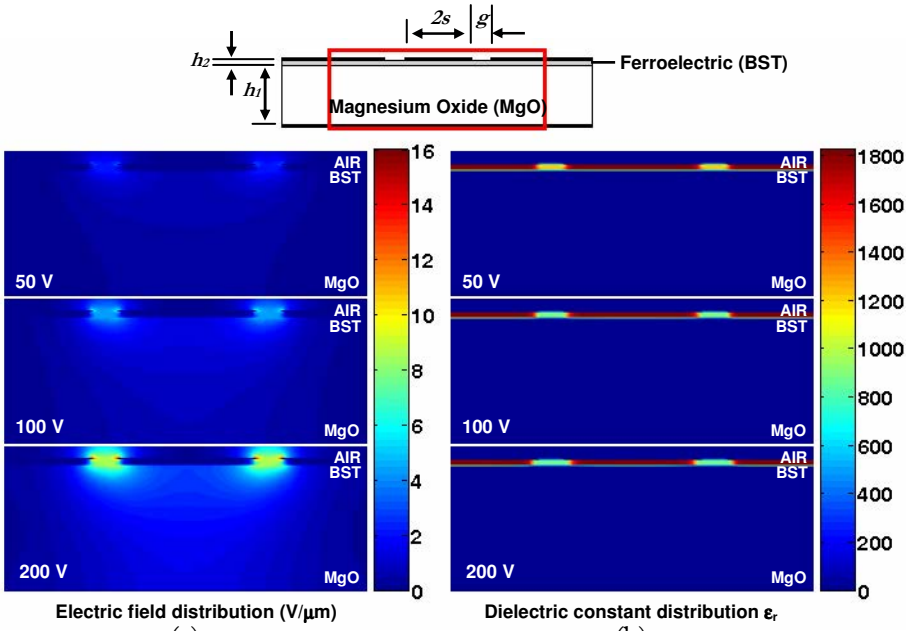

Figure 4.3.12: Enlarged view of (a) electric field and (b) dielectric constant distribution of a cross-sectional BST/MgO CBCPW around the centre conductor with various applied voltages.
($2s$=100μm, g=20μm, w_G=80μm h_1=100μm, h_2=5μm, h_a=20μm, Δx=2μm, Δy=1μm)

the edges of the conductors.

Table 4.4.1 shows the computed ε_{eff} and Z_c values for CPW and CBCPW structures utilising single (Duroid) and/or multilayer (BST/MgO) substrates using the FDM, conformal mapping and Sonnet simulation techniques respectively. The configurations reflect actual parameters used for the phase shifter and tunable attenuator described in Chapters 5 and 6. As with the microstrip geometry, the varying dielectric constant within the BST of the multilayer substrate was considered and compared against data generated using a fixed BST dielectric constant of 1250 or 1400.

As detailed in Table 4.4.1, the FDM calculations for both the single and multilayer configurations utilising a fixed dielectric constant show good agreement with the analytical models and simulation results. However, when allowing for the spatial variation of the BST dielectric constant, the impedance on multilayer substrate (BST/MgO) was found to be marginally lower, with a difference of approximately 4 to 6% for CPW line of dimension $2s$ = 50 μm and g = 78 μm and approximately 1.4 to 2.4% for CBCPW line of dimension $2s$ = 20 μm and g = 40 μm.

4.4 Conclusions

A modified FDM for determining the ε_{eff} and Z_c of ferroelectric-based transmission lines where the spatial variation of dielectric constant is taken fully into consideration has been presented. The results have been verified and compared with existing closed-form analytical models from the previous chapter as well as other published work. Extremely good agreement between FDM calculation and analytical models was observed. Although similar work has been reported by Sung *et al.* [119] in which the finite element method (FEM) was employed in solving static Poisson's equation iteratively to evaluate the ε_{eff} and Z_c of a similar structure (microstrip line on ferroelectric substrate), the simplicity of FDM nonetheless, remains its primary advantage. The results in [119] with varying ferroelectric dielectric constant showed

Configuration	2s (μm)	g (μm)	Calculation method	ε_{eff}	Z_c (Ω)
CBCPW – Duroid (h=254μm, ε_r=10.2)	120	60	Conformal mapping (3.4.6) Sonnet simulation † FDM	5.77 5.86 5.77	48.4 48.5 48.4
CBCPW - BST/MgO (h_1=500μm, ε_1=9.8, h_2=0.35μm, ε_2=1250 or 1400)	20	40	Conformal mapping (3.4.8) Sonnet simulation †† FDM: ε_{BST} = 1250 †† FDM: $\varepsilon_{BST}(E)$	15.71 16.14 15.70 16.52	45.1 45.0 45.1 44.0
			Conformal mapping (3.4.8) Sonnet simulation †† FDM: ε_{BST} = 1400 †† FDM: $\varepsilon_{BST}(E)$	16.98 17.37 17.03 17.50	43.4 43.3 43.3 42.7
CPW - BST/MgO (h_1=500μm, ε_1=9.8, h_2=0.35μm, ε_2=1250 or 1400)	50	78	Conformal mapping (3.4.2) Sonnet simulation ††† FDM: ε_{BST} = 1250 ††† FDM: $\varepsilon_{BST}(E)$	10.31 10.93 10.34 11.21	52.1 52.0 52.0 50.1
			Conformal mapping (3.4.2) Sonnet simulation ††† FDM: ε_{BST} = 1400 ††† FDM: $\varepsilon_{BST}(E)$	10.91 11.55 10.93 11.86	50.6 50.6 50.6 48.6

Table 4.4.1: Comparison of calculated parameters obtained from conformal mapping technique, sonnet simulations and finite difference method (FDM).

† Δx=10μm, Δy=2μm, w_G=60μm and h_a=200μm
†† Δx=2μm, Δy=0.05μm, w_G=20μm and h_a=3.6μm
††† Δx=2μm, Δy=0.05μm, w_G=20μm and h_a=34μm

the same trend as the FDM calculation discussed here, where Z_c is generally lower with higher ε_{eff} as compared to that of the assumed approximate constant value. This therefore, validates the work presented here and that recently published in [33].

Experimental validation of the new finite difference equation has not been performed as it is thought unlikely that currently available measurement

instrumentation possess the necessary resolution to discriminate between the small differences shown in Figure 4.3.7, Table 4.3.1 and Table 4.4.1. The small difference in the results indicates that the closed-form conformal mapping technique of assuming a fixed ferroelectric dielectric constant is valid for most practical cases. The methodology for determining accurate values of circuit impedance has been demonstrated and is a useful tool in enhancing the design and performance of ferroelectric based devices.

In the next chapter, the design and characterisation of tunable CPW phase-shifters using BST ferroelectric thin-films deposited on an MgO substrate will be presented. Comparisons between experimental and simulation results will be detailed.

Chapter 5

Ferroelectric Phase Shifter

5.1 Introduction

A phase shifter is essentially a device that produces a shift in phase angle of a microwave signal without changing its magnitude. Phase shifters are crucial elements in phased array antennas with steerable electronic beams, which allow the antenna beams to be focussed in the desired direction without physical repositioning of the antenna [8-11]. Such antennas are typically served by thousands of simultaneously operating phase shifters and therefore, phase shifters play a key role in determining the performance and the cost of the antenna. Electrically scanned phased array antennas have shown broad utilisation for both commercial and military applications, including advanced military radars, cellular base stations, satellite communications, and automotive anti-collision radar.

Traditionally, phase shifters in phased array antennas are constructed using ferrites where strong magnetic fields are required for tuning [11, 25]. Implementing ferrite phase shifters in phased arrays for commercial applications however, incur

drawbacks in terms of cost, size and weight. In addition, ferrite-based devices are slow in responding to control signals, which thus restrict their use in applications where rapid scanning is required [11].

Semiconductor switching elements such as field-effect transistors (FET), positive intrinsic negative (PIN) diodes and varactor diodes offer alternative solutions in construction of a phase shifter [15, 16, 24]. Unfortunately, inherent shortcomings involving high power consumption, cost and size of PIN diodes together with the relatively high loss of Galium Arsenide (GaAs) transistors and Silicon (Si) varactors at microwave frequencies have restricted the widespread application of such technology. In recent years, advances in the field of micro-electro-mechanical systems (MEMS) technology appeared to offer considerable advantages over competing technologies in terms of performance, power handling and power consumption. However, problems involving low reliability associated with component mechanical movement coupled with the high switching time and cost of packaging has prevented any extensive use of MEMS phase shifters [23, 24].

Ferroelectric materials have received tremendous interest over the last decade due to their potential in overcoming the limitations of ferrite, semiconductor and MEMS type equivalents. Although ferroelectric materials commonly suffer from a strong temperature dependency relating to dielectric constant and noticeable microwave loss, their superior properties in terms of tuning speed, power consumption and power handling capability as well as the advantage of low cost and reduced size, have made ferroelectric materials extremely competitive and particularly favoured for devices such as phased array antennas and other frequency-agile components [2, 15, 24, 28].

Ferroelectric phase shifters are by far the most extensively studied ferroelectric frequency-agile components and have been reported in numerous publications [1, 8-10, 38-40, 67, 68, 120]. Several ferroelectric phase shifters of delay-line type will be detailed in this chapter, where a variation in the ferroelectric materials' dielectric constant due to an applied electric field results in the change of the propagation constant in coplanar line, thus producing the phase shift. Sections 5.2 and 5.3

describe the ferroelectric phase shifter in both coplanar waveguide (CPW) and conductor-backed coplanar waveguide (CBCPW) forms respectively. Analytical models from Chapter 3 are employed for ferroelectric material characterisation as well as predicting the performance of the ferroelectric phase shifters. These ferroelectric phase shifters are key components in the tunable attenuator device described in Chapter 6.

5.2 CPW Ferroelectric Phase Shifter

Two designs of a coplanar waveguide (CPW) form phase shifter of delay-line type are presented in this section. The first is a simple CPW transmission line, whilst the other is a CPW structure in tapered form; hereinafter referred to as the 'tapered CPW', and are shown in Figure 5.2.1 and Figure 5.2.2, respectively. Both designs are based on multilayer configurations comprising $Ba_{0.5}Sr_{0.5}TiO_3$ (BST) ferroelectric thin-films on an MgO substrate.

The BST thin-films were deposited to a thickness of ~0.35 μm onto the MgO substrate of dimension 10 × 10 × 0.5 mm by pulsed laser deposition (PLD) technique. A laser fluence of 1.5 Jcm^{-2} at 5 Hz pulse rate with oxygen pressure at 10^{-1} mbar was used. The substrate temperature during deposition was 750°C. *Ex situ* post-deposition annealing was carried out in a flowing oxygen furnace for 24 hours at 1150°C. Silver coplanar transmission lines of 300 nm thick were patterned onto the ferroelectric films by lift-off photolithography.

The characteristics of the CPW line were calculated using the conformal mapping equations developed by Gevorgian *et al.* [84], as previously shown in section 3.4.1. The design parameters of the CPW line (i.e. width of centre strip w, gap g, length of the line) were chosen to achieve an optimal trade-off between the line impedance, phase shift and insertion loss, at a given thickness and dielectric constant of the BST thin-film ($\varepsilon_{BST}(0\ V)$= 1800) and MgO substrate (ε_r = 9.8). In other words, the coplanar lines were designed to approach a 50 Ω impedance line whilst ensuring

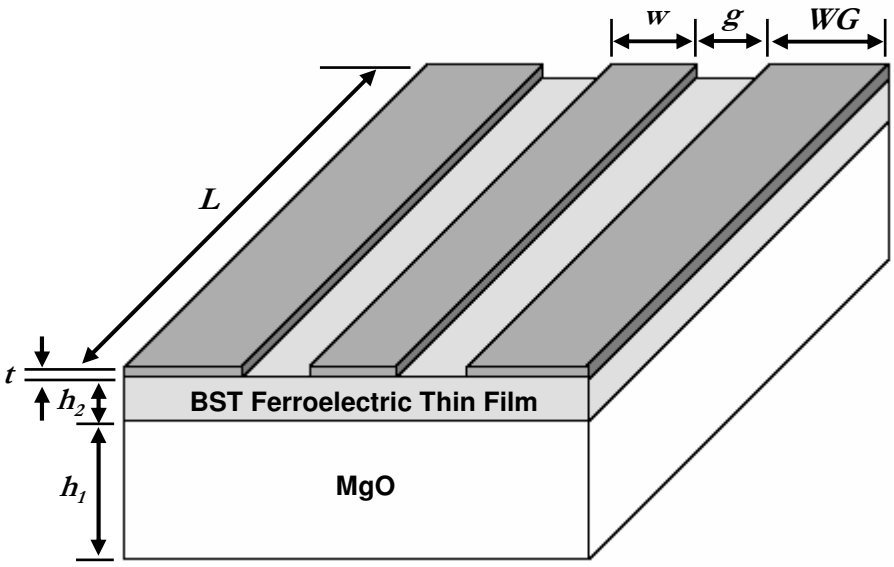

Figure 5.2.1: CPW phase shifter based on BST thin-film and MgO substrate.

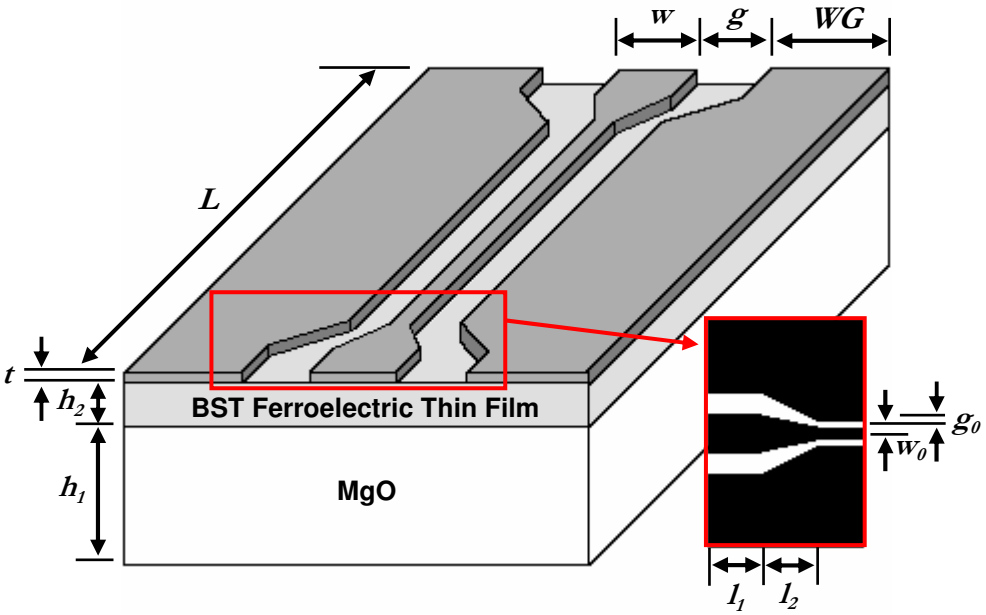

Figure 5.2.2: Tapered CPW phase shifter with narrower strip and gap width, based on BST thin-film and MgO substrate.

a reasonable width of gap in order to obtain a relatively high electric field in the vicinity of the centre strip. In addition, the strip-to-gap ratio (w/g) of the intermediate transition section in the tapered CPW phase shifter was ensured to retain a constant 50 Ω impedance line along the taper for minimal reflections. Table 5.2.1 lists the design parameters for both phase shifters.

	CPW phase shifter	**Tapered CPW phase shifter**
w	25 μm	50 μm
g	54 μm	78 μm
w_0	-	10 μm
g_0	-	32 μm
WG	275 μm	275 μm
l_1	-	50 μm
l_2	-	50 μm
L	5250 μm	5250 μm

Table 5.2.1: Design parameters of CPW and tapered CPW phase shifters on BST thin-film and MgO substrate.

5.2.1 Microwave Measurement

Microwave on-wafer frequency measurements were performed at room temperature using a Cascade Microtech Summit 9000 analytical probe station with 250 μm pitch ground-signal-ground (GSG) probes connected to a vector network analyser (Agilent E8361A) at frequencies ranging from 0.5 to 20 GHz. A bias-tee was used to apply bias voltages of up to 100 V between the ground and signal lines, producing average electric fields up to 1.85 V/μm and 3.13 V/μm for the CPW and tapered CPW phase shifter respectively. Prior to measurement, calibration of the probe tips was carried out with the LRRM (load-reflect-reflect-match) method using impedance standards formed from gold CPW lines on an alumina substrate. The

LRRM calibration technique required four standard measurements, of which only the 50 Ω matched load and thru (delay) had to be known precisely. The reflection measurements were made with the probes lifted off the substrate as well as with the probes placed on a shorted line. The calibration procedure removed systematic error sources that could affect the response of the test devices, and set the measurement reference planes at the probes tips [121, 122].

The scattering-parameters data obtained from microwave measurements at different bias voltages for the CPW and tapered CPW phase shifters are shown in Figure 5.2.3 and Figure 5.2.4 respectively. The maximum insertion loss of the CPW phase shifter was measured to be less than 5.4 dB, with the return loss better than 20 dB for all states of bias voltages at frequencies up to 20 GHz. Under the same conditions, the insertion loss of the tapered CPW phase shifter was measured to be less than 10.6 dB, with the return loss not exceeding 13 dB. As seen from both figures, maximum insertion losses were observed at 0 V and improved with increasing bias voltage. In addition, the phase of the phase shifters (φ_{S21}), as depicted in Figure 5.2.3(b) and Figure 5.2.4(b), was found to increase in a linear fashion with frequency and bias voltage. The improved response with bias voltage was found to be consistent with other work reported in the literature [41, 67, 68, 123].

The phase change or the differential phase shift ($\Delta\Phi$) of the phase shifter is:

$$\Delta\Phi = \varphi_{S21}(E) - \varphi_{S21}(0) \tag{5.2.1}$$

where $\varphi_{S21}(0)$ and $\varphi_{S21}(E)$ denote the phase at zero and non-zero electric field respectively. The performance of phase shifters are not solely determined by the differential phase shift, but also quantified by the associated insertion loss. This is commonly described as figure-of-merit (*FoM*), expressed as [66]:

$$FoM = \frac{\Delta\Phi}{\sqrt{S_{21}(0) \cdot S_{21}(E)}} \left(^{\circ}/\mathrm{dB}\right) \tag{5.2.2}$$

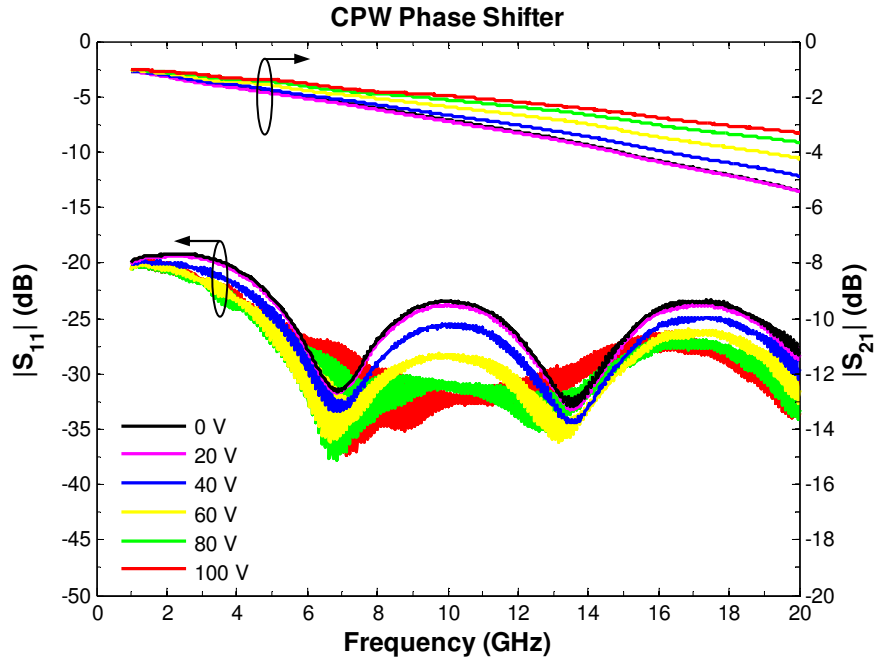

(a)

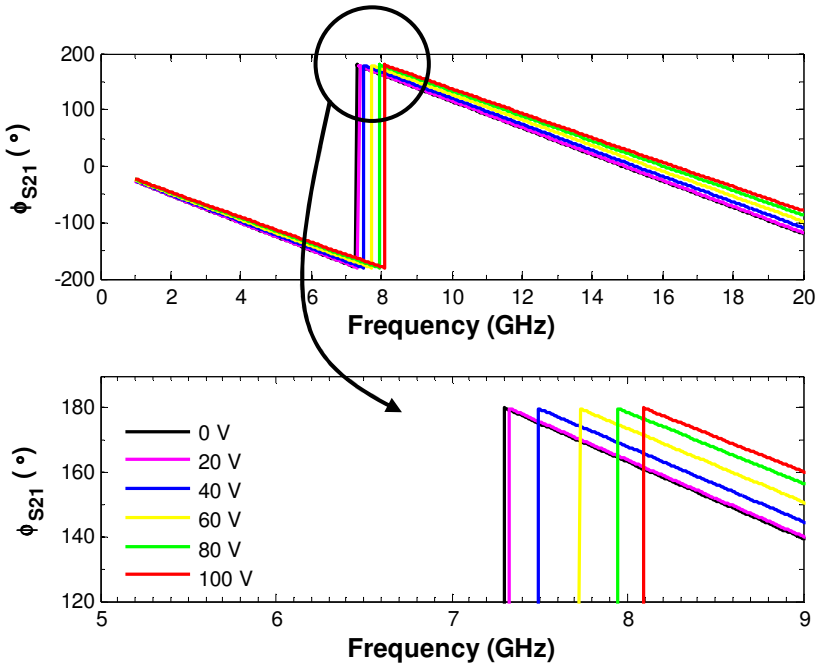

(b)

Figure 5.2.3: Measured (a) scattering-parameters, and (b) phase of CPW phase shifter with various bias voltages.

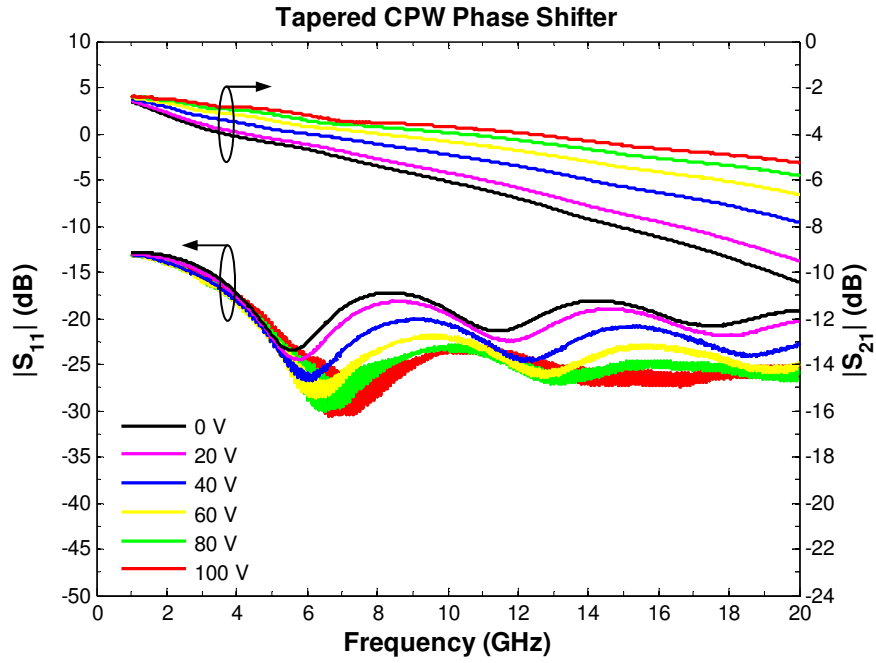

(a)

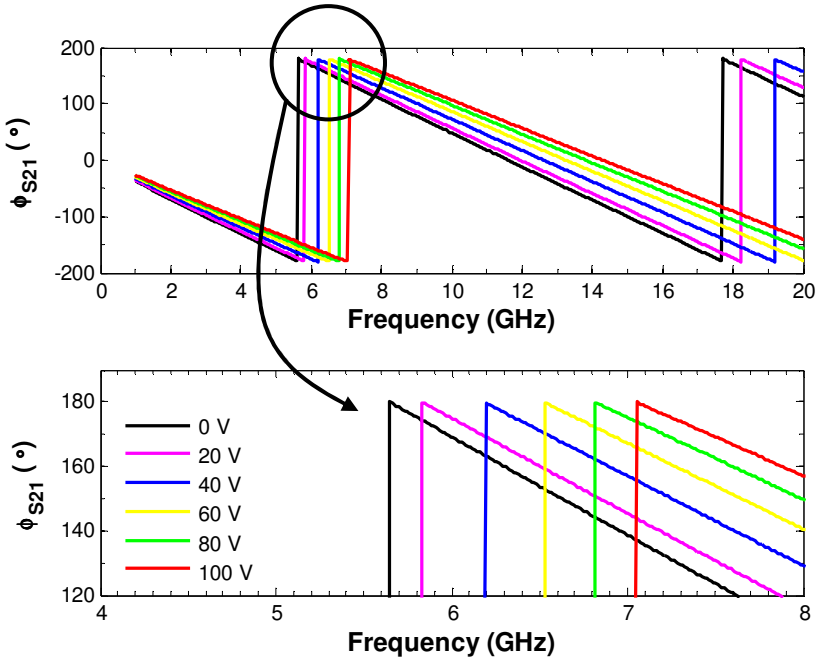

(b)

Figure 5.2.4: Measured (a) scattering-parameters, and (b) phase of tapered CPW phase shifter with various bias voltages.

In equation (5.2.2), $S_{21}(0)$ and $S_{21}(E)$ represent the insertion losses in both states (i.e. zero and non- zero electric field).

The measured differential phase shift as a function of bias voltages at various frequencies is plotted in Figure 5.2.5. A continuous phase shift of 40° and 105° was obtained at 20 GHz with bias voltage of 100 *V*, which equates to an electric field of 1.85 *V*/μm and 3.13 *V*/μm for both the CPW and tapered CPW phase shifter respectively. A larger phase shift was achieved for the latter configuration due to its narrower gap width, i.e. with the same bias voltage higher electric field strength was created in the vicinity of the signal strip for the tapered CPW phase shifter, which resulted in a greater change of dielectric constant within the BST layer. This therefore further increased the electric length alteration of the transmission line and thus generated a larger differential phase shift, as observed.

Figure 5.2.6 depicts the variation of the differential phase shift as a function of frequency with different bias voltages for both the CPW and tapered CPW phase shifters, with their corresponding figure-of-merit detailed in Figure 5.2.7. As anticipated, the differential phase shift increased with frequency and bias voltage. Under a bias voltage of 100 *V*, the *FoM* of CPW and tapered CPW phase shifter was found to be 8°/dB and 10°/dB at 6 GHz and 9.5°/dB and 14.4°/dB at 20 GHz respectively.

5.2.2 Microwave Characterisation

The scattering-parameters obtained from experimental measurement can be utilised to extract various microwave parameters, namely, the complex propagation constant γ, effective dielectric constant (ε_{eff}), characteristic impedance (Z_o) and loss tangent related to the device and the materials used. The complex propagation constant ($\gamma = \alpha + j\beta$) is related to the measured transmission coefficient (S_{21}) and the phase of transmission coefficient (φ_{S21}) by the following equations [124, 125]:

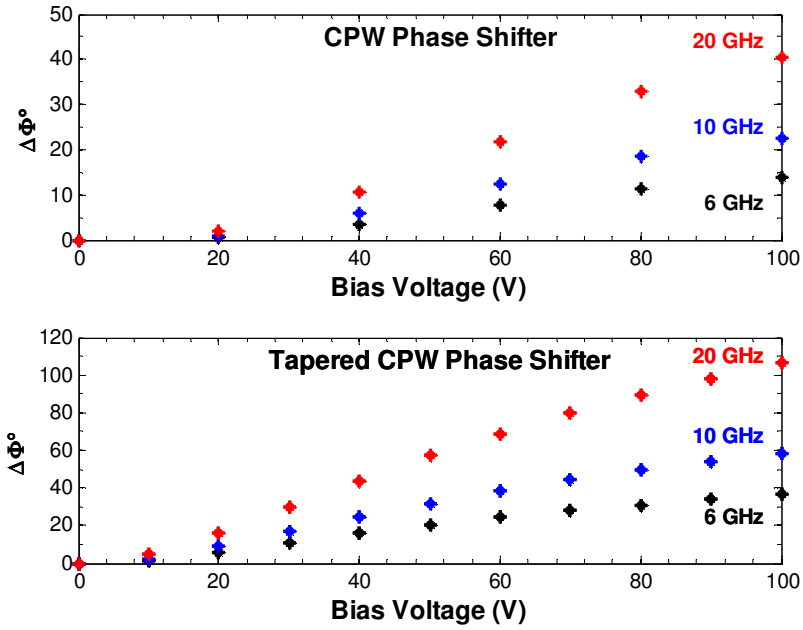

Figure 5.2.5: Differential phase shift as a function of bias voltage for CPW and tapered CPW phase shifter.

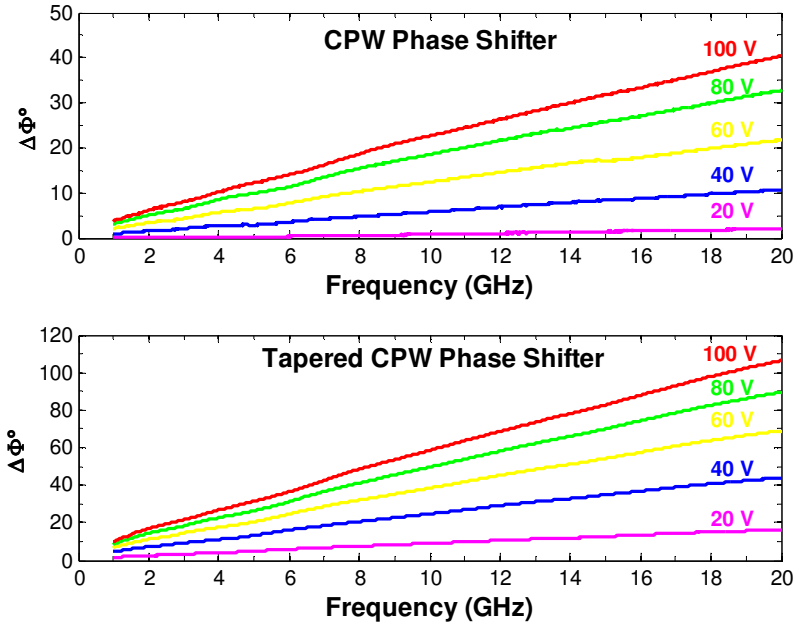

Figure 5.2.6: Differential phase shift as a function of frequency for CPW and tapered CPW phase shifter.

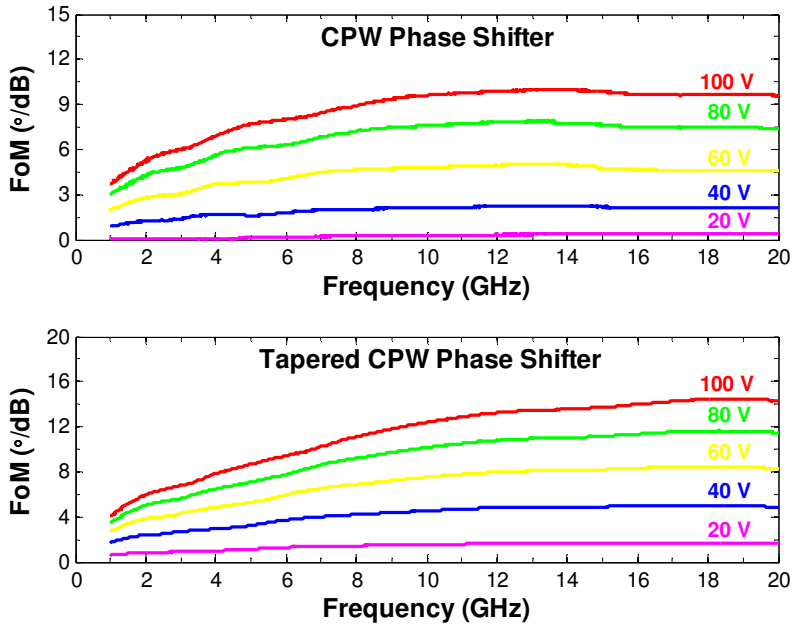

Figure 5.2.7: Figure-of-merit of CPW phase shifter (dotted line) and tapered CPW phase shifter (solid line) with different bias voltages.

$$\alpha = -\frac{S_{21}(\text{dB})}{l\,(\text{m})} \qquad \beta = -\frac{\varphi_{S21}(\text{rad})}{l\,(\text{m})} \tag{5.2.3}$$

where α is the attenuation constant (dB/m) and β is the phase constant (rad/m). The effective dielectric constant of the phase shifter was calculated using equation (5.2.4) [41, 126].

$$\varepsilon_{eff} = -\left(\frac{c_0 \gamma}{2\pi f}\right)^2 \tag{5.2.4}$$

Alternatively, ε_{eff} can also be determined from the slope of φ_{S21} versus frequency from the relationship $\varphi_{S21} = 2\pi f \cdot l \cdot \sqrt{\varepsilon_{eff}} / c_0$ [124, 125]. From the derived effective dielectric constant (ε_{eff}), the real part of the dielectric constant of the BST thin-film

(ε_{r2}') was then extracted using the conformal mapping technique based on the quasi-TEM approach expressed in equation (3.4.1), rearranged to give:

$$\varepsilon_{r2}' = \frac{1}{q_2}\left[\varepsilon_{eff}' - 1 - (q_1\varepsilon_{r1}) + q_1 + (q_2\varepsilon_{r1})\right] \tag{5.2.5}$$

In equation (5.2.5), ε_{r1} is the dielectric constant of the MgO substrate (assumed to be purely real with value of 9.8, which is appropriate for a very low loss substrate such as MgO ~10^{-4} [99]), ε_{eff}' is the real part of the effective dielectric constant and $q_{1,2}$ are the filling factors involving the transmission line dimensions, film and substrate thickness given in equation (3.4.3). The characteristic impedance of the CPW line (Z_o) and the relative tunability (n_r) of the BST thin-film were calculated from equation (3.4.2) and (2.2.2) respectively.

Figure 5.2.8 shows the real part of the BST thin-film dielectric constant and relative tunability of the BST thin-film as a function of applied electric field. The data was obtained from the measured scattering-parameters of CPW and tapered CPW phase shifter at 20 GHz using conformal mapping technique. ε_{BST}' was found to be ~1800 at 0 $V/\mu m$ and ~940 at 3.13 $V/\mu m$. This corresponds to an n_r of approximately 48%. As predicted, with similar sample preparation routes, the ε_{BST}' characterised in the current work shows close agreement with the data curve reported in [41] and the approximated BST curve employed in all the finite difference method (FDM) calculations in the previous chapter as shown in equation (4.3.20).

The characteristic impedance of the coplanar line with respect to bias voltage is plotted in Figure 5.2.9 with values of 45-52 Ω and 40-51 Ω obtained for CPW and tapered CPW phase shifters respectively. It was observed that as bias voltage increased, the impedance gradually approached 50 Ω, where reflection in the line was expected to be minimal. This accounted for the improved insertion and return losses of the phase shifters (as shown in Figure 5.2.3 and Figure 5.2.4) at 100 V bias as compared to zero bias voltage.

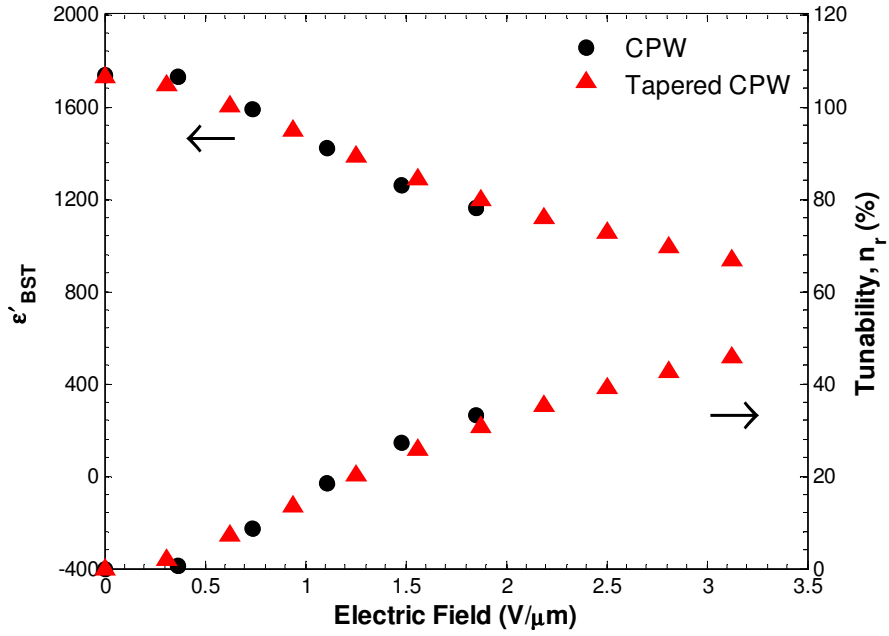

Figure 5.2.8: Real part of the dielectric constant of BST thin-film and relative tunability of the BST thin-film as a function of applied electric field. ③ and ⑩ represent the data extracted from CPW and tapered CPW phase shifter, respectively.

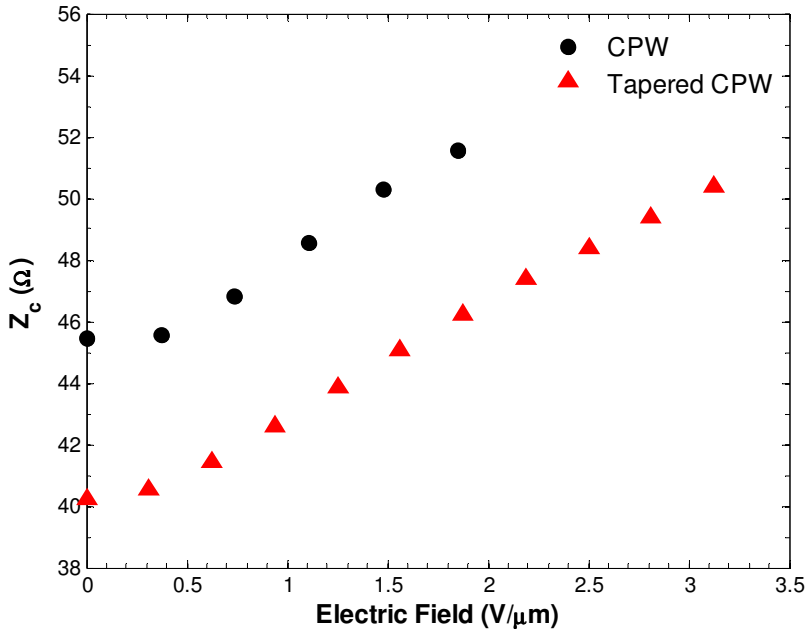

Figure 5.2.9: Characteristic impedance as a function of bias voltage for CPW and tapered CPW phase shifter.

The total loss representation of the phase shifter, which involves both dielectric and conductor losses, is termed as the 'effective loss tangent' (tan δ_{eff}) and can be calculated by the following expression [41]:

$$\tan \delta_{eff} = \frac{\varepsilon''_{eff}}{\varepsilon'_{eff}} \tag{5.2.6}$$

where ε'_{eff} and ε''_{eff} are real and imaginary parts of the effective dielectric constant respectively.

Figure 5.2.10 shows the effective loss tangent of the phase shifters measured at different bias voltages. An apparent relaxation in effective loss tangent at frequencies below 2 GHz was observed for both designs. Such behaviour was believed to have been caused by calibration errors near zero frequency and was found to agree with similar work reported in [124, 125] and [126]. Conversely at the higher frequency regime, the effective loss tangent was found to be more stable and reliable.

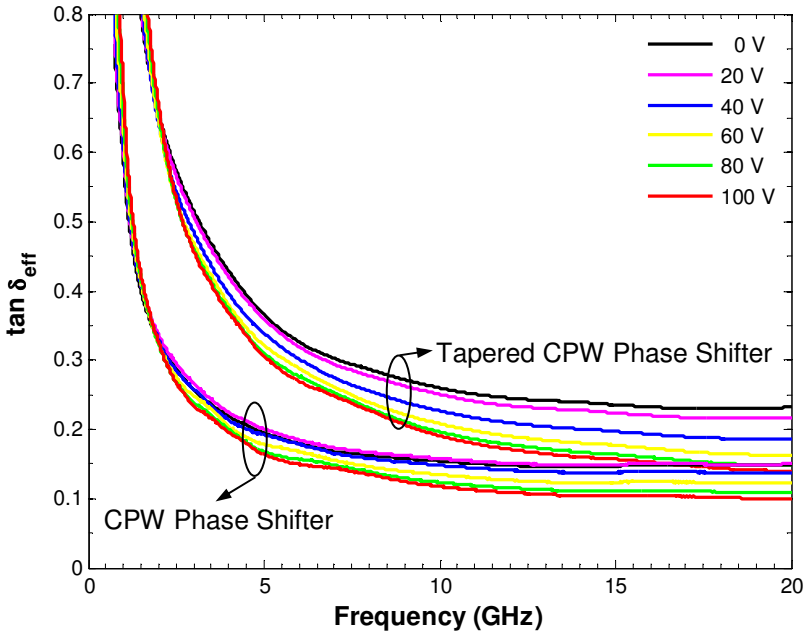

Figure 5.2.10: Effective loss tangent tan δ_{eff} as a function of frequency.

As previously addressed in Section 3.6, the total losses in a coplanar line are inversely proportional to the strip width *2s*, a fact clearly illustrated in Figure 5.2.10 where the tapered CPW phase shifter with narrower strip width ($2s$ = 10 μm) possessed higher losses compared to the CPW phase shifter ($2s$ = 25 μm). In addition, the effective loss tangent was seen to improve with the increase of bias voltage to up to 100 *V*, with values of tan δ_{eff} decreasing from 0.15 to 0.10 and 0.23 to 0.14 for the CPW and tapered CPW phase shifters respectively. The improvement of tan δ_{eff} with bias voltage is consistent with work by Zimmermann *et al.* [123] and Jakoby *et al.* [15]. This has further accounted for the improved insertion and return losses of both phase shifters with increasing bias voltage shown in Figure 5.2.3 and Figure 5.2.4.

There is currently no known analytical technique or expression which can be used to accurately extract the losses due to the BST thin-film from the measured total loss of the device, which includes the loss attributed to the silver conductor. By estimating the loss tangent of the BST thin-film (tan δ_{BST}) and using the dielectric constant values of the BST thin-film obtained from characterisation (shown in Figure 5.2.8), the performance of the phase shifters was modelled using Sonnet, a commercial electromagnetic planar simulator based on method-of-moments, to reproduce the raw experimental data, i.e. the scattering-parameters. Figure 5.2.11 and Figure 5.2.12 present a comparison between the simulation results from Sonnet and the corresponding experimental data at 0 *V*, 40 *V* and 100 *V* for the CPW and tapered CPW phase shifter respectively. The main input parameters for Sonnet simulations are the dielectric constant, dielectric loss, thickness of the BST thin-film and MgO substrate, and geometry of the devices, as previously shown in Figure 5.2.8 and Table 5.2.1. The conductivity of the 300 nm thick silver metallisation was assumed to be 6.17×10^7 S/m.

As seen from Figure 5.2.11 and Figure 5.2.12, a reasonably close agreement between the simulation results and the experimental data is observed, particularly at lower frequencies (below 10 GHz) and bias voltages (under 40 *V*). The more

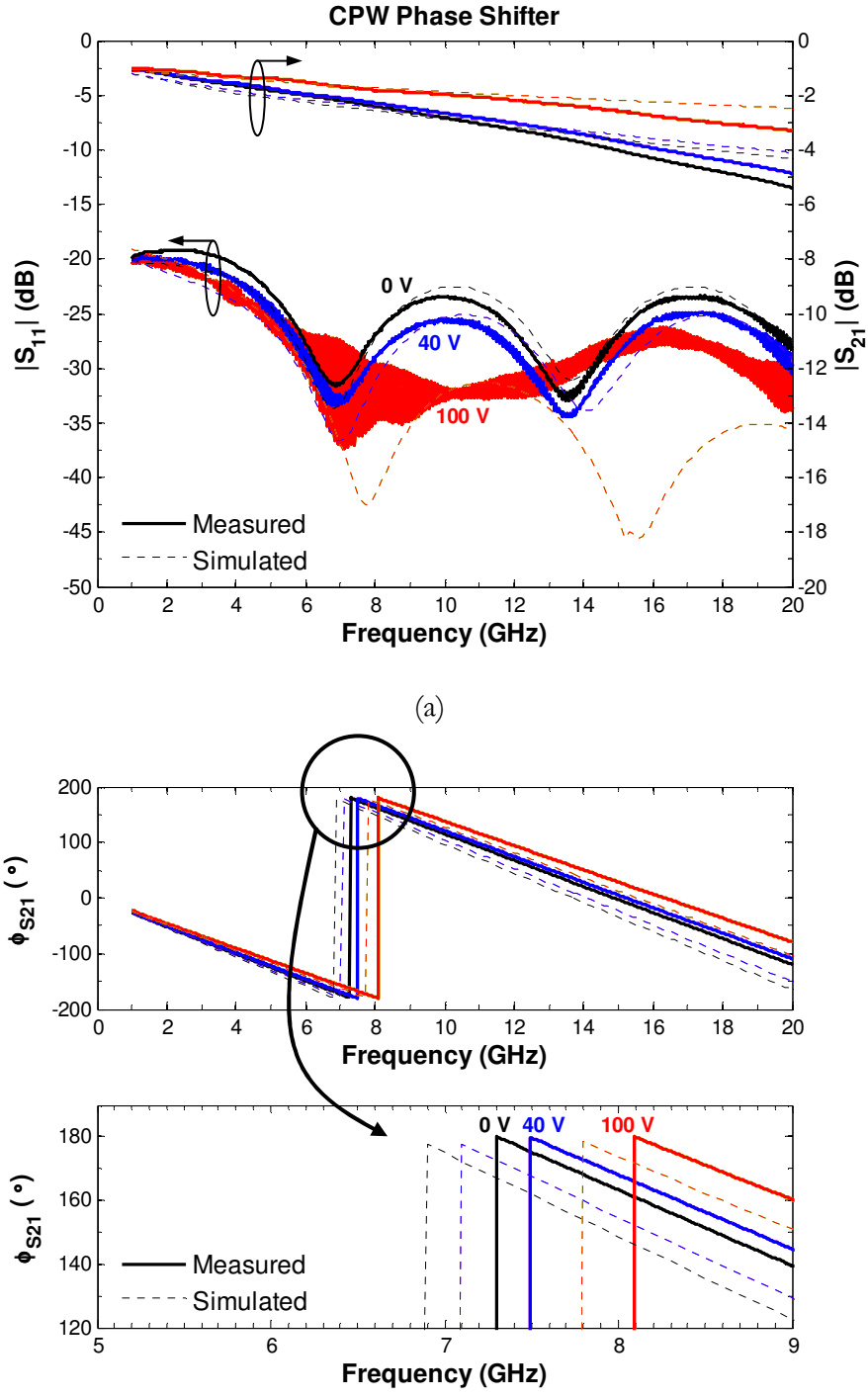

Figure 5.2.11: Comparison of measured (solid lines) and simulated (dashed lines) (a) scattering-parameters, and (b) phase of the CPW phase shifter at various bias voltages.

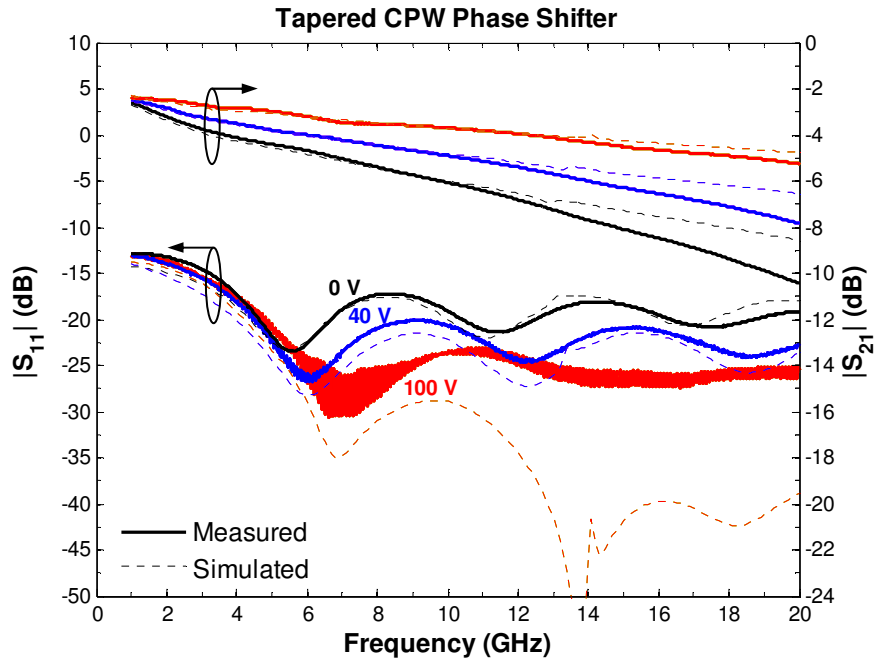

(a)

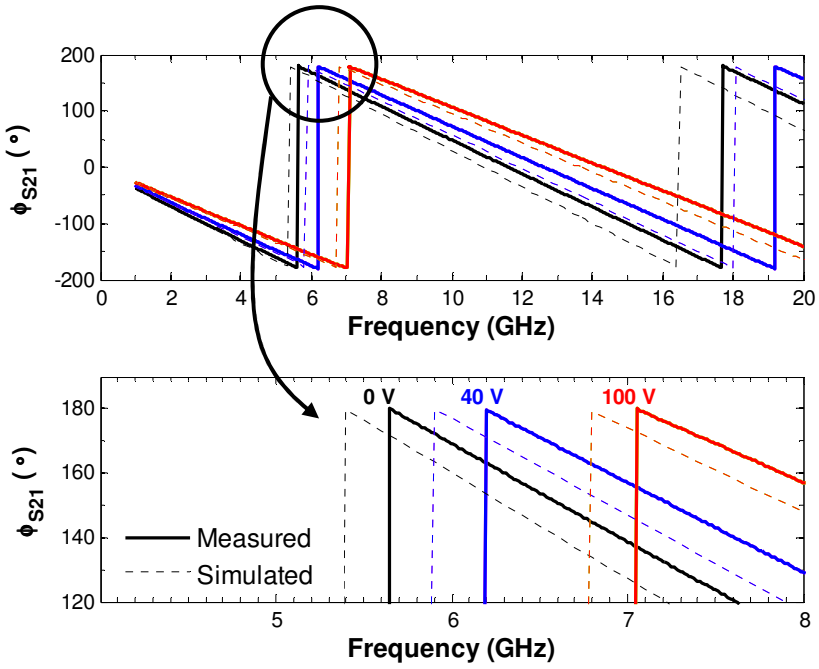

(b)

Figure 5.2.12: Comparison of measured (solid lines) and simulated (dashed lines) (a) scattering-parameters, and (b) phase of the tapered CPW phase shifter at various bias voltages.

pronounced discrepancy above 10 GHz and 40 V could be attributed to unaccounted parasitic inductances and capacitances, as well as the dispersive dielectric constant of the BST thin-film. A small shift of phase between both results is observed in both figures. Such phase difference could be due to the difference or error in the dielectric constant of the BST thin-film extracted from the original experimental data.

In addition, the discrepancy in the simulation results and the experimental data could be attributed to several other aspects, namely (a) the preliminary error of the full two-port calibration near zero frequency; (b) simulation limitation in using finite cell size in compensation to simulation time; and (c) the ideal assumption in the simulation where discrepancy in conductor surface roughness, substrate thickness and dielectric constant distribution across the BST thin-films were neglected. Nonetheless, the reasonably close agreement between the simulated and measured results has indicated a good estimation of the loss tangent and extraction of the dielectric constant of the BST thin-film (tan δ_{BST} and ε_{BST}).

The values of tan δ_{BST} used in the simulations for both phase shifters as a function of the real part of the BST thin-film dielectric constant (ε'_{BST}) is presented in Figure 5.2.13. When ε'_{BST} = 1800 or with no applied electric field across the conductors, the loss tangent of BST thin-film amounts to a maximum of tan δ_{BST} = 0.12. The loss of the film decreased to by 50% when ε'_{BST} dropped to 940 or increased of applied electric field to 3.13 V/μm. The improvement of tan δ_{BST} with the decrease in ε'_{BST} was expected as previously observed from the effective loss tangent tan δ_{eff} (i.e. the overall losses of the device) in Figure 5.2.10.

Two designs of a CPW structure phase shifter of delay-line type have been designed and measured. The performance of the tapered CPW phase shifter proved superior to the standard CPW configuration at a given bias voltage due to its narrower gap width, which allowed a greater change of dielectric constant within the BST layer. A phase shift of 105° at 100 V (E = 3.13 V/μm) and a figure-of-merit of 14°/dB at 20 GHz was achieved with the tapered CPW phase shifter based on

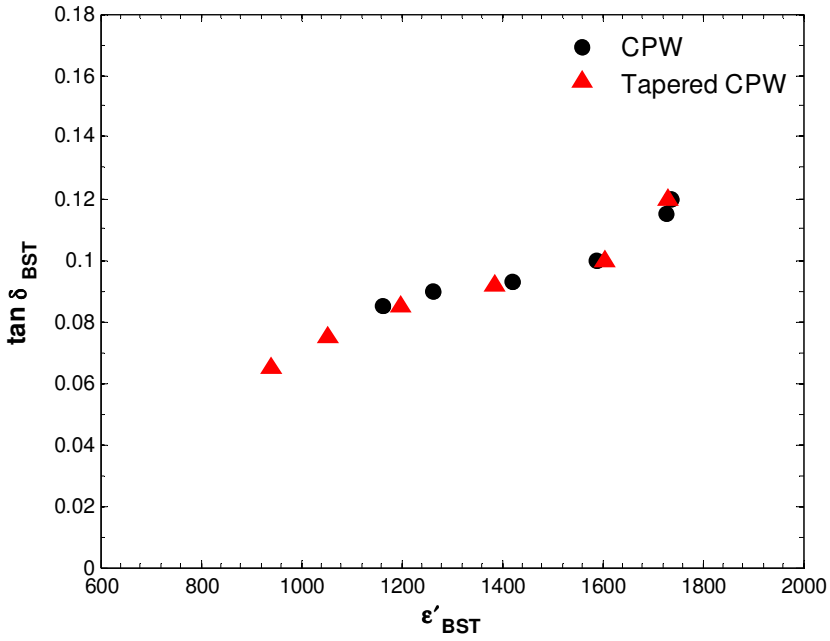

Figure 5.2.13: Loss tangent of the BST thin-film, tan δ_{BST} as a function of real part of the BST thin-film dielectric constant, ε'_{BST}. ③ and ⑩ represent the values used in the Sonnet simulations of CPW and tapered CPW phase shifter, respectively.

0.35 μm thick of $Ba_{0.5}Sr_{0.5}TiO_3$ thin-films on MgO substrate. The results were comparable to other published ferroelectric-based phase shifter designs [38, 67, 127, 128].

Sherman *et al.* [67] reported work using a tapered CPW phase shifter based on 0.3 μm thick $Ba_{0.3}Sr_{0.7}TiO_3$ thin-films on an alumina substrate with 1.65 μm stacks of Au/Ti conducting layers. They showed that a phase shift of 34° was obtained with a voltage of 250 *V* or electric field of 9 *V*/μm, corresponding to a figure-of-merit of 16°/dB at 20 GHz. Kim *et al.* [38] proposed a simple CPW phase shifter comprising 0.5 μm thick $Ba_{0.5}Sr_{0.5}TiO_3$ thin-films on an MgO substrate with 2 μm of Au conductors. A phase shift of 5.5° was achieved with 30 *V* which corresponded to an electric field of 1.5 *V*/μm, and resulted in a figure-of-merit of 3°/dB at 10 GHz. In 2000, Kirchoefer *et al.* [127] reported research on a similar structure which achieved

30° of phase shift with a bias voltage of 40 *V*, giving an electric field of 1.5 *V*/μm and a figure-of-merit of 4°/dB at 20 GHz. In the same year, Kozyrev *et al.* [128] tested a tapered CPW phase shifter based on 8 μm of BST on an MgO substrate and produced a 360° phase shift with 350 *V* or electric field of 8.75 *V*/μm at 30 GHz. The corresponding figure-of-merit is approximately 45°/dB.

The figure-of-merit of delay-line type ferroelectric-based phase shifters are generally lower than alternative types of ferroelectric-based phase shifters including loaded-line (i.e. periodically loaded with ferroelectric varactor) and reflection type [67, 69, 129] devices. Nonetheless, its wideband capability together with ease of fabrication and simple design in comparison to loaded-line and reflection type variants, have ensured delay-line type CPW phase shifters remain competitive for frequency-agile applications.

The research carried out using CPW phase shifters were the preliminary step towards using BST thin-films for designing CBCPW phase shifters. BST-based CBCPW phase shifters play a crucial role in the tunable attenuator described in Chapter 6 and will be discussed in the following section.

5.3 CBCPW Phase Shifter

Two different configurations of a conductor-backed coplanar waveguide (CBCPW) phase shifter are presented in this section. The first, similar to the earlier CPW phase shifter, is based on a multilayer configuration comprising ~0.35 μm thick BST thin-films on a 500 μm thick MgO substrate with 300 nm layer of silver metallisation (as shown in Figure 5.3.1(a)), where the phase change is achieved by the application of bias voltage across the centre strip and the in-plane ground of the CBCPW line. The second configuration consists of a 254 μm thick Duroid substrate (ε_r = 10.2) with 17 μm thick coating of copper metallisation. In contrast to the ferroelectric-based phase shifter, the phase change of the CBCPW phase shifter based on Duroid substrate is realised by placing other dielectric materials of different

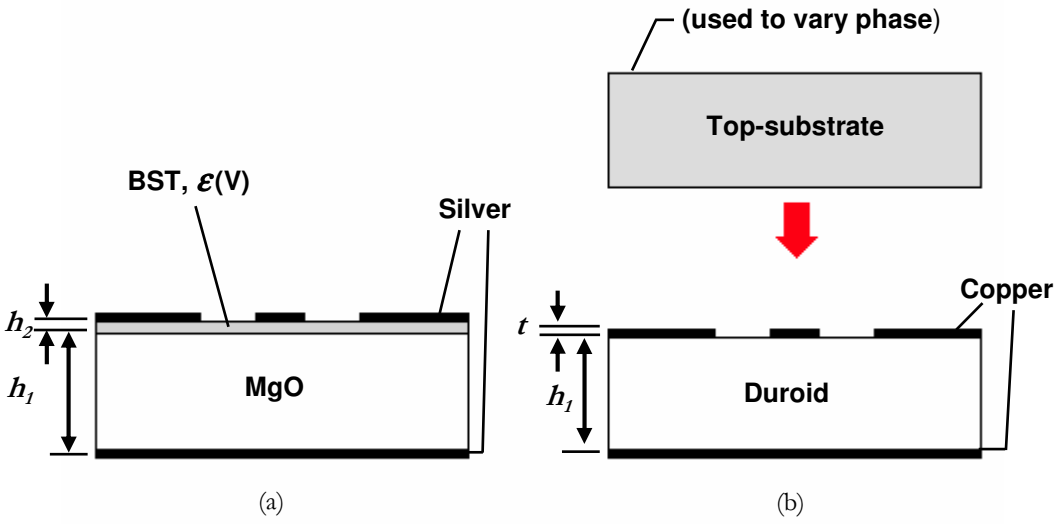

Figure 5.3.1: Cross-section of CBCPW phase shifter based on (a) BST, and (b) Duroid substrate.

dielectric constant ε_r on its top surface, as illustrated Figure 5.3.1(b). Both configurations play a key role in the tunable attenuator device described in Chapter 6, which is intended for operation with a centre frequency of 6 GHz. The simulated responses of the CBCPW phase shifters described here was performed over a frequency range up to 8 GHz.

As with the CPW design, the characteristics of the CBCPW lines were determined using the conformal mapping equations developed by Gevorgian *et al.* [84], as previously described in Section 3.4.3 and 3.4.4. It should be noted that the design parameters of the CBCPW line (i.e. width of centre strip *w*, gap *g*, length of the line) were chosen to achieve an optimal trade-off between the line impedance, phase shift and insertion loss, at a given thickness and dielectric constant of the substrates used. For BST-based phase shifter, the CBCPW line was designed to approach a 50 Ω impedance line whilst ensuring a reasonable width of gap in order to achieve a relatively high electric field in the vicinity of the centre strip. Figure 5.3.2

shows the design layout of the CBCPW phase shifter with the corresponding design parameters used for both the BST and Duroid configurations listed in Table 5.3.1.

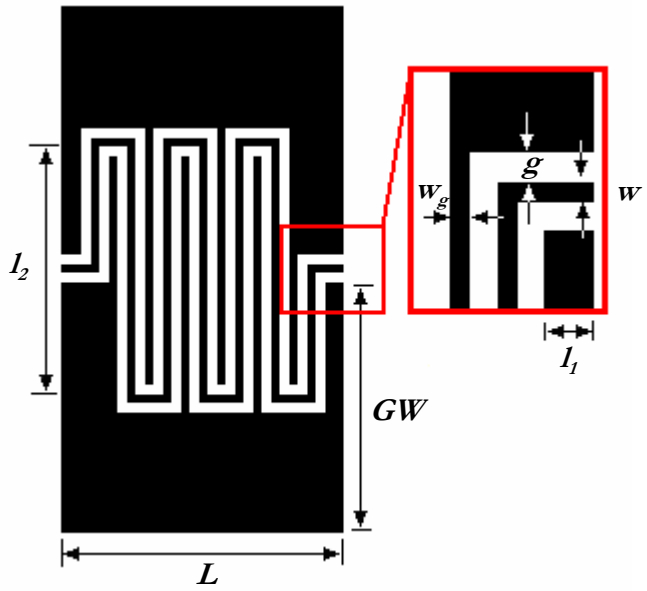

Figure 5.3.2: Layout of the meandered CBCPW phase shifter.

	BST-based CBCPW Phase Shifter	**Duroid-based CBCPW Phase Shifter**
w	20 μm	60 μm
g	40 μm	120 μm
w_g	100 μm	60 μm
GW	1.72 mm	2.31 mm
l_1	140 μm	120 μm
l_2	1.90 mm	2.50 mm
L	1.58 mm	2.70 mm

Table 5.3.1: Design parameters of CBCPW phase shifter based on BST and Duroid substrates.

The CBCPW line was meandered in the manner shown in Figure 5.3.2 to maximise the use of substrate area, but more importantly, to increase the total physical length of the line in order to maximise the phase change of the propagated microwave signal. The BST dielectric constant ε_{BST} curve extracted from experimental measurements of the CPW phase shifter (as previously shown in Figure 5.2.8) was employed in all simulations detailed in the current and subsequent chapter. The loss tangent of the BST thin-films was assumed to be 0.12 at zero electric field and decreased to 0.07 at 2.5 $V/\mu m$, as depicted in Figure 5.2.13.

The Sonnet simulated scattering-parameters of the CBCPW phase shifter based on the BST substrate is shown in Figure 5.3.3(a). As with the CPW phase shifter, the phase change of the CBCPW phase shifter was realised by varying the bias voltage across the centre signal strip and the ground planes. With a total meander-line length of approximately 1.31 cm and a bias voltage of up to 100 V, the maximum insertion loss of the phase shifter was simulated to be less than 7 dB with the return loss better than 21 dB for all states of bias voltages over the frequency band of 3 to 8 GHz. It was observed that both insertion and return losses of the phase shifter improved as bias voltage increased. Figure 5.3.3(b) depicts the differential phase shift and figure-of-merit as a function of frequency of a CBCPW phase shifter on BST substrate at different bias voltages. With a bias voltage of 100 V which equates to an electric field of 2.5 $V/\mu m$, a continuously variable phase shift of 68° was predicted at 6 GHz, which corresponded to a figure-of-merit of 12.6°/dB. As predicted, under identical electric field strength and frequency levels, the meandered CBCPW line showed an approximate two fold increase in phase shift with an improved figure-of-merit as compared to the tapered CPW phase shifter presented in Section 5.2.1 (Figure 5.2.6 and Figure 5.2.7).

In contrast to the BST-based phase shifter, the phase change in the Duroid substrate configuration was achieved by placing other dielectric materials of different dielectric constant ε_r on its top surface, as shown in Figure 5.3.4(a). With the meander conductor line sandwiched between the top-substrate and Duroid substrate,

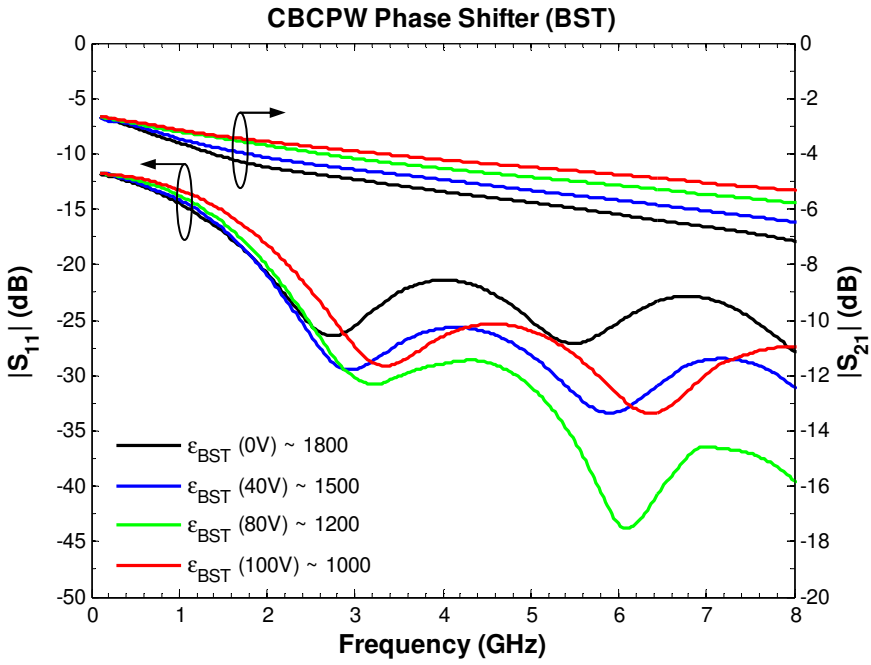

(a)

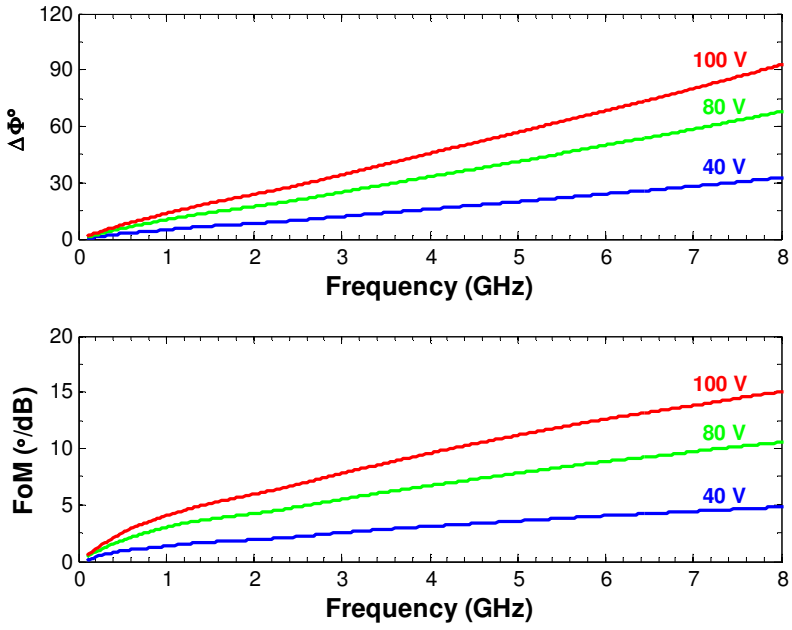

(b)

Figure 5.3.3: Simulated (a) scattering-parameters, (b) differential phase shift, and figure-of-merit of CBCPW phase shifter based on BST and MgO substrate with different bias voltages.

the effective dielectric constant ε_{eff} of the structure changes, which causes any signal travelling into the phase shifter to alter and hence resulting in a phase change.

It should be noted that while performing the experimental measurements, a weight or mass was placed over the top-substrate in an attempt to eliminate any air gaps between the top-substrate and the conductor line. Despite use of the weight however, a thin layer of air would still be inevitably present at the interface due to the relative roughness of the conductor surface, as illustrated in Figure 5.3.4(b). Table 5.3.2 lists the properties of the dielectric materials that were used as the top-substrate of the Duroid-based CBCPW phase shifter.

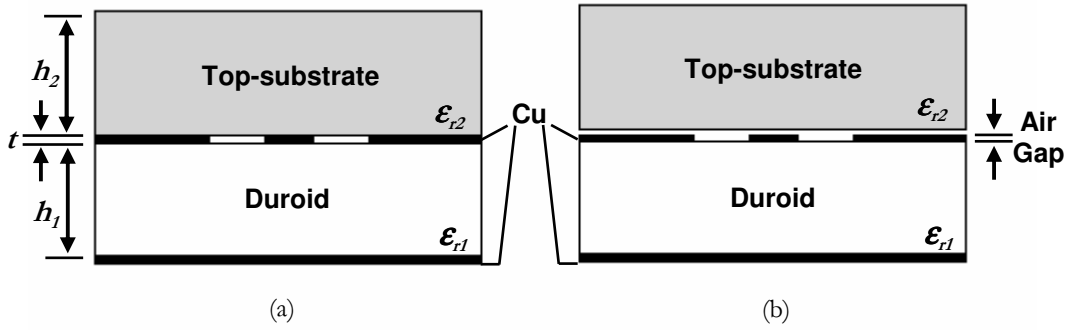

Figure 5.3.4: Cross-section of CBCPW configuration based on Duroid substrate and loaded with top-substrate (a) in ideal case, and (b) with air gap layer between top-substrate and conductors.

Dielectric material	**Thickness (h_2)**	**Dielectric constant (ε_{r2})**	**Loss tangent (tan δ)**
Pyrex® 7740 Glass	1.1 mm	4.6	0.0050
Magnesium Oxide (MgO)	0.5 mm	9.8	0.0001
Lanthanum Aluminate ($LaAlO_3$)	1.0 mm	24.5	0.0003

Table 5.3.2: Properties of the dielectric material to be used as the top-substrate of the phase shifter [99, 130-132].

Figure 5.3.5 details the simulated scattering-parameters, differential phase shift and figure-of-merit of the Duroid-based CBCPW phase shifter with various dielectric materials on the surface. The simulations were performed under ideal conditions where no air gap layer was present at the interface. With a total meander-line length of approximately 1.72 cm, the maximum insertion loss of the phase shifter was found to be less than 1.5 dB, with the return loss better than 10 dB for all types of top-substrate over the frequency band of 3 to 8 GHz. The return loss improved as ε_{r2} of the top-substrate increased and indicated that the line impedance was approaching that of a 50 Ω line. A maximum phase shift of 230° was predicted at 6 GHz, which corresponded to a figure-of-merit of 220°/dB when the phase shifter was loaded with a 1 mm thick piece of $LaAlO_3$.

Due to the impedance mismatch in the line, several ripples were observed in the plot of insertion losses. Insertion loss is a combination of the loss in the device and the loss of the signal reflected back due to the impedance mismatch. When the meander-line is of the order of multiple half-wavelengths, minimum insertion loss occurs as reflection in the line is at its lowest level. This therefore explains the origins of the ripples observed in the graph of *FoM* versus frequency. In addition, the emergence of spurious responses at frequency regime of 6 - 7 GHz when loaded with a $LaAlO_3$ top-substrate was noted. This was thought to be due to the excitation of the unwanted slotline mode in the meandered CBCPW phase shifter, which is a result of the path length difference between the inner slot and the outer slot of the meander line previously mentioned in section 3.6.4.

As a layer of air is quite often present between the top-substrate and conductor line in most practical cases, an evaluation of the effect of varying air gap thickness on device response was carried out. Figure 5.3.6 plots the differential phase shift as a function of air gap thickness at 6 GHz. As shown in the figure, a significant decrease in differential phase shift was observed as air gap thickness increased. The phase shift decreased more than two fold when the air gap thickness was several microns thick. Such behaviour was attributed to the decrease in effective dielectric constant of the structure as the air gap layer increased and resulted in a lower continuous phase shift.

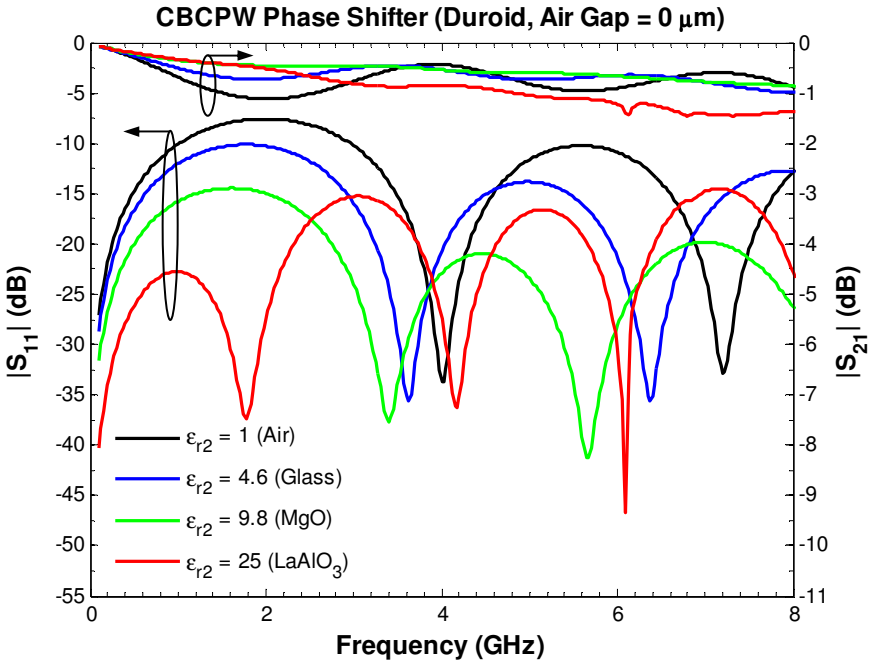

(a)

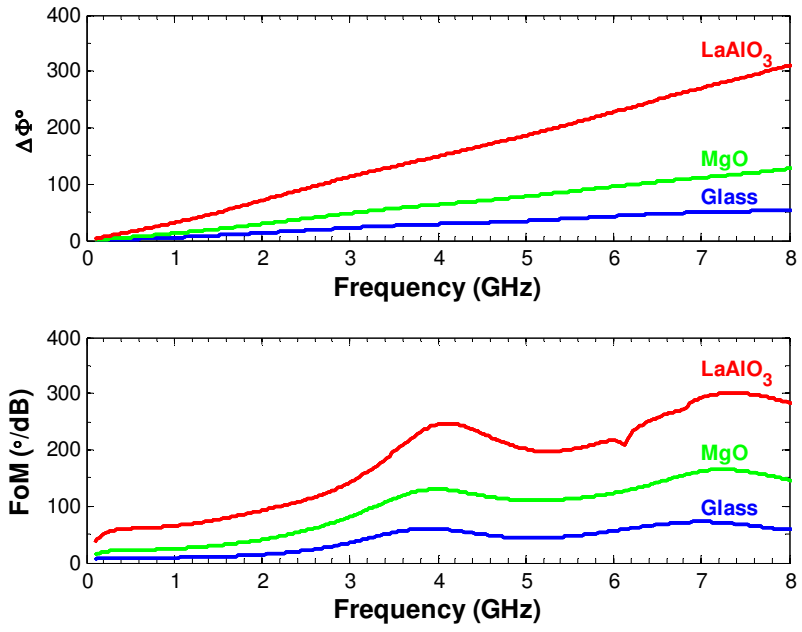

(b)

Figure 5.3.5: Simulated (a) scattering-parameters, (b) differential phase shift, and figure-of-merit of CBCPW phase shifter based on Duroid substrate and various top-substrate.

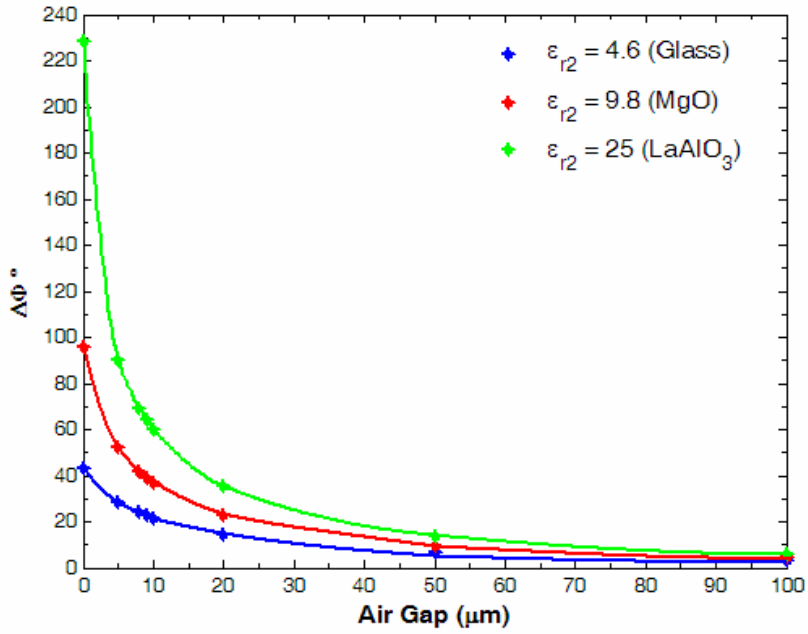

Figure 5.3.6: Differential phase shift of CBCPW phase shifter based on Duroid substrate as a function of air gap thickness at 6 GHz.

The simulated frequency response of the CBCPW phase shifter based on a Duroid substrate having an 8 μm thick layer of air at the top-substrate-conductor interface is shown in Figure 5.3.7. An obvious decrease in phase shift was observed when the phase shifter was separately loaded with Glass, MgO and $LaAlO_3$ on its surface, thereby giving a phase shift of only 24°, 42° and 69° at 6 GHz, and a corresponding figure-of-merit of 30°/dB, 55°/dB and 91°/dB respectively. Similarly as before, ripples were observed in the plot of insertion loss and figure-of-merit due to the impedance mismatch in the line. Additionally, the excitation of the unwanted slotline mode when loaded with $LaAlO_3$ was present at 7 GHz.

Two configurations of meandered CBCPW phase shifter of delay-line type, which are key components in the tunable attenuator described in the following chapter, have been designed and presented. The simulated responses of the meandered CBCPW phase shifter based on BST/MgO substrates displayed superior performance compared to the measured results of the tapered CPW phase shifter

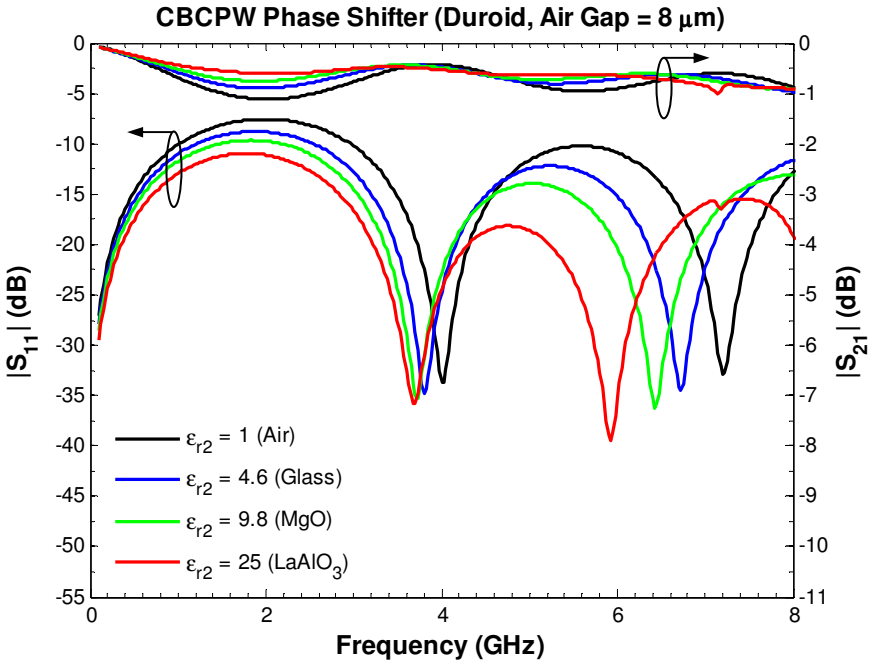

(a)

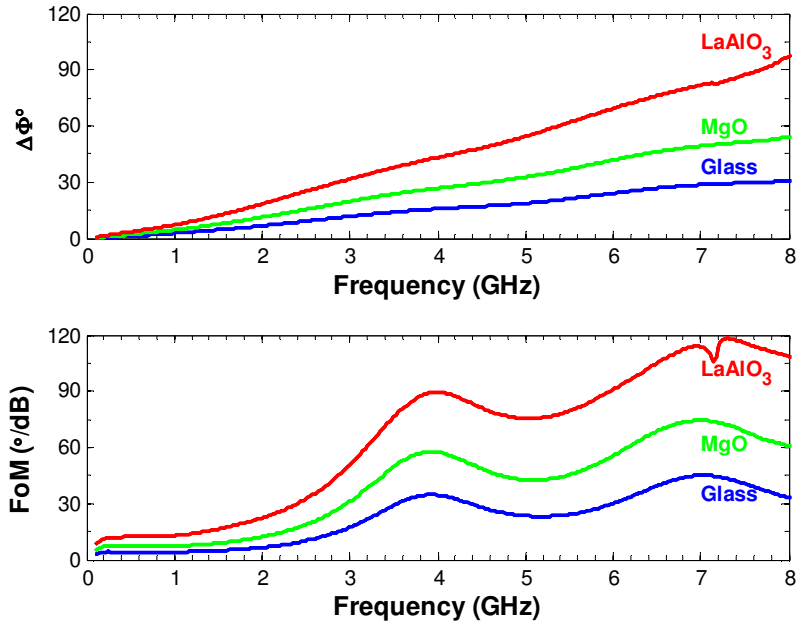

(b)

Figure 5.3.7: Simulated (a) scattering-parameters, (b) differential phase shift, and figure-of-merit of CBCPW phase shifter based on Duroid substrate with 8 μm thick of air gap.

based on similar multilayer configuration presented in the previous section. With a bias voltage of 100 *V* or an equivalent electric field of 2.5 *V*/μm, the BST-based meandered CBCPW phase shifter predicted a continuously variable phase shift of 68° at 6 GHz, which corresponded to a figure-of-merit of 12.6°/dB. This was not surprising as the total length of the meander CBCPW line was nearly two times longer than the tapered CPW line design.

Conversely for a meander CBCPW phase shifter based on Duroid substrate, a maximum phase shift of 230° was predicted at 6 GHz with a figure-of-merit of 220°/dB when loaded with $LaAlO_3$ on its surface under ideal circumstances, where no air gap layer was present at the top-substrate-conductor interface. A dramatic decrease in phase shift was observed when a layer of air gap was present at the interface. With an air gap of approximately 8 μm , the predicted phase shift reduced by approximately two-thirds to 69° at 6 GHz, with a figure-of-merit of 91°/dB.

The simulations performed on both the BST and Duroid-based CBCPW phase shifters were intended mainly to predict the likely phase shift obtainable for each configuration as background information for the tunable attenuator design. It was therefore thought unnecessary to experimentally validate the simulated results of the phase shifters as the ferroelectric tunable attenuator (incorporating the BST-based CBCPW phase shifter described here) detailed in the following chapter will be verified through comparison with data obtained from experimental trials performed with an equivalent Duroid-based attenuator.

5.4 Conclusions

The fabrication of CPW and tapered CPW phase shifters on BST thin-films and MgO substrate has been successfully performed. Characterisation of the BST dielectric properties using probe station was demonstrated. A phase shift of 105° was produced at 20 GHz on the tapered CPW phase shifter, with an insertion loss of about 10.6 dB, giving a figure-of-merit of 14°/dB. A high tunability of ~48% was

achieved at 3.13 *V*/μm (or at bias voltage of 100 *V*).

This work was carried out as a preliminary step towards using BST ferroelectric thin-films for designing CBCPW phase shifters, which are key components in the tunable attenuator described isn the following chapter. The design and the associated simulated response of CBCPW phase shifters based on BST/MgO and Duroid substrates was discussed while the effect of air gap layer at the top-substrate and conductor interface was also considered.

Chapter 6

Tunable Attenuator

6.1 Introduction

While many ferroelectric-based tunable microwave devices such as varactors, tunable resonators, filters and phase shifters [1, 3, 39, 41, 44, 45, 59, 60, 62, 68, 70-73, 128] have been studied extensively over the last few decades, there has been little or no work reported on the use of ferroelectric thin-films for tunable attenuators. In light of its potential benefits, current research involving a novel topology of a tunable attenuator employing ferroelectric thin-films is presented.

In much of the previous works, tunable attenuators have been implemented employing various methods and technologies. In [32], tunable attenuators were designed using semiconductor varactors in a cascade manner in order to achieve controlled attenuation. The measured attenuation (or controlled change of the

insertion loss) was between 0.25 dB to 4.4 dB at a frequency of 1.7 GHz with 2^4 discrete amplitude states. In addition, the fabrication process of the semiconductor-based attenuator was both complicated and time consuming, as the device required several layers of metallisation and substrates.

An alternative configuration of tunable attenuator known as the Mach-Zehnder electro-optic modulator comprises two sections involving an optical waveguide Mach-Zehnder interferometer (MZI) and coplanar waveguide (CPW) line [133-135]. Here, the modulator is designed based on Lithium Niobate ($LiNbO_3$) substrate which exhibits a Pockels electro-optic effect where its refraction index varies proportionally to the applied electric field. Changing the applied electric field at which the modulator operates determines whether the two path signals interfere constructively or destructively at the output, and thereby control the attenuation and linearity of the modulator output. Similar to the semiconductor-based attenuator [32], the design and fabrication process of electro-optic modulators is both complicated and time consuming, as the modulator requires optical waveguides to be properly aligned and embedded in the substrates while the interaction length (region with MZI and CPW) has to be suitably selected in order to achieve an optimal response.

The ferroelectric-based tunable attenuator proposed here is not only smaller in size, but achievable through a less complex fabrication process as the device can be realised into one integrated planar circuit with only a single layer of metallisation. More importantly however, is that the use of ferroelectric material allows continuous variation of attenuation under controlled bias voltages.

The function of an attenuator is effectively the opposite of an amplifier. While an amplifier provides gain, an attenuator is used to generate loss or a gain of less than 1. This passive device is used to attenuate the amplitude or power of a signal without appreciably distorting its waveform. The tunable attenuator in this work utilises the non-linear dielectric constant of ferroelectric materials, together with the principle of constructive and destructive interference by integrating two tunable ferroelectric phase shifters in parallel to produce amplitude shifting or attenuation of signals. Figure 6.1.1 shows a schematic diagram of the device.

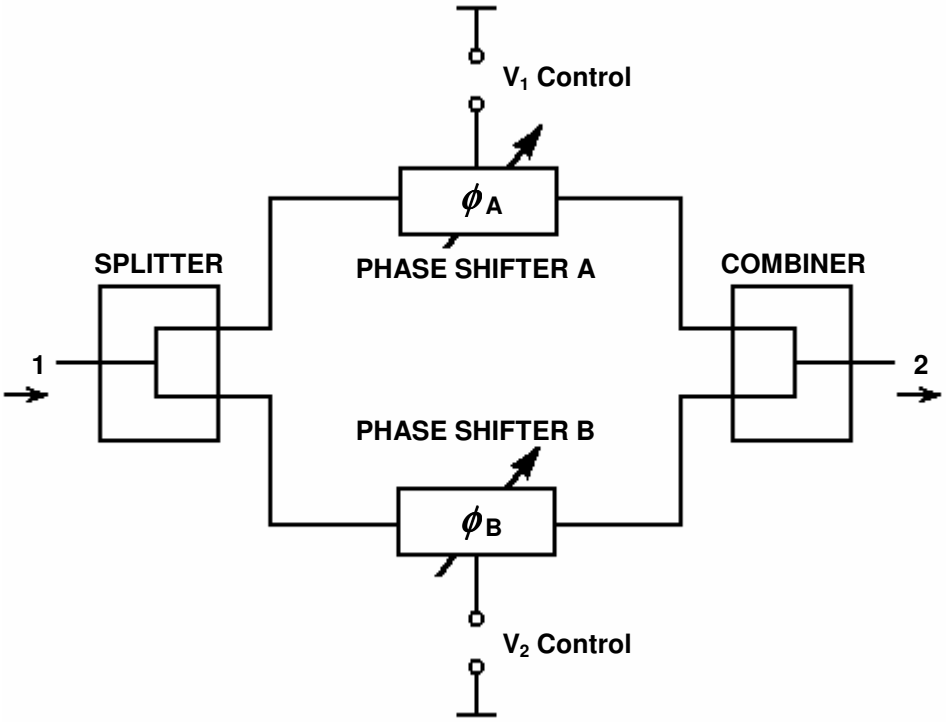

Figure 6.1.1: Schematic diagram of the tunable attenuator.

A microwave signal is fed into the splitter at port 1 where it is divided into two identical branches. The corresponding output microwave signal at port 2 is the sum of the output signals from the two phase shifters, A and B. Two external bias voltages, V_1 and V_2 are applied to control the phase shift of each phase shifter. Consequently, the output signal amplitude at port 2 is a function of the phase difference of the two branches, which are controlled by the respective tunable phase shifters. In other words, by changing the electric field on phase shifters A and B will determine whether the two branch signals interfere constructively or destructively at the output, and thereby control the amplitude or attenuation of the input microwave signal.

The ferroelectric tunable attenuator implemented here was based on Barium Strontium Titanate ($Ba_{0.5}Sr_{0.5}TiO_3$ or BST) ferroelectric thin-film of thickness ~0.35 μm on 500 μm thick of Magnesium Oxide (MgO) substrate, as shown in

Figure 6.1.2(a). By altering the electric field across the phase shifter, the dielectric constant of the BST thin-film will undergo substantial change causing the phase velocity of waves propagating through the phase shifter to alter accordingly. Hence, a desired continuous attenuation can be achieved simply by controlling the external bias voltages, V_1 and V_2.

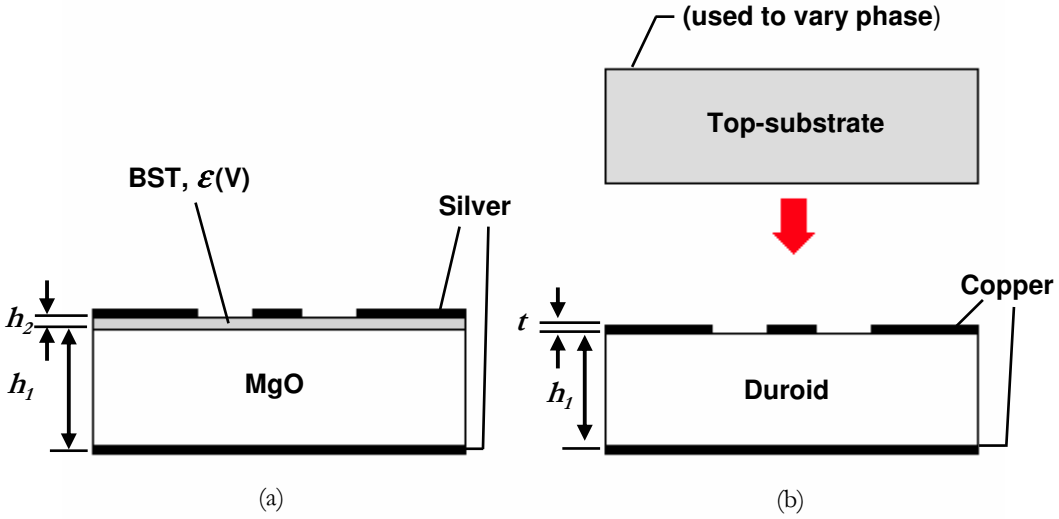

Figure 6.1.2: Cross-section of tunable attenuator based on (a) BST substrate and (b) Duroid substrate.

Due to time constraints, experimental measurements on the BST-based tunable attenuator device could not be performed. Indirect verification of the simulation results and operating principle of the proposed ferroelectric attenuator was however carried out through measurement and comparison with an equivalent device fabricated using Roger/Duroid 6010LM substrate of thickness 254 μm having a relative dielectric constant of 10.2, as shown in Figure 6.1.2(b). As the ε_r of the Duroid substrate was constant, the signal attenuation was achieved by putting an alternative dielectric material of different ε_r on top of the phase shifter. With the conductors sandwiched between the top-substrate and Duroid layer, the effective dielectric constant ε_{eff} of the structure was altered, thus causing a phase change of the

signal travelling into the device. The degree of attenuation attainable using such an approach is however highly dependent on the dielectric constant of the top-substrate loaded on the surface of the phase shifter. Typically, a larger range of attenuation can be achieved by utilising materials that possess high dielectric constant values, which results in larger phase changes being obtained.

With the same principle of operation, where two tunable phase shifters were utilised in parallel to achieve signal attenuation, this design layout was maintained for both the BST- and Duroid-based tunable attenuators. The dimensions of the circuit lines for the individual tunable attenuators were however different, not least due to the dissimilar properties of the substrates used but also the variation in respective substrate thicknesses. Similar to the phase shifter detailed in the previous chapter, experimental microwave measurements for the tunable attenuator were performed at room temperature using a Cascade Microtech Summit 9000 analytical probe station with 250 μm pitch ground-signal-ground (GSG) probes connected to a vector network analyser (Agilent E8361A).

As illustrated in Figure 6.1.1, the tunable attenuator described comprises several circuit elements, namely circuit transitions, transmission line discontinuities, power splitter/combiner and phase shifters. In the following sections, the design and response of each element, based on BST and Duroid substrates, will be outlined. This will be followed by the overall design layout and response of the whole device for the two substrates. Both attenuators were designed to operate at a centre frequency of 6 GHz under room temperature conditions.

6.2 Power Divider/Combiner

A tee-junction, as previously mentioned in Chapter 3, was used either for power splitting or combining. As a simple three-port network, it can be implemented in virtually any type of transmission line media. However, drawbacks of a tee-junction power divider/combiner include the problem of mismatch at each of the

ports in addition to the lack of isolation between output ports. While the use of a resistive tee-junction is a possible solution for the matching problem at all ports, it does not overcome the difficulty associated with isolation and can lead to increased power loss due to the inherent resistive structure of the element.

6.2.1 Wilkinson Power Divider

In 1960, E.J. Wilkinson invented what is now known as the Wilkinson power divider [136], a three-port network with all ports simultaneously matched as well as isolation between output ports. The Wilkinson power divider is particularly useful as it possesses the property of giving zero loss when the output ports are matched, where only reflected power is dissipated. Although the Wilkinson power divider can be made to give arbitrary power division, the two-way equal-split (3 dB) design is the most commonly used.

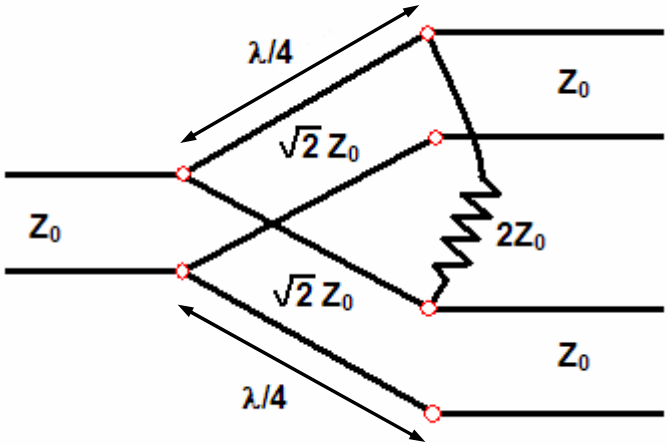

Figure 6.2.1:Two-way, equal- split Wilkinson power divider.

In the simplest two-way, equal-split Wilkinson power divider configuration, as that shown in Figure 6.2.1, a signal fed into the input port with a characteristic impedance of Z_0 can be divided into two in-phase and of equal amplitude signals by

way of two transmission lines with impedances of $\sqrt{2}\,Z_0$, each having an electrical length of one-quarter wavelength at the operating frequency. The quarter wavelength ($\lambda/4$) of the signal is related to the operating frequency by the following expression:

$$\frac{\lambda}{4} = \frac{c_0}{4 f_0 \sqrt{\varepsilon_{eff}}} \tag{6.2.1}$$

where c_0 the speed of light in free space, f_0 is the centre operating frequency, ε_{eff} is the effective dielectric constant of the transmission line and λ is the wavelength at the operating frequency. Each transmission line acts as an impedance matching transformer. A perfect match with no reflection can only be achieved when the length of the transmission line is $\lambda/4$ or an odd multiple $(2n + 1)$ of $\lambda/4$.

A resistor of value $2Z_0$ is connected between each transmission line at the output and a common node. This resistor is the distinct feature of the Wilkinson power divider and is the reason that all ports can be simultaneously matched (provided the output ports are of impedance Z_0) as well as isolated where coupling effects of the output ports are avoided. Likewise, when used as a power combiner, the Wilkinson arrangement combines two input signals into an output signal. No power dissipation occurs provided that the input signals are in-phase, otherwise a portion of power will be dissipated through the resistors and the power delivered to the combiner output will reduce accordingly. Note that this simple Wilkinson power divider is a narrow-band device due to the quarter-wavelength transmission line sections. Additional transformer sections and isolation resistors would be needed if greater bandwidth is desired, although the added complexity would lead to increased physical size and insertion loss [137].

Figure 6.2.2 illustrates the ideal scattering-parameters of a two-way, equal-split Wilkinson power divider when all the output ports of impedance Z_0 are perfectly matched. The transmission lines of impedance $\sqrt{2}\,Z_0$ are $\lambda/4$ long at frequency f_0. At other frequencies, mismatch is observed as the $\lambda/4$ transmission line will appear

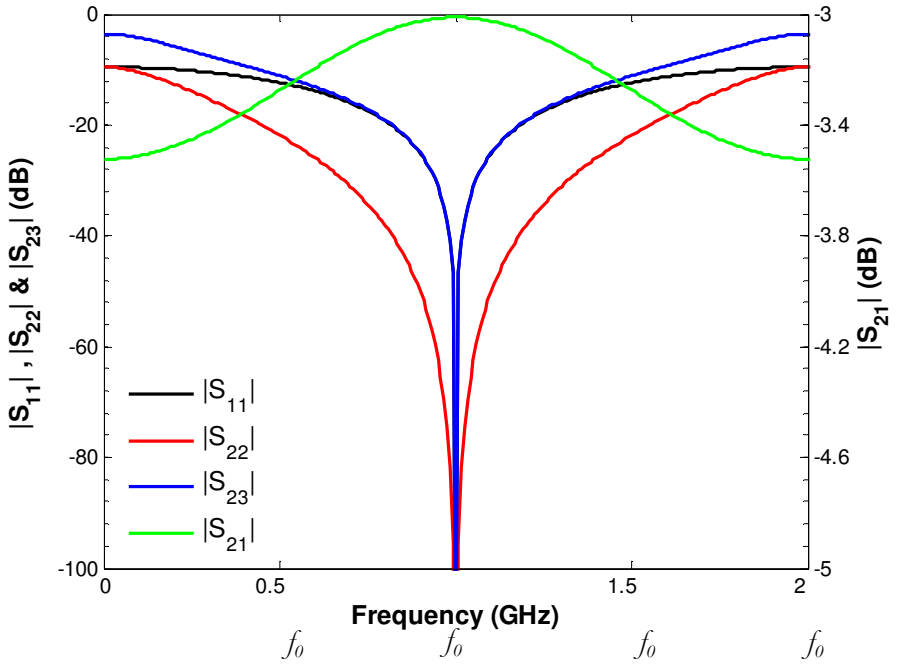

Figure 6.2.2: Ideal scattering-parameter responses of a two-way equal-split Wilkinson power divider. Port 1 is the input port; Port 2 and 3 are the output ports.

either electrically shorter or longer depending on the frequencies. Therefore, the further the operating frequency deviates from f_0, the greater the increase in return loss ($|S_{11}|$) at the input and output ports. With the use of a resistor of value $2Z_0$, good isolation $|S_{23}|$ between the output ports is achieved. An insertion loss ($|S_{21}|$) of 3 dB at frequency f_0 indicates an equal split or division in power.

Figure 6.2.3 depicts the layout of a two-way, equal-split Wilkinson power divider in microstrip form. Both input and output ports were of impedance 50 Ω. Due to space considerations, the $\lambda/4$ long microstrip line of impedance 70.7 Ω was meandered to reduce component 'footprint'. The isolation resistor used here was a 100 Ω chip resistor of dimension 0.5 × 1.0 × 0.35 mm. All tee-junctions and corners of the microstrip line have been optimally mitred in order to reduce reflection within the circuit, which otherwise would have degraded the performance of the power divider.

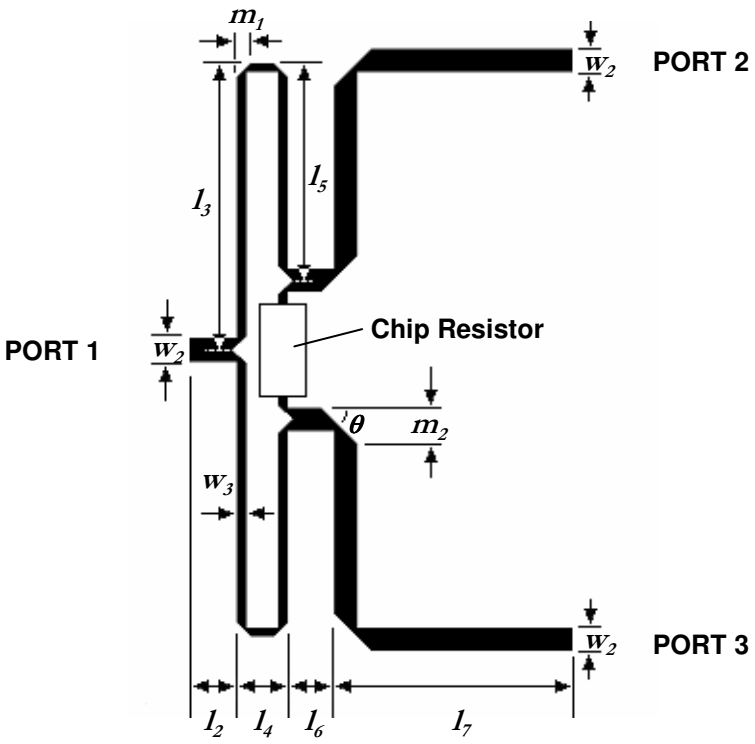

Figure 6.2.3: Layout of two-way, equal-split microstrip Wilkinson power divider.

The simulated scattering-parameters of a microstrip two-way, equal-split Wilkinson power divider based on BST and Duroid substrates are shown in Figure 6.2.4 and Figure 6.2.5, respectively. The loss tangent of the BST thin-film was assumed to be 0.12 with a dielectric constant of 1800 at 0 V. These values were taken from the experimental measurement from the previous chapter. At 6 GHz, the quarter-wavelength, 70.7 Ω-microstrip-line was approximately 5.1 mm long on the BST substrate and 5.8 mm long on the Duroid layer (ε_r = 10.2). As observed from both graphs, an extremely good match was achieved at 6 GHz where return loss was lowest at 60 dB and 36 dB for the BST and Duroid variants, respectively. At other frequencies, mismatch occurred as the length of the 70.7 Ω-microstrip-line was no longer a quarter-wavelength. Over the frequency band of 4 to 8 GHz, the return loss of the divider was better than 14 dB for the BST substrate and 15 dB for the Duroid substrate. The minimum insertion loss condition at 6 GHz indicates an equal split of power division. Due to the losses contributed by the conductor and dielectric materials, the insertion loss was slightly higher than the ideal 3 dB.

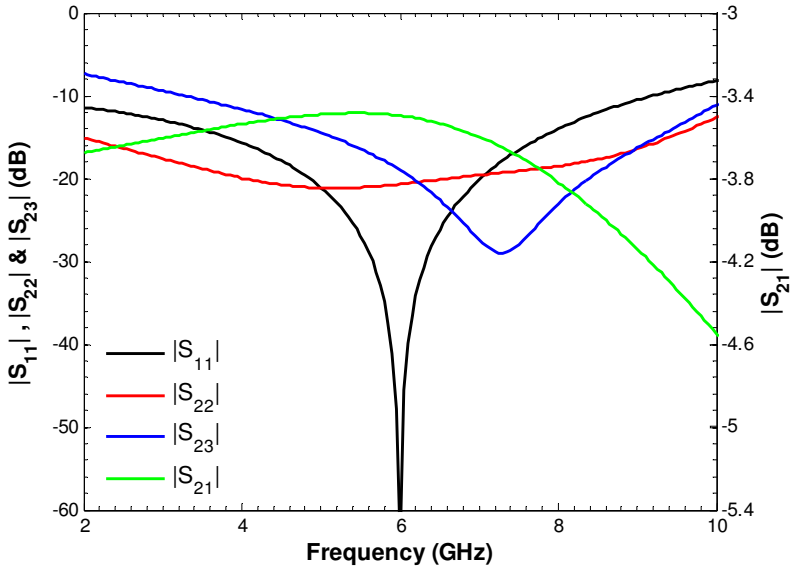

Figure 6.2.4: Simulated scattering-parameters of a two-way equal-split Wilkinson power divider in microstrip form on BST substrate.
(w_2=0.4mm, w_3=0.14mm, θ=45°, m_1=0.26mm, m_2=0.64mm, l_2=0.5mm, l_3=2.84mm, l_4=0.6mm, l_5=1.96mm, l_6=0.4mm, l_7=0.9mm, h_1=500μm, h_2=0.35μm, t=300nm, ε_{MgO}=9.8, ε_{BST}=1800)

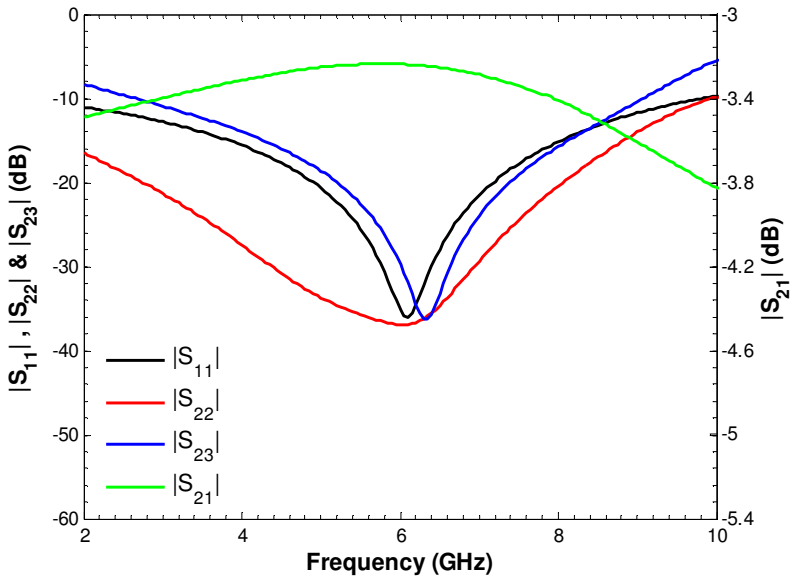

Figure 6.2.5: Simulated scattering-parameters of a two-way equal-split Wilkinson power divider in microstrip form on Duroid substrate.
(w_2=0.24mm, w_3=0.09mm, θ=45°, m_1=0.15mm, m_2=0.39mm, l_2=0.51mm, h_1=254μm, l_3=3.09mm, l_4=0.54mm, l_5=2.34mm, l_6=0.51mm, l_7=2.55mm, t=17μm, ε_1=10.2)

6.3 Integration of Various Components

The tunable attenuator proposed in this work employed conductor-backed coplanar waveguide (CBCPW)-to-microstrip transitions, microstrip Wilkinson power splitter/combiner and two meandered CBCPW phase shifters in parallel to achieve a controlled attenuation, as illustrated in Figure 6.3.1. The CBCPW-to-microstrip transition enabled experimental characterisation using a CPW probe pad without the need for device packaging. The strip-to-gap ratio of the CBCPW was kept appropriately in order to retain a constant 50 Ω characteristic impedance taper. The transition was followed by a three-port Wilkinson power splitter. Here, the input microwave signal at port 1 was fed into the splitter where it was divided into two identical branches. Each output of the splitter was then connected to an identical meander CBCPW phase shifter via a further CBCPW-to-microstrip transition before the signals, exiting from each phase shifter, rejoined through the three-port Wilkinson power combiner. Finally, the signal summation was directed back to the CPW probe pad via a microstrip-to-CBCPW transition at port 2.

The output microwave signal at port 2 was the sum of the signals leaving the phase shifters, where the output signal amplitude depended on the phase difference of the two branches, controlled by both phase shifter A and B. The relationship between the attenuation or magnitude of transmission coefficient of the attenuator ($|S_{21}|$), the phase of the transmission coefficient (φ_{S21}) and the phase of both phase shifters can be expressed as:

$$|S_{21}| = \cos\left(\frac{\varphi_A - \varphi_B}{2}\right) \tag{6.3.1}$$

$$\varphi_{S21} = \frac{\varphi_A + \varphi_B}{2} \tag{6.3.2}$$

where φ_A and φ_B denote the phase of phase shifter A and B respectively.

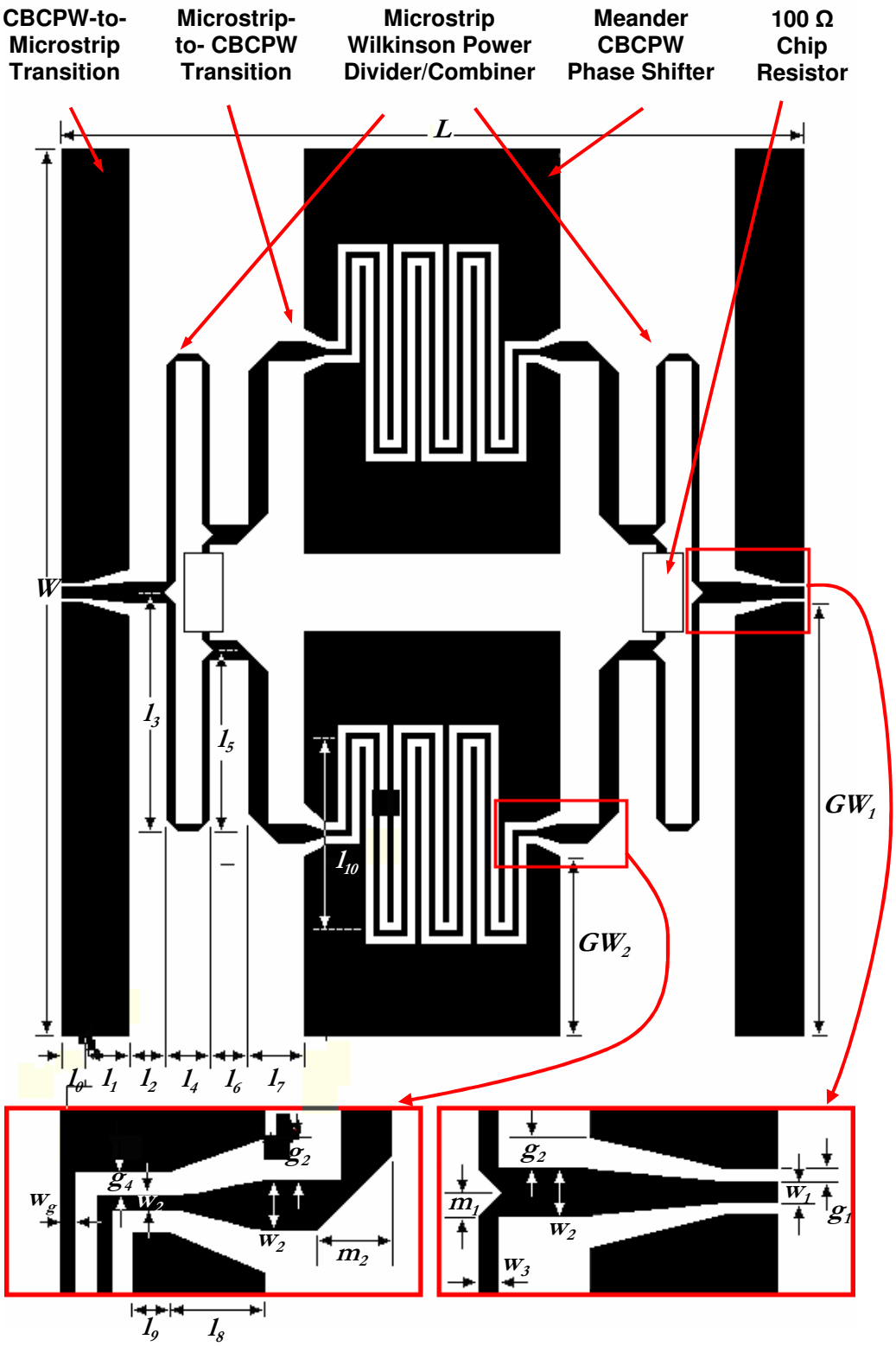

Figure 6.3.1: Generic device layout of the tunable attenuator.

In order to better understand the basic operation of both phase shifters in the tunable attenuator to achieving attentions, Figure 6.3.2 demonstrates the degree of attenuation with varying phase difference between phase shifter A and B ($\varphi_A - \varphi_B$) of an ideal tunable attenuator when conductors and dielectrics are assumed to be perfect and lossless. As seen on the graph, the insertion loss is zero when there was no phase difference between the two phase shifters ($\varphi_A - \varphi_B = 0$). This result was expected as both branch signals were in-phase ($\varphi_A = \varphi_B$) and constructive interference occurred where the output microwave signal was equal to the input microwave signal. As the phase difference magnified, the insertion loss gradually increased and reached the maximum value when ($\varphi_A - \varphi_B = 180°$). At this point, both branch signals were completely out-of-phase and destructive interference occurred with input signals fully suppressed or attenuated, resulting in zero output signals at port 2.

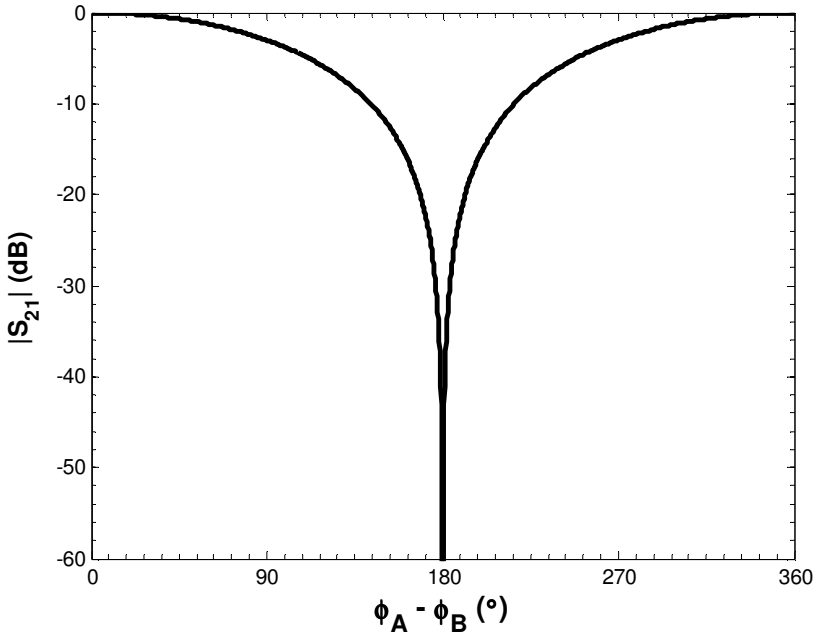

Figure 6.3.2: Ideal attenuation response of the tunable attenuator with respect to the phase difference between phase shifter A and B.

The primary tunable attenuator described in this work was based on BST ferroelectric thin-film whose dielectric constant varies with the application of electric field. While direct experimental measurement for the ferroelectric-based tunable attenuator was not performed, simulated performance results were compared with experimental data from an equivalent attenuator on a Roger/Duroid 6010LM substrate with a constant ε_r of 10.2. The design layout for both the BST- and Duroid-based tunable attenuators were similar, where the signal attenuation was achieved by utilising two tunable phase shifters in parallel. As substrates of dissimilar properties were used, the circuit dimensions for both designs were different. Table 6.3.1 lists the circuit dimensions for both the BST- and Duroid-based tunable attenuator as detailed in Figure 6.3.1. Both attenuators were designed to operate at a centre operating frequency of 6 GHz under room temperature conditions.

6.3.1 Ferroelectric Tunable Attenuator

The ferroelectric tunable attenuator proposed here is based on Barium Strontium Titanate ($Ba_{0.5}Sr_{0.5}TiO_3$ or BST) thin-film of thickness ~0.35 μm on a 500 μm thick of Magnesium Oxide (MgO) substrate, operating at room temperature having a centre frequency of 6 GHz. A silver layer of 300 nm thick was used as the metallisation on both top conductor and the bottom ground plane. Figure 6.3.3 shows the layout of the BST-based tunable attenuator. The circuit has an overall surface area of 8×8 mm.

Two external bias voltages, V_1 and V_2 were applied across the centre strip and the ground planes of both meander CBCPW phase shifters (A and B) of identical dimensions linked by several bond wires. By appropriate control of V_1 and V_2, substantial changes in the dielectric constant of the BST thin-film within the phase shifters were experienced, which subsequently altered the phase of the travelling signal accordingly, thus producing the desired attenuation at the output.

	BST-based Tunable Attenuator (μm)	Duroid-based Tunable Attenuator (μm)
w_1	80	120
g_1	100	60
w_2	400	240
g_2	1700	180
w_3	140	90
w_4	20	60
g_4	40	120
w_g	100	60
m_1	260	150
m_2	640	390
l_0	40	510
l_1	840	990
l_2	300	500
l_3	1900	3090
l_4	600	540
l_5	2780	2340
l_6	400	500
l_7	780	740
l_8	240	480
l_9	140	120
l_{10}	1900	2500
GW_1	3860	5610
GW_2	1220	2310

Table 6.3.1: The circuit dimensions for BST- and Duroid-based tunable attenuator.

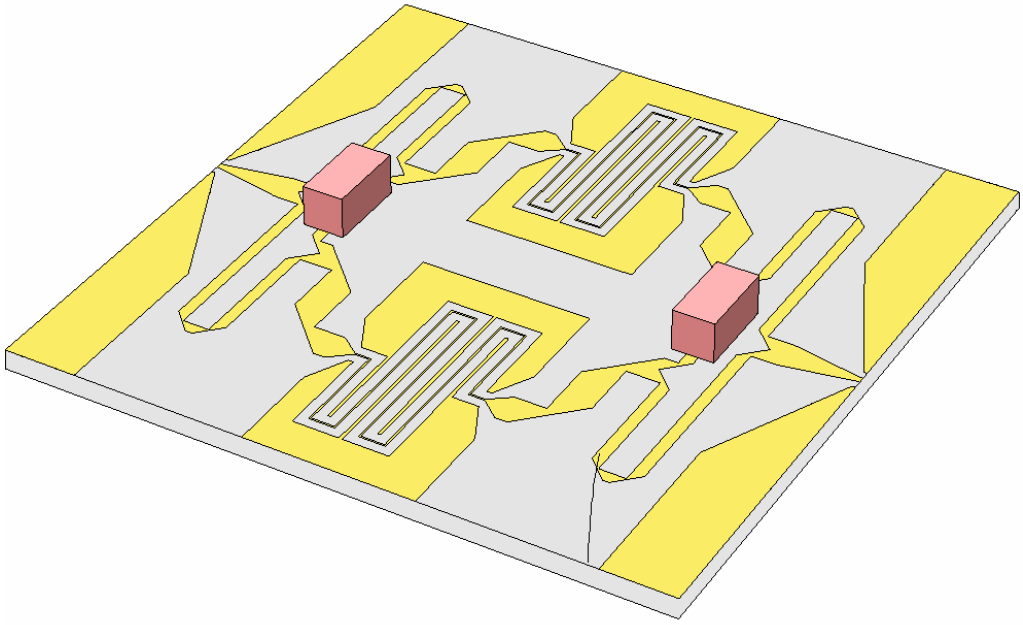

Figure 6.3.3: Layout of the ferroelectric tunable attenuator on BST thin-film and MgO substrate.

Figure 6.3.4 illustrates the Sonnet EM [80] simulated results of the BST-based tunable attenuator for the case where ideal conductors and dielectric materials were assumed (lossless conditions). Here, the bias voltage across phase shifter A (V_1) was modulated between 0 and 100 V whilst a constant zero bias was maintained at phase shifter B. The electric field strength at phase shifter A progressively intensified from 0 $V/\mu m$ to $E \approx 2.5$ $V/\mu m$, causing the dielectric constant of the BST thin-film to vary from ~1800 to ~1000 (as shown previously in Figure 5.2.8), with a corresponding gap width of 40 μm.

Where no bias voltage was applied at both phase shifters i.e. $\varepsilon_A = \varepsilon_B = 1800$ with both branch signals in-phase, the attenuator showed an

expected attenuation or insertion loss of 0 dB at 6 GHz. Conversely, as the bias voltage across phase shifter A rose to 100 *V*, an increase in the insertion loss to 11 dB was obtained. In other words, the attenuator in lossless conditions has demonstrated a controlled change of attenuation of 11 dB with applied bias voltage of 100 *V* across phase shifter A and 0 *V* across phase shifter B. This result was in line with the anticipated phase difference generated between both phase shifters due to the difference in dielectric constant of the BST thin-film in the devices, where ε_A dropped from 1800 to 1000 while ε_B remained at 1800. The return loss of the attenuator was better than 17 dB at all states of bias voltage, which indicates a reasonably good impedance matching at 6 GHz.

It should be noted that the performance of the Wilkinson power splitter and combiner are frequency-dependent. A perfect match can only be obtained at the design frequency where the electrical length of the matching section is $\lambda/4$. Therefore, a deteriorating performance in the attenuator was observed as the frequency moved further away from the centre operating frequency of 6 GHz.

Figure 6.3.5 shows the Sonnet simulated results of the tunable attenuator based on BST thin-film and MgO substrates when losses in the conductors and dielectric materials were taken into consideration (lossy condition). The loss tangent of the BST thin-film was assumed to be 0.12 at 0 *V* and 0.06 at 100 *V*. As a result of these conditions, a relatively high insertion loss of 5.5 dB was obtained at 6 GHz despite the absence of applied bias voltage at the phase shifters and with both branch signals being in-phase. A further increase in insertion loss to 16.2 dB was simulated after the bias voltage across phase shifter A reached 100 *V*. Similar to the lossless conditions, the attenuator with the inclusion of loss factors has demonstrated a controlled change of attenuation of 11 dB. This is expected as the phase change of each phase shifters was independent and unaffected by the loss introduced in the circuit. The simulated return loss was better than 22 dB over a frequency range of 6 to 7 GHz or 14 dB over a frequency range of 5 to 7 GHz.

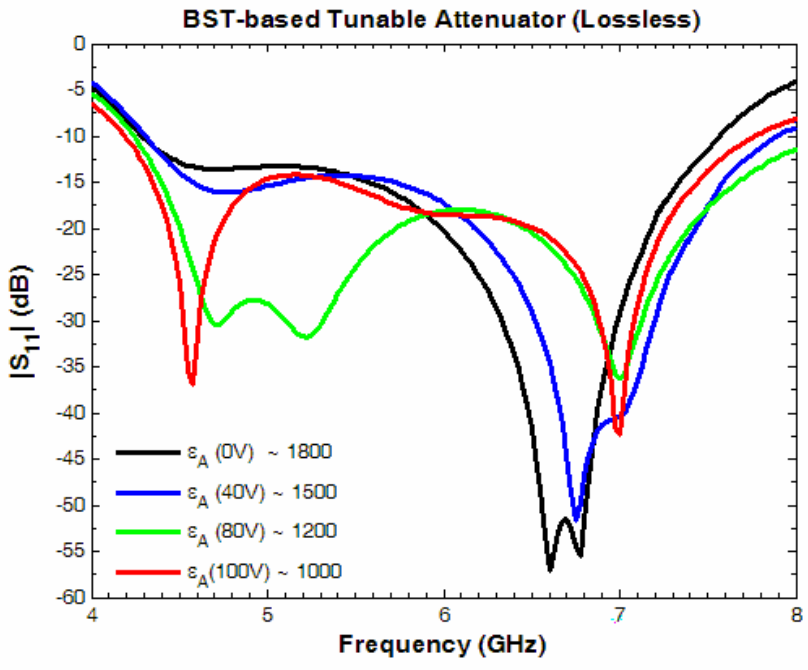

(a)

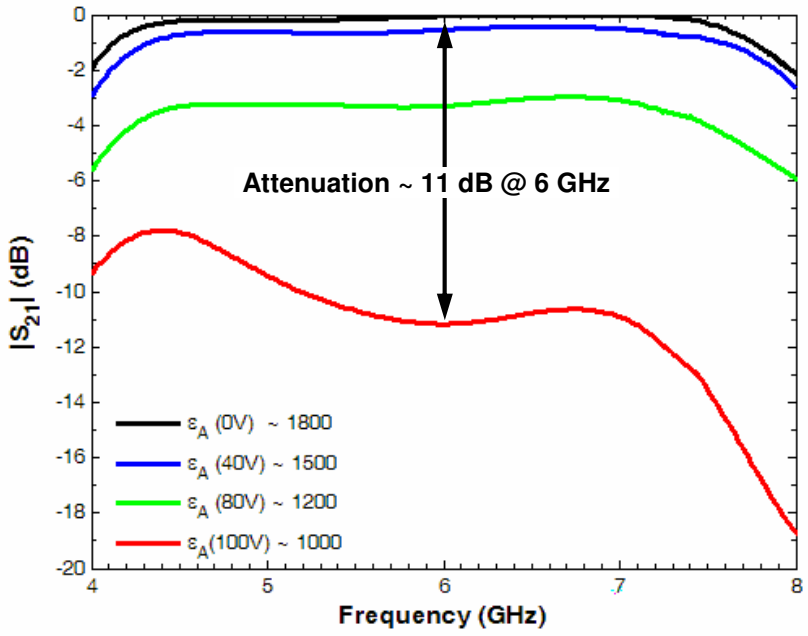

(b)

Figure 6.3.4: Simulated (a) S_{11}, and (b) S_{21} of the BST-based tunable attenuator with various bias voltages on phase shifter A and zero bias on phase shifter B in lossless conditions.

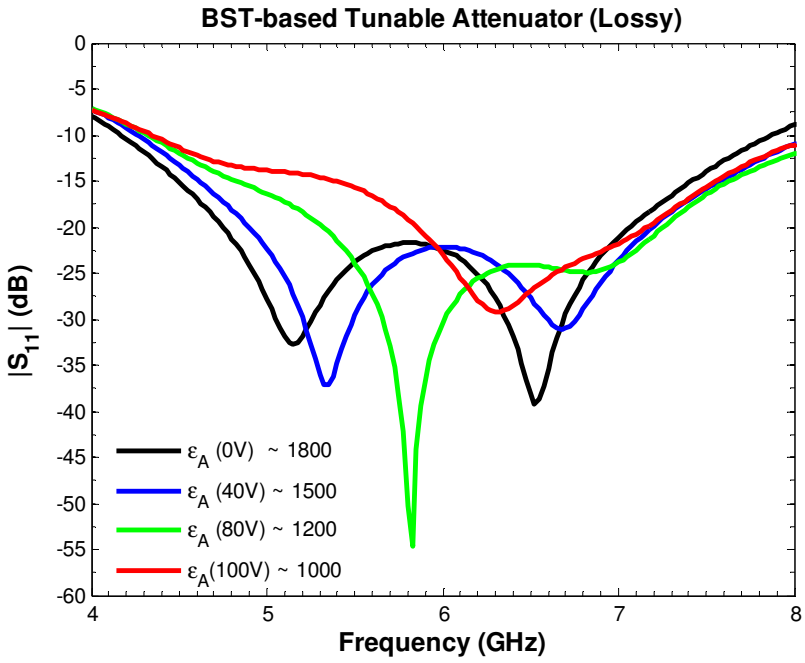

(a)

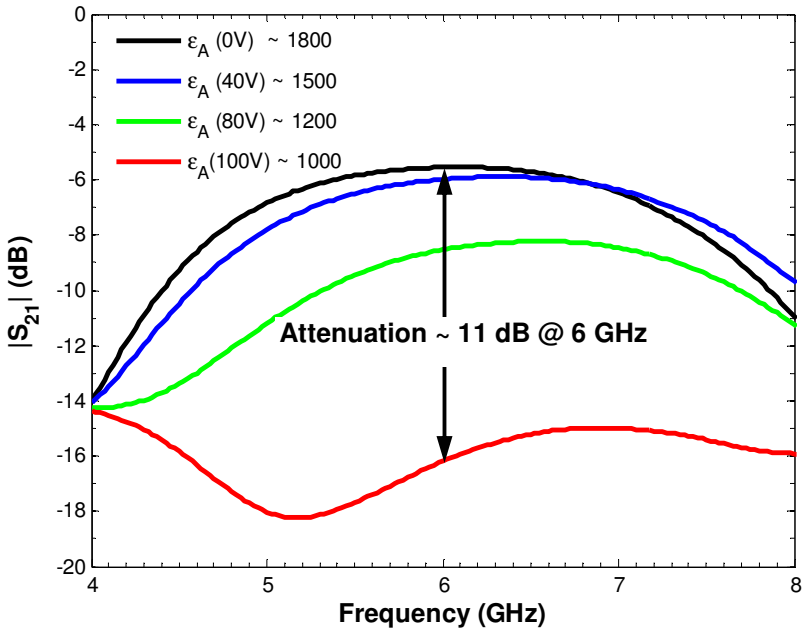

(b)

Figure 6.3.5: Simulated (a) S_{11}, and (b) S_{21} of the BST-based tunable attenuator with various bias voltages on phase shifter A and zero bias on phase shifter B in lossy conditions.

6.3.2 Duroid Tunable Attenuator

A Roger/Duroid 6010LM-based (254 μm thick substrate of dielectric constant 10.2) tunable attenuator of similar design was fabricated and tested in order to verify the Sonnet simulated results and operating principle of the BST-based tunable attenuator. Figure 6.3.6 shows the layout of the Duroid-based tunable attenuator. The realised circuit has an overall size of 11.46 mm × 11.22 mm with a 17 μm thick layer of copper cladding and is shown in Figure 6.3.7. Figure 6.3.8 shows the experimental setup for microwave measurement of the Duroid-based tunable attenuator. This employed a Cascade Microtech Summit 9000 analytical probe station with 250 μm pitch ground-signal-ground (GSG) probes connected to a vector network analyser (Agilent E8361A). All measurements were done at room temperature in the frequency range of 4 to 8 GHz. Calibration to the probe tips was conducted using the LRRM (load-reflect-reflect-match) method with impedance standards formed from gold CPW lines on an alumina substrate to remove external systematic errors, as previously mentioned in Chapter 5.

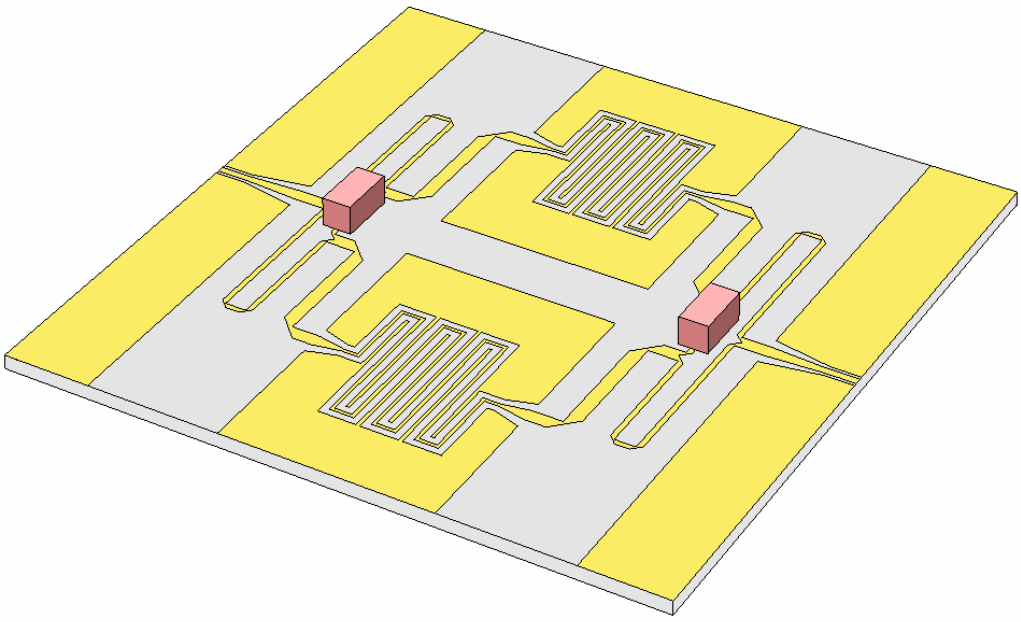

Figure 6.3.6: Layout of the Duroid-based tunable attenuator.

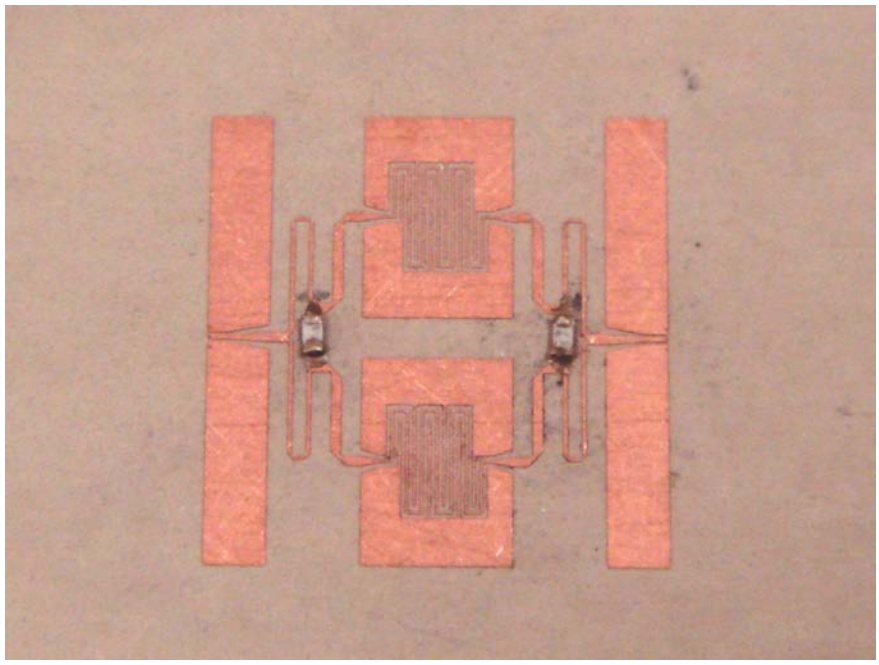

Figure 6.3.7: Photograph of the fabricated Duroid-based tunable attenuator device.

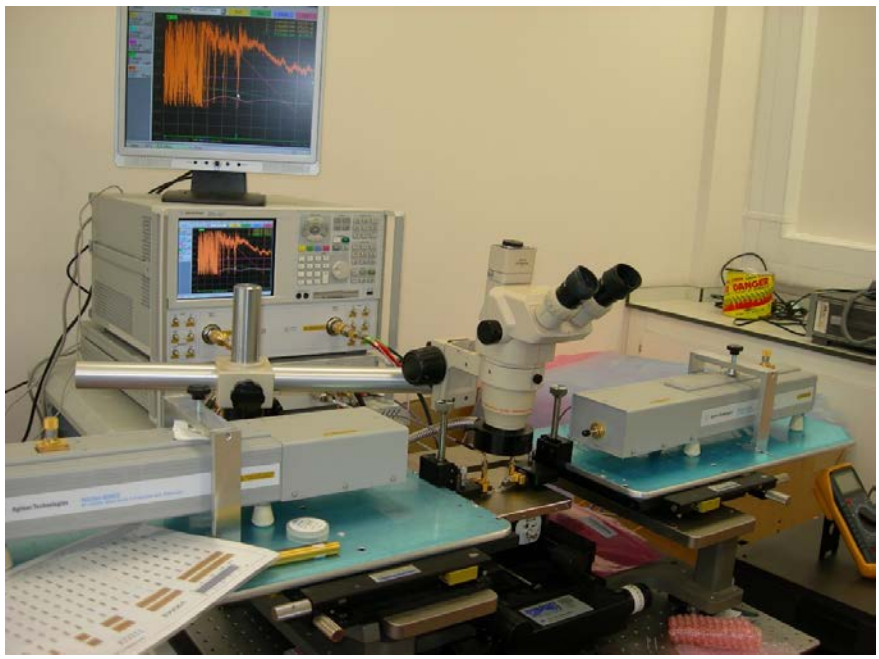

Figure 6.3.8: Attenuator-under-test in a cryogenic probe station connected to Agilent PNA network analyser E8361A.

In order to effect signal attenuation through the circuit, various dielectric materials with different dielectric constant values (as listed in Table 5.3.2) were placed alternately on the surface of phase shifter B to modify the phase of the signal travelling into the phase shifter, as shown in Figure 6.3.9. Figure 6.3.10 shows a weight/metallic screw being placed on the surface of the top-substrate above phase shifter B in an attempt to eliminate any air gaps between the top-substrate and conductor line interface.

Figure 6.3.11 depicts the experimental responses of the tunable attenuator based on Duroid substrate in the case where both phase shifter A and B were loaded with equivalent top-substrates ($\varepsilon_A = \varepsilon_B$). Results were recorded for tests with and without the use of a weight to press the substrates together. In general, use of a weight/metallic screw had negligible effect on attenuator performance. With identical top-substrates positioned on the surface of each phase shifter, an insertion loss of less than 1.4 dB was measured at 5.5 - 6.5 GHz. The frequency shifts in the return and insertion loss with various top-substrates should be noted. Such behaviour was attributed to the variation of load impedance of the splitter/combiner, which is essentially the characteristic impedance of the CBCPW phase shifter. The impedance of the respective phase shifters changed when using top-substrates of different dielectric constants. A minimal return and insertion loss of 44 dB and 0.9 dB was achieved at a frequency of 6 GHz with the MgO top-substrate. This demonstrated that the impedance of both phase shifters loaded with MgO approached 50 **Ω**, where reflections were at its lowest. While zero attenuation was expected with the signals from both output branches in-phase, the imperfect conductor and dielectric materials of the attenuator contributed to the minor losses encountered here.

Figure 6.3.12 shows the measured results of the Duroid-based tunable attenuator when phase shifter A was left bare ($\varepsilon_A = 1$) while phase shifter B was loaded with different ε_r top-substrates ($\varepsilon_A \neq \varepsilon_B$), with and without the use of a weight. Similar to results plotted in Figure 6.3.11, the effect of employing a weight on the top-substrate was negligible. A continuous increase in insertion loss was observed as

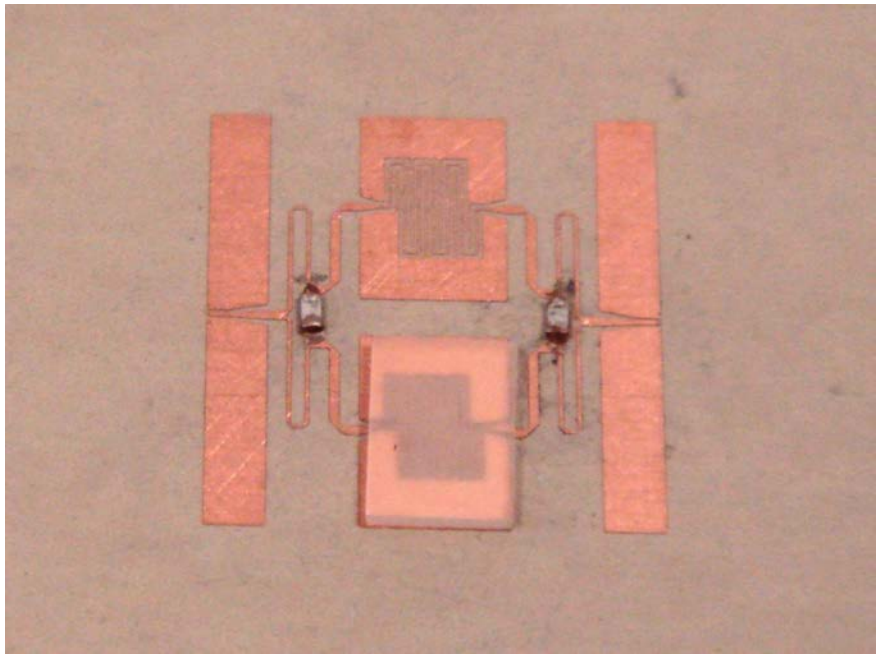

Figure 6.3.9: Photograph of the fabricated Duroid-based tunable attenuator device with phase shifter B loaded with a layer of top-substrate.

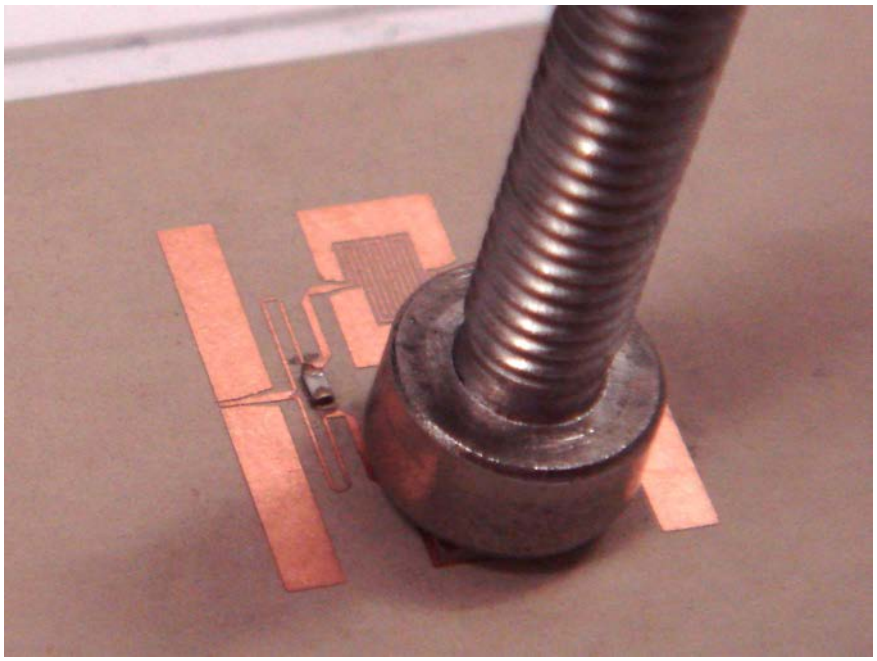

Figure 6.3.10: A weight is placed above the top-substrate on phase shifter B.

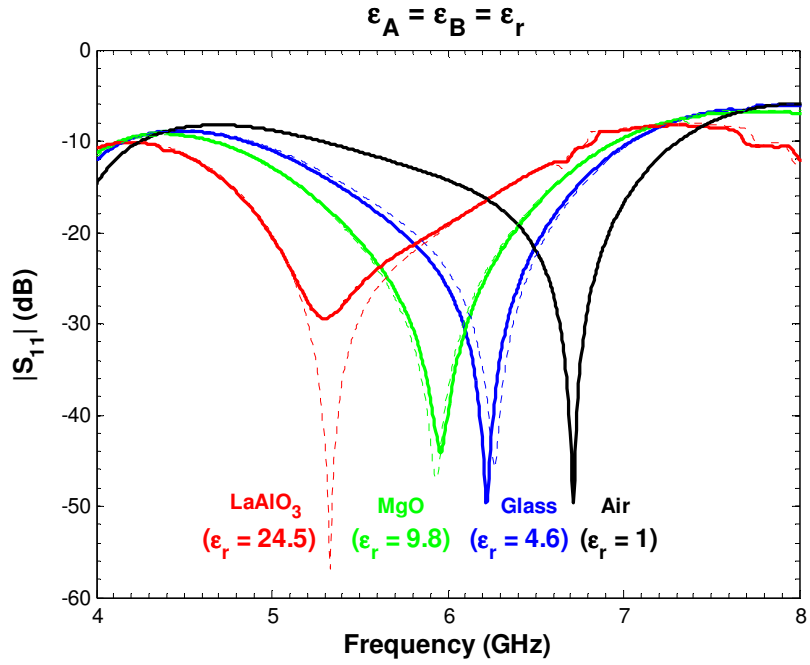

(a)

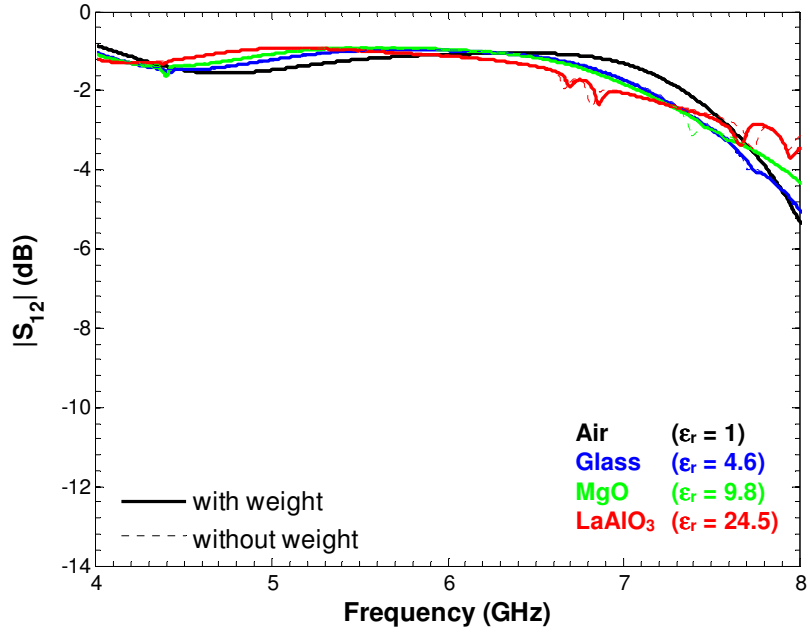

(b)

Figure 6.3.11: Measured (a) S_{11}, and (b) S_{21} of the tunable attenuator based on Duroid substrate with similar top-substrate on both phase shifters (ε_A=ε_B). Solid and doted lines denote with and without the used of a weight, respectively.

successively higher ε_r top-substrates were placed on the surface of phase shifter B. Insertion losses of 1.2 dB, 1.7 dB and 4 dB at 6 GHz were measured when Glass, MgO and $LaAlO_3$ substrates were alternately placed on phase shifter B respectively. This was as expected since the phase difference between both branch signals amplified when ε_r of the top-substrate increased. It should be noted that the performance of the attenuator deteriorated as the frequency was further away from the centre operating frequency of 6 GHz due to the frequency-dependency of the Wilkinson power splitter and combiner. The Duroid-based tunable attenuator therefore has demonstrated a controlled change of attenuation (mimicking a ferroelectric-based device) within the limits of 0.9 dB up to 4 dB and a return loss of better than 17 dB at 6 GHz, when different top-substrates were placed on the surface of the phase shifters.

Figure 6.3.13(a) and (b) shows a comparison between the experimentally measured and Sonnet simulated frequency response of the Duroid-based tunable attenuator for conditions of $\varepsilon_A = \varepsilon_B$ and $\varepsilon_A \neq \varepsilon_B$ respectively. In the Sonnet simulations, an 8 μm thick air gap was simulated between the top-substrate and the conductor interface in the situation when loaded with top-substrate. A small frequency shift was observed between the measured and simulated results. The simulations predict a similar trend to the measured results, with an over-estimation of 0.5 – 0.8 dB in insertion loss and deviation of 3 – 5 dB in terms of return loss. The discrepancy in the measured and simulated responses can be attributed to sesveral aspects, namely (a) the fabrication tolerance where conductors were not perfectly etched i.e. over-, under-etched track, and non-uniform etching profile; (b) simulation limitation in using finite cell size in compensation to simulation time; and (c) the ideal assumption where discrepancy in conductor surface roughness, substrate thickness and dielectric constant distribution across the BST thin-film were neglected. Nonetheless, both experimental and simulation results showed a reasonably good agreement with one another. The 8 μm thick air gap chosen in the simulation has shown to be valid and therefore, has indicated that an air gap was still present between the top-substrate-conductor interfaces disregard with the use of the weight

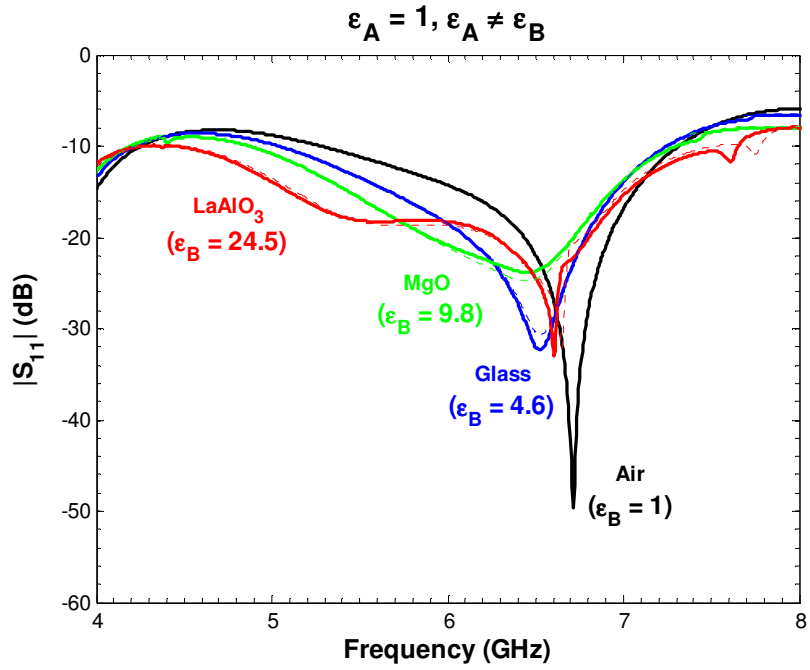

(a)

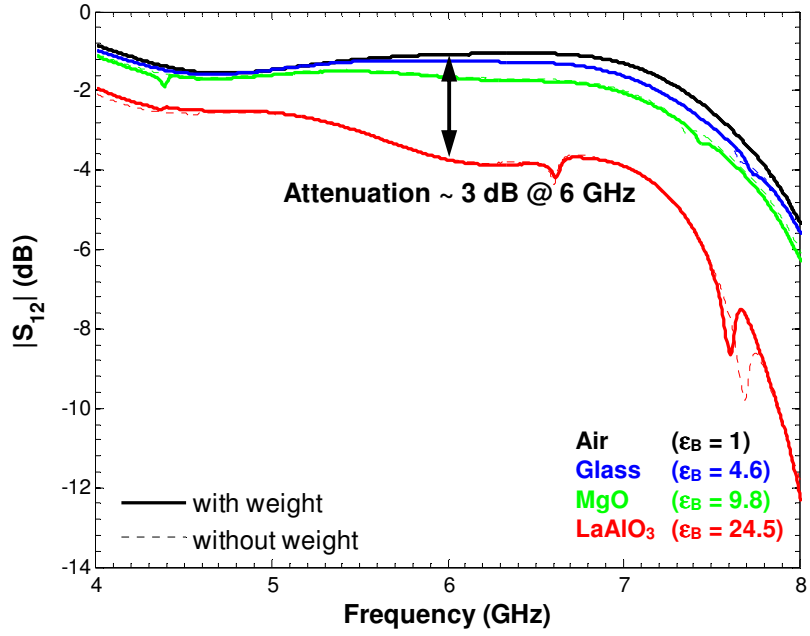

(b)

Figure 6.3.12: Measured (a) S_{11}, and (b) S_{21} of the tunable attenuator based on Duroid substrate with bare phase shifter A and different top-substrate on phase shifter B (ε_A=1 and $\varepsilon_A \neq \varepsilon_B$). Solid and doted lines denote with and without the used of a weight, respectively.

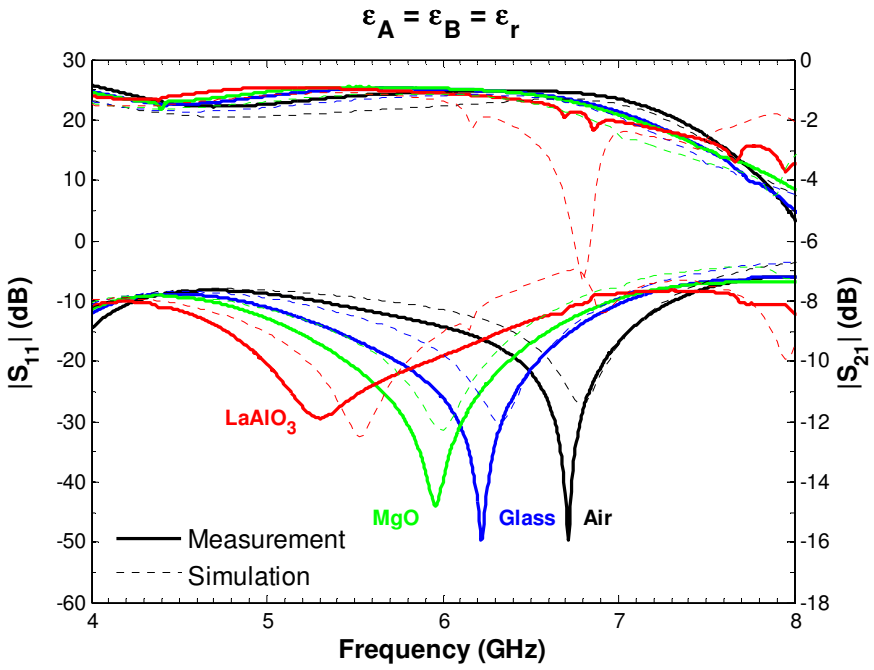

(a)

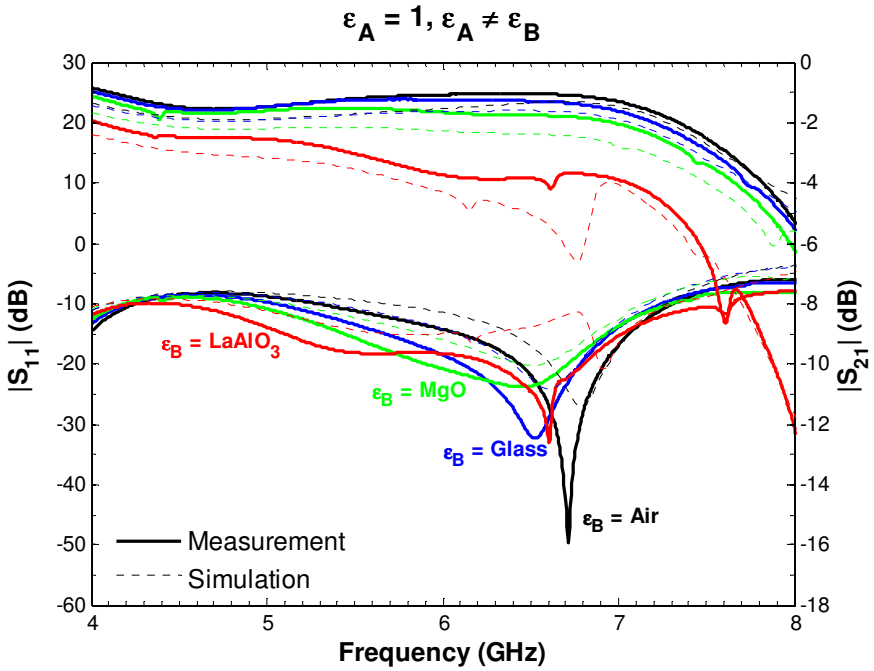

(b)

Figure 6.3.13: Comparison of measured and Sonnet simulated scattering-parameters of the Duroid tunable attenuator with (a) similar top-substrate on both phase shifters (ε_A=ε_B), and with (b) bare phase shifter A and different top-substrate on phase shifter B (ε_A=1 and ε_A≠ε_B).

to press the substrates together. This was probably due to the inherent roughness of the 17-μm-copper surface or the existence of other foreign particles at the interface.

Note that both measured and simulated responses showed an abrupt spurious response at the frequency regime of 6 - 7 GHz when $LaAlO_3$ was loaded onto the surface of the phase shifter. The emergence of such a response was due to the excitation of the unwanted parasitic slotline mode in the meandered CBCPW phase shifter, a result of unequal potentials between the two in-plane grounds alongside of the signal line. As previously mentioned in section 3.6.4, the unbalanced potentials were caused by the difference in path length between the inner slot and the outer slot of the CBCPW meander line [102, 103].

The scattering-parameters of the attenuator obtained from experimental measurement can be utilised to extract the phase of each of the meander CBCPW phase shifters in the attenuator. The phase of both phase shifter A and B (φ_A and φ_B) is related to the attenuator's phase of the transmission coefficient (φ_{S21}) as follows.

$$\varphi_{S21} = \frac{\varphi_A + \varphi_B}{2} \tag{6.3.3}$$

When identical dielectric materials are placed on the surface of both phase shifters, the phase of the phase shifter is simply equal to the attenuator's phase of the transmission coefficient, that is $\varphi_A = \varphi_B = \varphi_{S21}$. The differential phase shift ($\Delta\Phi_{OUT}$) of the attenuator is expressed as:

$$\Delta\Phi_{OUT} = \varphi_{S21}(\varepsilon_{A,B} = 1) - \varphi_{S21}(\varepsilon_{A,B} \neq 1) \tag{6.3.4}$$

where $\varphi_{S21}(\varepsilon_{A,B} = 1)$ and $\varphi_{S21}(\varepsilon_{A,B} \neq 1)$ denote the attenuator's phase of the transmission coefficient with bare and loaded phase shifters respectively.

Figure 6.3.14 shows the measured phase of the transmission coefficient (φ_{S21}) or output phase of the Duroid-based tunable attenuator with various dielectric material combinations on phase shifter A and B, while Figure 6.3.15 plots the

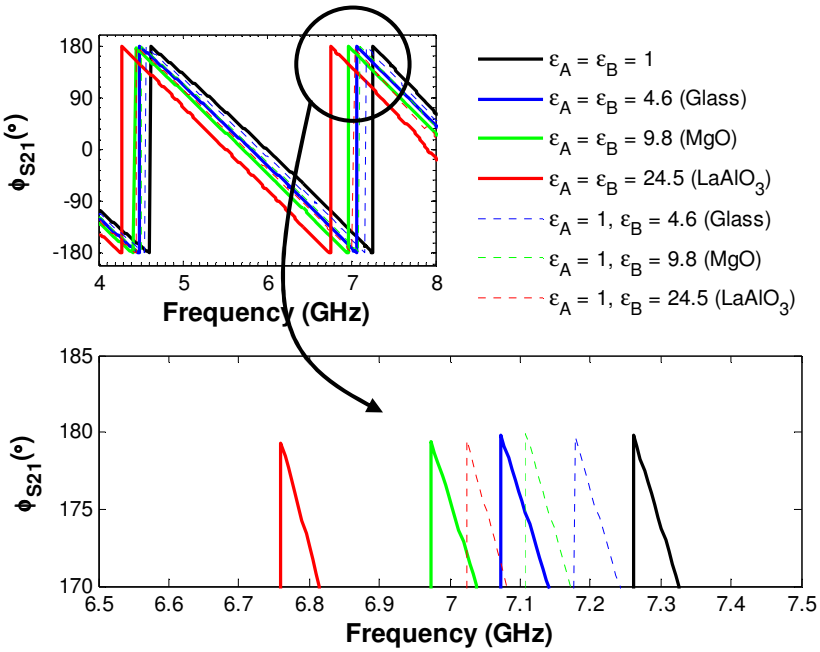

Figure 6.3.14: Measured output phase of the Duroid-based tunable attenuator for various combination of ε_A and ε_B..

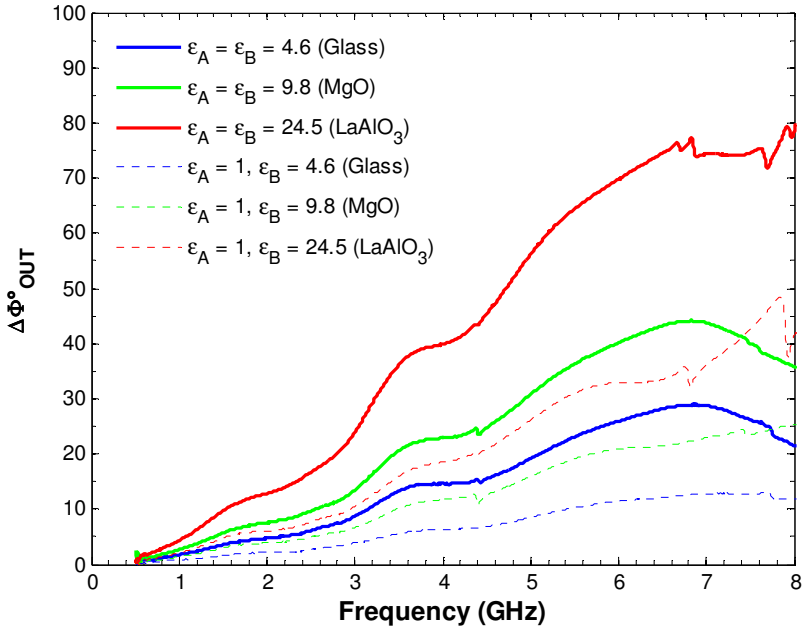

Figure 6.3.15: Differential phase shift of the output signal for various combination of ε_A and ε_B.

corresponding differential phase shift ($\Delta\Phi_{OUT}$) of the attenuator.

As seen from Figure 6.3.15, differential phase shifts of 26°, 40° and 70° were observed at 6 GHz when both phase shifters were equally loaded with Glass, MgO and $LaAlO_3$ respectively. With identical top-substrates and signal modulation characteristics on both phase shifters, the differential phase shift of the attenuator is simply equivalent to the differential phase shift of each phase shifter. The experimental results showed a good agreement with the simulated results of the CBCPW phase shifter discussed in the previous chapter, which was defined with an 8 μm thick air gap between the top-substrate and the conductor. In addition, the measured results were found to be consistent with equation (6.3.3), where the differential phase shift for an attenuator with bare phase shifter A (ε_A = 1) and a selection of different dielectric materials on phase shifter B (giving ε_B = 4.6, 9.8 or 24.5) were halved to approximately 12°, 21° and 33° respectively.

6.4 Conclusions

A novel topology of a tunable attenuator based on BST ferroelectric thin-film has been presented. The BST-based tunable attenuator has enabled a significant reduction in the overall device dimension due to the very high dielectric constant of the ferroelectric material. Other advantages include a much easier fabrication process, as the tunable attenuator is realised into one integrated planar circuit with only a single layer of metallisation required in patterning. But most importantly, the BST-based tunable attenuator proposed in this work is able to provide continuous variation of attenuation under controlled bias voltages. The simulation results of the BST-based tunable attenuator exhibited continuous attenuation in the limits from 5.5 dB up to 16.2 dB with a bias voltage of up to 100 *V*.

The design and operation of the BST-based tunable attenuator was validated with results from a similar design of tunable attenuator based on Duroid substrate tested using on-wafer coplanar probes. At the centre frequency of 6 GHz, the

Duroid-based tunable attenuator showed a controlled attenuation between 0.9 dB and 4 dB when different top-substrates of different dielectric constant was loaded onto the surface of the phase shifters. The measured results were in good agreement with the Sonnet EM simulation and have shown a similar trend of curves as the simulation results of the BST-based tunable attenuator.

Chapter 7

Conclusions

7.1 Summary and Contributions

Ferroelectric materials offer a variety of advantages over other competing technologies, such as ferrites, MEMS, and semiconductors in terms of cost, weight, and size, hence are particularly favoured for applications where rapid, continuous tuning and low power consumption is required. To date, no work on tunable attenuators using ferroelectric materials has ever been reported, as contrary to other extensively studied ferroelectric-based tunable microwave devices and components, namely tunable resonators, filters, and phase shifters.

In response to these motivations, this research has demonstrated the developments of a tunable attenuator device based on Barium Strontium Titanate ($Ba_{0.5}Sr_{0.5}TiO_3$ or BST) ferroelectric thin-film. The BST-based tunable attenuator in this work allows a significant reduction in size and weight, and most importantly, the use of ferroelectric material enables continuous variation of attenuation under controlled bias voltages. In addition, a much easier fabrication process is involved as the device is realised into one integrated planar circuit with only a single layer of

metallisation required for patterning. The topology of the tunable attenuator utilised the non-linear dielectric constant of the BST ferroelectric thin-film and employed the principle of constructive and destructive interference by integrating two tunable ferroelectric-based phase shifters in parallel to produce amplitude shifting or attenuation of the signal under appropriate controlled bias voltage.

7.1.1 Finite Difference Method Computation

A significant portion of this research was focused on the parameter computations, namely the effective dielectric constant (ε_{eff}) and the characteristic impedance (Z_c), of ferroelectric-based transmission lines, The work on how the finite difference method (FDM), a computational technique, was modified to suit the evaluation of the cross-sectional field distribution of a ferroelectric-based transmission line has been presented in Chapter 4. The modified FDM was employed for determining the ε_{eff} and Z_c of ferroelectric-based structures where the spatial variation of dielectric constant was taken into consideration with assumption of isotropic and homogenous materials/substrates used ($\varepsilon_x = \varepsilon_y = \varepsilon_r$).

Extremely good agreement between FDM calculation, existing closed-form analytical models and Sonnet simulation results was observed when utilising a fixed value of ferroelectric dielectric constant. When allowing for spatial variation of the ferroelectric dielectric constant, the FDM calculation demonstrated the same trend as similar work reported by Sung *et al.* [119] where the finite element method was employed. The trend showed a generally lower Z_c and higher ε_{eff} as compared to that of the assumed approximate constant value with a small percentage difference of approximately ~1 to 6% depending on the dimensions of the transmission lines. The small difference in the results indicates that the closed-form conformal mapping technique of assuming a fixed ferroelectric dielectric constant is valid for most practical cases. Nonetheless, the demonstrated methodology for determining accurate values of circuit impedance is a useful tool in enhancing the design and performance of ferroelectric based devices. A paper relating to this computational

technique has been published [33] and can be found in Appendix C.

7.1.2 Dielectric Properties of BST Thin-film

Prior to the integration of ferroelectric materials in the tunable attenuator circuit design, precise dielectric properties of BST thin-film were acquired. As outlined in Chapter 5, the fabrication and experimental measurements of the CPW and tapered CPW transmission lines on BST thin-film and MgO substrates have been performed. Characterisation of the BST dielectric properties using on-wafer probing was demonstrated at room temperature. The real part value of the BST dielectric constant ε'_{BST} was found to be ~1800 at 0 $V/\mu m$ and ~940 at 3.13 $V/\mu m$, achieving a high relative tunability n_r of approximately 48%. In parallel with the characterisation of the BST thin-film, the CPW and tapered CPW transmission lines (which at the same time served as phase shifters of delay-line type) obtained phase shifts of 40° and 105°, with insertion loss better than 5.4 dB and 10.6 dB, resulting in figure-of-merit of 9.5°/dB and 14.4°/dB at 20 GHz respectively.

It is difficult to accurately extract the losses or loss tangent due to the BST thin-film (tan δ_{BST}), another crucial dielectric property of BST thin-film, from the measured total loss of the device, which includes the loss attributed to the silver conductor. By estimating the tan δ_{BST} and using the dielectric constant values of the BST thin-film obtained from experimental characterisation, the performance of the CPW and tapered CPW transmission lines/phase shifters were modelled using Sonnet simulation software to reproduce the raw experimental data, i.e. the scattering-parameters. A reasonably close agreement between the simulation results using estimated tan δ_{BST} values and the experimental data was observed, particularly at lower frequencies and bias voltages under 40 V. This would suggest a good estimation of the loss tangent and extraction of the dielectric constant of the BST thin-film. The tan δ_{BST} values was estimated to be 0.12 at zero electric field (ε_{BST} ~ 1800) and decreased to 0.06 at 3.13 $V/\mu m$ (ε_{BST} ~ 940).

As a result of the very high loss tangent of the BST thin-film (tan δ_{BST} = 0.12), the loss attributed to the silver metallisation (or conductor loss α_c) is comparable to the loss attributed to the BST thin-film (or dielectric loss α_d) at frequencies below 10 GHz, which is shown in Figure 3.6.1.

The experimental work of the CPW and tapered CPW phase shifters was carried out as a preliminary step towards using BST thin-film for designing CBCPW phase shifters, which are key components in the tunable attenuator described in this research. The design and the associated simulated response of CBCPW phase shifters on both BST/MgO and Duroid substrates was investigated with the effect of increased air gap layer between the top-substrate and conductor interface found to significantly reduce the differential phase shift.

7.1.3 Tunable Attenuator

Chapter 6 presented the tunable attenuator device which employed CBCPW-to-microstrip transitions, microstrip Wilkinson power splitter/combiner and two meandered CBCPW phase shifters in parallel to achieve a controlled attenuation. The proposed tunable attenuator was based on BST ferroelectric thin-film on an MgO substrate. The results from simulations of the BST-based tunable attenuator predicted a continuous attenuation (or controlled change of the insertion loss) in the limits from 5.5 dB up to 16.2 dB at 6 GHz with bias voltage up to 100 V or applied electric field up to 2.5 $V/\mu m$. The results were found to be promising when compared to a similar piece of work previously detailed in [32], where the reported tunable attenuator was realised using semiconductor tunable varactors in a cascade manner in order to achieve controlled attenuation.

In order to verify the simulation results as well as the validity of the operating principle of the BST-based tunable attenuator, a similar design of tunable attenuator based on Duroid substrate was successfully designed and tested using on-wafer coplanar probes at room temperature. When employing a centre frequency of 6

GHz, the Duroid-based tunable attenuator showed a controlled attenuation in the limits from 0.9 dB up to 4 dB with different dielectric constant of top-substrate loaded onto the surface of the phase shifters. The measured results were in good agreement with the full-wave simulation and showed a similar trend of curves as with the simulation results of the BST-based tunable attenuator.

The main contributions from this research can be summarised as,

- Determination of key transmission line parameters (effective dielectric constant ε_{eff} and the characteristic impedance Z_o) relative to practical line geometries/dimensions using the finite difference method.

- Derivation of a modified finite difference equation to account for the non-linear behaviour of ferroelectric-based transmission lines.

- Design and operational simulation of a tunable attenuator on a ferroelectric thin-film coated substrate that allowed for continuous variation of signal attenuation under controlled bias voltages. Results were benchmarked against an equivalent design fabricated using Duroid substrate.

7.2 Suggestions for Future Work

Novel design concepts for a tunable attenuator integrating BST thin-film and MgO substrate have been proposed as a result of this research. However, the operating principle of the innovative BST-based tunable attenuator has only been demonstrated in this work using Sonnet simulations and verified through experimental measurements of a similar tunable attenuator design based on Duroid substrate. While the approach employed was valid considering the scope and technical constraints of the current project, it is nonetheless recommended that future testing be undertaken on an attenuator fabricated with BST substrate. The following work is also envisaged in order to further develop the ideas presented in this thesis:

- Optimisation of the tunable attenuator for wider-band operation and improved degree of controlled attenuation. The tunable attenuator introduced in this research was designed to operate at a centre operating frequency of 6 GHz, with acceptable level of return and insertion loss over a frequency range of 5 to 7 GHz. Such band-limiting behaviour is due to the quarter-wavelength transmission sections of the Wilkinson power divider/combiner used in the circuits. For wider-band operation, additional transformer sections and isolation resistors would be required. Hence, further design or circuit optimisation is needed with a trade-off between band operation and physical size limitation, as well as consideration of loss factors.

- Investigation of tunable attenuators using thicker or low-resistivity metallisation, such as high temperature superconductors (HTS) to improve insertion loss performance. As a significant portion of losses experienced in the tunable attenuator were attributed to conductor loss of the metallisation used in the circuit, results of incorporating thicker metallisation (typically several orders thickness of the skin depths) or the use of HTS is worthy of study.

- Integration of BST varactors in the tunable attenuator circuit to achieve controlled attenuation. Use of loaded-line phase shifters with a BST varactor instead of conventional delay-line type phase shifters can drastically reduce the dielectric loss of BST thin-film and hence, improve the overall insertion loss performance of the tunable attenuator.

- Optimisation of phase shifters which would enable maximum phase shift with relatively low bias voltage.

- Investigation of simplified, via-less CBCPW-to-microstrip transitions on thicker substrates with improved insertion loss performance and reduced parasitic modes.

Appendix A :
Approximations for Elliptic Integrals Ratio

This section presents the approximations for elliptic integrals ratio of the first kind used in the compact closed-form analytical expressions as mentioned in Chapter 3 in finding the effective dielectric constant ε_{eff} and the characteristic impedance Z_c of coplanar lines, i.e. multilayer coplanar waveguide (CPW), conductor-backed coplanar waveguide (CBCPW) and dielectric-loaded CBCPW.

An efficient and fast converging ratio for the complete elliptic integrals of the first kind $K(k)/K'(k) = K(k)/K(k')$ can be evaluated to an accuracy of better than 10^{-8} using the following expression [84]. Assuming $m = k^2$, $m_1 = 1 - k^2$:

for $0 < k \le \frac{1}{\sqrt{2}}$,

$$\frac{K(k)}{K(k')} = -\pi \left\{ \ln\left[\frac{m}{16} + 8\left(\frac{m}{16}\right)^2 + 84\left(\frac{m}{16}\right)^3 + 992\left(\frac{m}{16}\right)^4 + \ldots \right] \right\}^{-1} \tag{A.1}$$

and for $\frac{1}{\sqrt{2}} \le k < 1$,

$$\frac{K(k)}{K(k')} = -\frac{1}{\pi} \left\{ \ln\left[\frac{m_1}{16} + 8\left(\frac{m_1}{16}\right)^2 + 84\left(\frac{m_1}{16}\right)^3 + 992\left(\frac{m_1}{16}\right)^4 + \ldots \right] \right\} \tag{A.2}$$

Appendix B :
Incremental-Inductance Method

B.1 Introduction

This section presents the derivation of the analytical expression for the conductor loss of conductor-backed coplanar waveguide (CBCPW) based on incremental-inductance method, as discussed in Section 3.6.1.

The incremental-inductance method, an alternative technique for derivation of conductor loss, was first published in 1942 by Wheeler [138] and further developed by Pucel [96]. In Wheeler's method [138], the series surface resistance per unit length R_s caused by the skin effect is expressed in terms of the inductance produced by the magnetic field within the conductors. The formulation is based on the fact that the surface impedance Z_s of a conductor,

$$Z_s = R_s + jX \tag{B.3}$$

has a real part R_s which is equals to its imaginary part X. That is,

$$R_s = X = \omega L_i \tag{B.4}$$

where L_i is the internal inductance per unit length caused by a thin layer of current flow due to the skin effect. According to the 'incremental-inductance rule', L_i can be derived as the increase in the external inductance per unit length L due to the incremental recessions of all conductive walls by half of the skin depth [96]. An assumption underlying this rule is that the radius of the curvatures and the thickness of the conductors exposed to the electromagnetic field are larger than the skin depth, preferably several skin depths. The internal inductance per unit length L_i and series

surface resistance per unit length R can be expressed as [96]:

$$L_i = \sum_m \frac{\mu_m}{\mu_0} \frac{\partial L}{\partial n_m} \frac{\delta_m}{2}$$
$$R_s = \frac{1}{\mu_0} \sum_m R_{s,m} \frac{\partial L}{\partial n_m} \tag{B.5}$$

where $\partial L/\partial n_m$ denotes the derivative of L with respect to incremental recession of wall m, n_m is the normal direction to wall m, and $R_{s,m} = \omega\mu_m\delta_m/2$ is the surface resistance of the conductor wall m. The external inductance L can be expressed in terms of the characteristic impedance of the transmission line with the dielectric replaced by air Z_0^a and is given as [77]:

$$L = \frac{Z_0^a}{c_0} \tag{B.6}$$

where c_0 is the velocity of the electromagnetic wave in free space.

The attenuation constant due to conductor or ohmic loss is defined as [77, 96]:

$$\alpha_c = \frac{P_c}{2P(z)} = \frac{I^2 R_s}{2I^2 Z_c} = \frac{1}{2\mu_0 Z_c} \sum_m R_{s,m} \frac{\partial L}{\partial n_m} \tag{B.7}$$

P_c, $P(z)$ and Z_c denote the average power loss in conductors, transmitted power in z-direction (along the direction of propagation parallel to the strip conductor) and the characteristic impedance respectively.

B.2 Conductor Loss of CBCPW

Figure B.1 illustrates the recessions of the conductor surfaces in CBCPW for loss calculation using incremental-inductance method [98], where

$\partial w = -2\partial n$ (recession of either edge of the strip)
$\partial g = 2\partial n$ (recession of one edge of the strip and one of the in-plane grounds)
$\partial t = -2\partial n$ (recession of top and bottom of strip conductors)
$\partial h = \partial n$ (recession of bottom of strip conductors)
$\partial h = \partial n$ (recession of conductor backing)

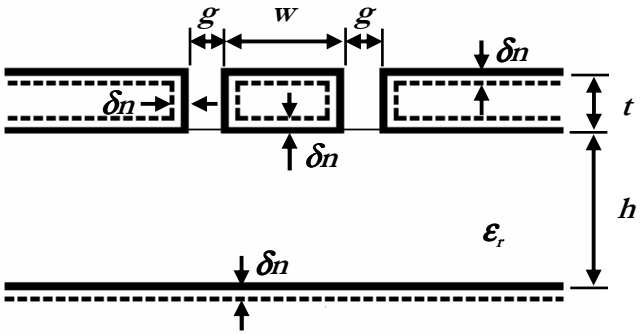

Figure B.1: Recession of the conductors of CBCPW for loss calculation using incremental-inductance method [98].

As quoted from [96] when dealing with the ground of the microstrip, it is "on somewhat uncertain ground, however, in deciding whether the recession of the bottom surface of the strip conductor can be counted towards a recession in *t* as well as an extension of *h*". It is assumed here for the coplanar waveguide as for microstrip in [96], by counting towards as a recession of *t*, a larger value of α_c was obtained and has seemed to agree better with the measured results.

The attenuation of CBCPW due by conductor loss as adopted from [98] can be expressed as:

$$\alpha_c^{CBCPW} = \frac{8.68}{\mu_0 c_0 Z_c^{CBCPW}} \left[R_s^s \left(\frac{\partial Z_c^a}{\partial g} - \frac{\partial Z_c^a}{\partial w} - \frac{\partial Z_c^a}{\partial t} + \frac{1}{2}\frac{\partial Z_c^a}{\partial h} \right) + R_s^G \left(\frac{1}{2}\frac{\partial Z_c^a}{\partial h} \right) \right] \quad \text{(B.8)}$$

where R_s^s and R_s^G are the surface resistances on the strip and the conductor-backing. Assume $R_s^s = R_s^G$.

B.2.1 Narrow coplanar line

For CBCPW with substrate thickness h much larger than the centre strip width w and gap width g, ($h >> w$ and g), the conductor-backing has less effect on the fringe field of the coplanar conductors [98]. Therefore, the similar correction can be adopted for CBCPW as for the conventional CPW in [77]. The effective strip w_e and gap g_e widths are defined as:

$$w_e = w + 1.25\frac{t}{\pi}\left[1 + \ln\left(\frac{4\pi w}{t}\right)\right] \quad ; \quad g_e = g - 1.25\frac{t}{\pi}\left[1 + \ln\left(\frac{4\pi w}{t}\right)\right] \tag{B.9}$$

Let

$$k_1 = w_e/(w_e + 2g_e) \quad ; \quad k_2 = A/B \tag{B.10}$$

where

$$A = \tanh\left(\frac{\pi w_e}{4h}\right) \quad ; \quad B = \tanh\left[\frac{\pi(w_e + 2g_e)}{4h}\right] \tag{B.11}$$

and

$$X_{i=1,2} = \begin{cases} \left[\dfrac{K(k_i)}{K\left(\sqrt{1-k_i^2}\right)}\right]^2 \dfrac{k_i}{\left(1-\sqrt{1-k_i^2}\right)\left(1-k_i^2\right)^{0.75}} & 0 \le k_i \le 0.707 \\ \dfrac{1}{(1-k_i)\sqrt{k_i}} & 0.707 < k_i \le 1 \end{cases} \tag{B.12}$$

$$Y_1 = \frac{2(w_e + g_e)}{(w_e + 2g_e)^2}\left[1 + \frac{1.25t}{\pi w} + \frac{1.25}{\pi}\ln\left(\frac{4\pi w}{t}\right)\right] \tag{B.13}$$

$$Y_2 = \frac{(B-A)(1+AB)+2A}{B^2}\left[\frac{\pi}{4h}+\frac{1.25t}{4hw}+\frac{1.25}{4h}\ln\left(\frac{4\pi w}{t}\right)\right]... \\ -\frac{A(1-B^2)}{B^2}\frac{\pi g_e}{2h^2}+\frac{(B-A)(1+AB)}{B^2}\frac{\pi w_e}{4h^2} \tag{B.14}$$

The attenuation of CBCPW due to conductor loss can be expressed as:

$$\alpha_c^{CBCPW} = \frac{8.68}{60\pi^2\mu_0 c_0} R_s \varepsilon_{eff} Z_c^{CBCPW}\left(X_1 Y_1 + X_2 Y_2\right) \tag{B.15}$$

When the substrate is sufficiently thick, this attenuation approaches the one as for a CPW as expected.

B.2.2 Wide coplanar line

When w is comparable or larger than h, the fringe field will be greatly affected by the presence of the conductor-baking. In such a case, the aforementioned correction that only depends on w and t may not be valid. Instead, a correction depending on h and t can be used, which was mentioned in [98, 122].

$$\Delta' = \frac{1.25t}{\pi}\left[1+\ln\left(\frac{2h}{r}\right)\right] \quad ; \quad w_e = w+\Delta' \quad ; \quad g_e = g-\Delta' \quad ; \quad h_e = h \tag{B.16}$$

Let

$$k_1 = w_e/(w_e+2g_e) \quad ; \quad k_2 = A/B \tag{B.17}$$

where

$$A = \tanh\left(\frac{\pi w_e}{4h_e}\right) \quad ; \quad B = \tanh\left[\frac{\pi(w_e+2g_e)}{4h_e}\right] \tag{B.18}$$

and

$$X_{i=1,2}=\begin{cases}\left[\dfrac{K(k_i)}{K\left(\sqrt{1-k_i^{\,2}}\right)}\right]^2\dfrac{k_i}{\left(1-\sqrt{1-k_i^{\,2}}\right)\left(1-k_i^{\,2}\right)^{0.75}} & 0\le k_i\le 0.707\\ \dfrac{1}{(1-k_i)\sqrt{k_i}} & 0.707<k_i\le 1\end{cases}$$

$$Y_1=\frac{2(w_e+g_e)}{(w_e+2g_e)^2}\left[1-\frac{1.25t}{\pi h}+\frac{1.25}{\pi}\ln\left(\frac{2h}{t}\right)\right] \tag{B.19}$$

$$Y_2=\frac{(B-A)(1+AB)}{B^2}\left[\frac{\pi}{4h}-\frac{\pi}{4h^2}\left(\frac{1.25t}{\pi}-w_e\right)+\frac{1.25}{4h}\ln\left(\frac{2h}{t}\right)\right]\cdots$$
$$+\frac{A}{B^2}\left[\frac{\pi}{2h}+\frac{1.25}{2h}\ln\left(\frac{2h}{t}\right)-\frac{\pi}{2h^2}\left(\frac{1.25t}{\pi}+\left(1-B^2\right)g_e\right)\right]$$

The conductor loss in this case is similar as equation (B.15), with the use of X_1, Y_1, X_2 and Y_2 from equation (B.19). The problem of this correction (Δ') is its divergence with increasing substrate thickness h. This also results in a divergent attenuation, which is physically unreasonable. So the valid range of this correction is restricted. It is believed that this correction is only usable when h is comparable or smaller than w. In addition, according to [74], this correction overestimates the characteristic impedance.

Appendix C :

"Computation of Parameters of a Ferroelectric-filled Microstrip by Finite Difference Method"

- IET Microwaves, Antennas and Propagation

Computation of parameters of a ferroelectric-filled microstrip by finite difference method

L.C. Cheng and M.J. Lancaster

Abstract: The permittivity of ferroelectric materials undergoes a substantial change with the application of an electric field. A new variation on the finite difference method to calculate electric fields in ferroelectric structures is presented. As an example, it is shown that how microstrip line parameters such as the effective permittivity and the characteristic impedance are computed when the dielectric is replaced with the ferroelectric. The derivation of the finite difference equations for ferroelectric materials is presented and the results are verified.

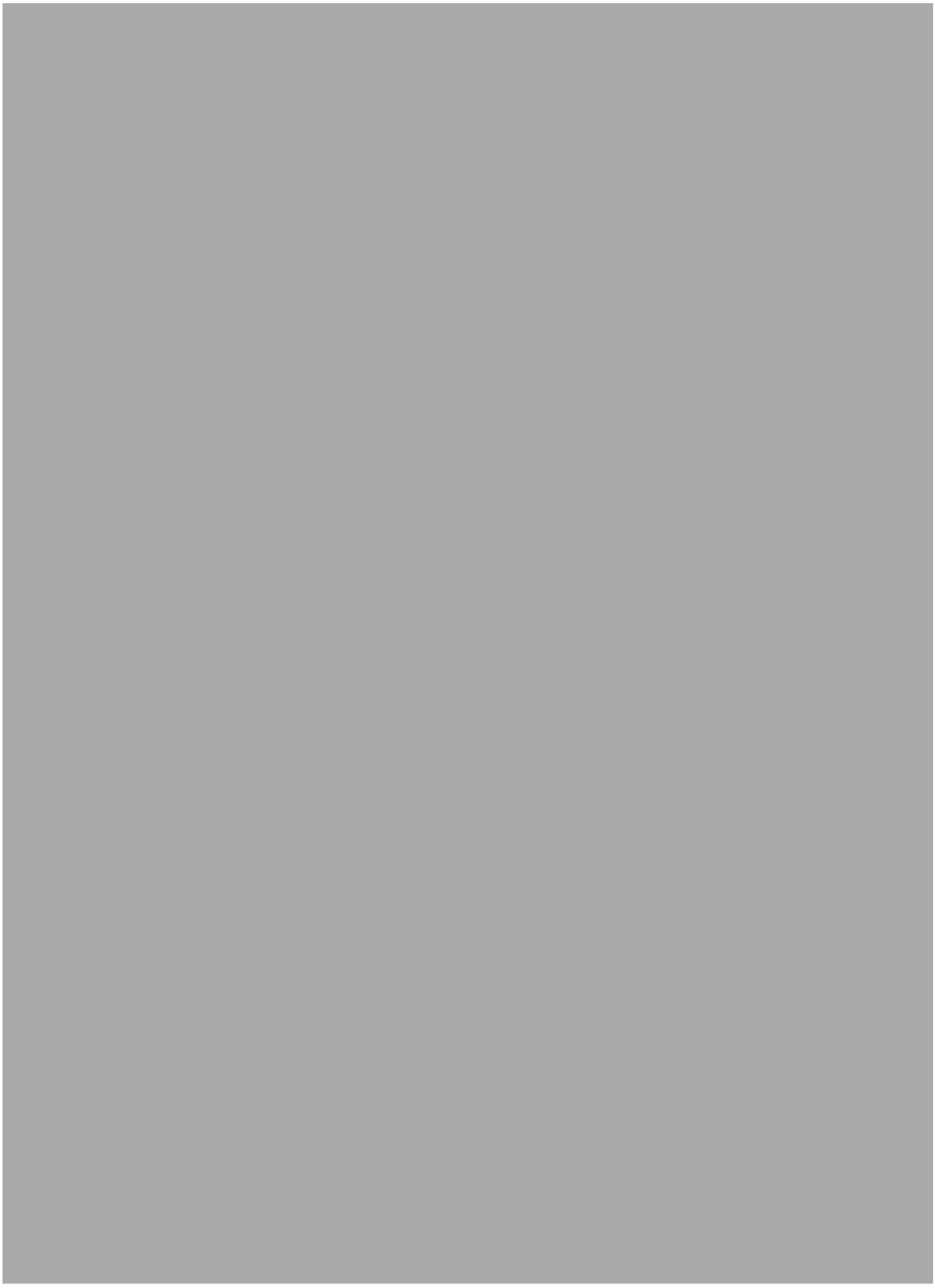

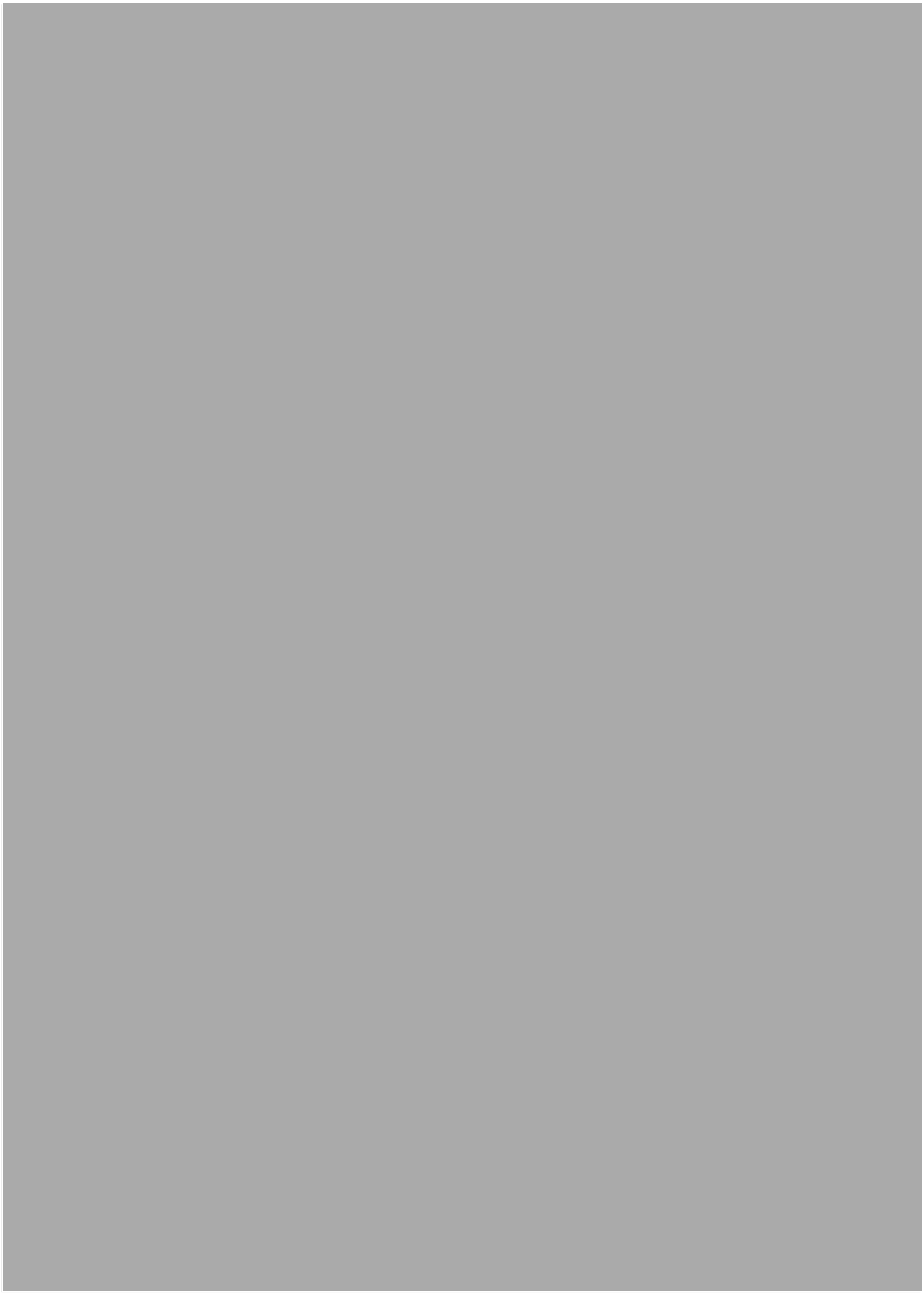

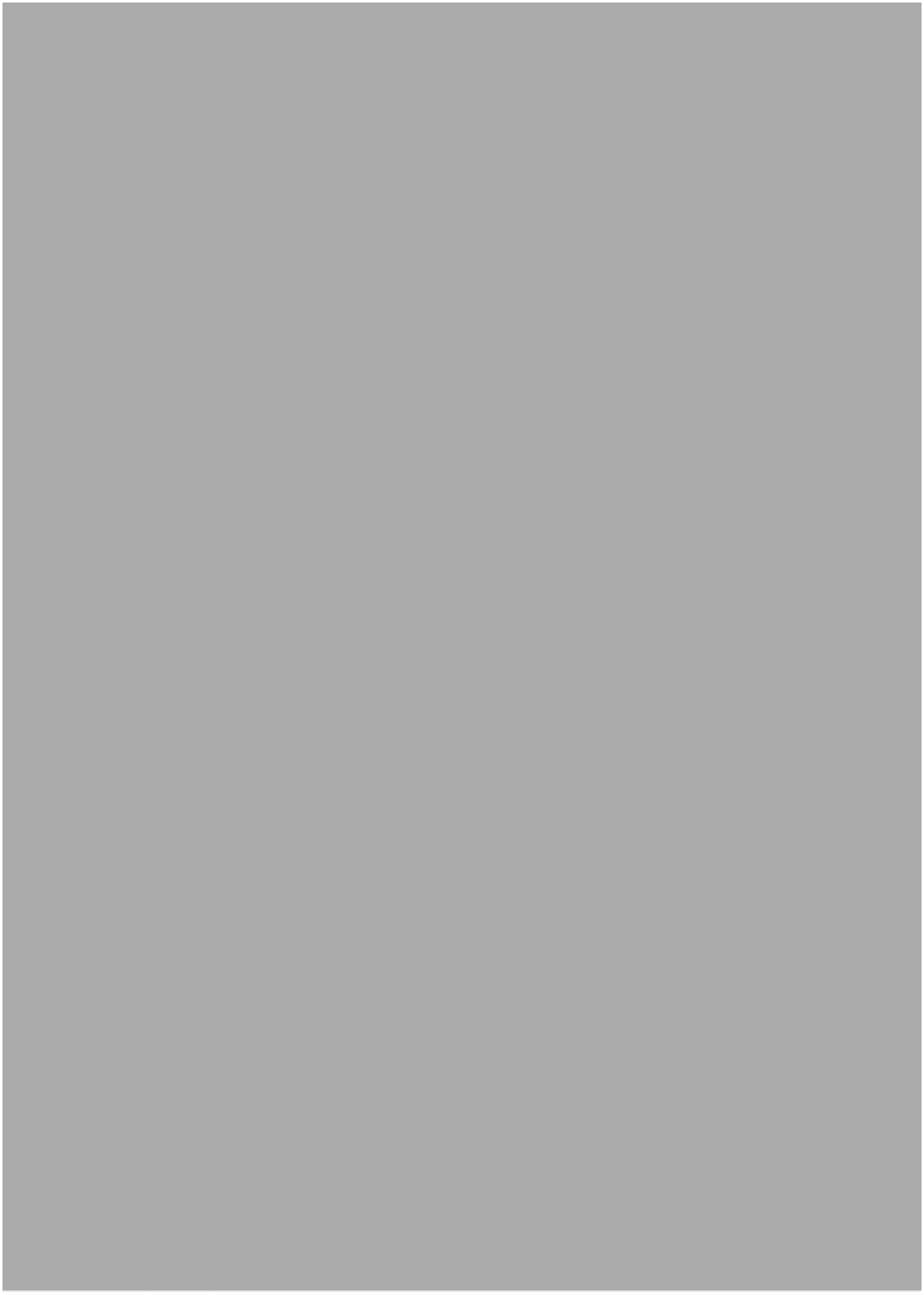

BIBLIOGRAPHY

[1] B. Acikel, T. R. Taylor, P. J. Hansen, J. S. Speck, and R. A. York, "A New High Performance Phase Shifter Using $Ba_xSr_{1-x}TiO_3$ Thin Films," *IEEE Microwave and Wireless Components Letters,* vol. 12, pp. 237-239, 2002.

[2] M. J. Lancaster, J. Powell, and A. Porch, "Thin-film Ferroelectric Microwave Devices," *Superconductor Science & Technology,* vol. 11, pp. 1323-1334, Nov 1998.

[3] I. D. Kim, M. H. Lim, H. G. Kim, K. B. Kim, T. S. Yun, and J. C. Lee, "Ferroelectric Thin-Film-Based Electrically Tunable Bandpass Filters," *Electrochemical and Solid-State Letters,* vol. 5, pp. F25-F28, 2002.

[4] O. G. Vendik, E. K. Hollmann, A. B. Kozyrev, and A. M. Prudan, "Ferroelectric Tuning of Planar and Bulk Microwave Devices," *Journal of Superconductivity,* vol. 12, pp. 325-338, 1999.

[5] S. N. Das, "Quality of a ferroelectric material," *IEEE Transactions on Microwave Theory and Techniques,* vol. 12, p. 440, 1964.

[6] M. DiDomenico, Jr., D. A. Johnson, and R. H. Pantell, "Ferroelectric Harmonic Generator and the Large-Signal Microwave Characteristics of a Ferroelectric Ceramic," *Journal of Applied Physics,* vol. 33, pp. 1697-1706, 1962.

[7] G. Rupprecht and R. O. Bell, "Microwave Losses in Strontium Titanate above the Phase Transition," *Physical Review,* vol. 125, p. 1915, 1962.

[8] W. Kim, M. F. Iskander, and W. D. Palmer, "An Integrated Phased Array Antenna Design Using Ferroelectric Materials and the Continuous Transverse Stub Technology," *IEEE Transactions on Antennas and Propagation,* vol. 54, pp. 3095-3105, 2006.

[9] R. R. Romanofsky, J. T. Bernhard, F. W. van Keuls, F. A. Miranda, G. Washington, and C. Canedy, "K-band Phased Array Antennas Based on $Ba_{0.6}Sr_{0.4}TiO_3$ Thin-film Phase Shifters," *IEEE Transactions on Microwave Theory and Techniques,* vol. 48, pp. 2504-2510, 2000.

[10] J. Stevenson Kenney, Y. Yong Kyu, A. Minsik, M. G. Allen, Z. Zhiyong, W. Xiaoyan, A. Hunt, and K. Dongsu, "Low-Voltage Ferroelectric Phase Shifters From L- to C-Band and Their Applications," *IEEE Aerospace Conference,* p. 9 pp., 2006.

[11] L. Sengupta and S. Sengupta, "Novel Ferroelectric Materials for Phased Array Antennas," *IEEE Transactions on Ultrasonics, Ferroelectrics and Frequency Control,* vol. 44, pp. 792-797, 1997.

[12] A. G. Fox, "An Adjustable Wave-Guide Phase Changer," *Proceedings of the IRE,* vol. 35, p. 1489, 1947.

[13] J. F. White, "High Power, p-i-n Diode Controlled, Microwave Transmission Phase Shifters," *IEEE Transactions on Microwave Theory and Techniques,* vol. 13, p. 233, 1965.

[14] K. M. Johnson, "Microwave Varactor Tuned Transistor Oscillator Design," *IEEE Transactions on Microwave Theory and Techniques,* vol. 14, p. 564, 1966.

[15] R. Jakoby, P. Scheele, S. Muller, and C. Weil, "Nonlinear Dielectrics for Tunable Microwave Components," *15th International Conference on Microwaves, Radar and Wireless Communications,* vol. 2, p. 369, 2004.

[16] O. G. Vendik, I. B. Vendik, and M. A. Nikol'ski, "Comparison of MMIC Phase Shifters Using Figure of Merit as the Main Characteristic," *15th International Conference on Microwaves, Radar and Wireless Communications,* vol. 1, p. 333, 2004.

[17] S. R. Chandler, I. C. Hunter, and J. G. Gardiner, "Active Varactor Tunable Bandpass Filter," *IEEE Microwave and Guided Wave Letters,* vol. 3, p. 70, 1993.

[18] L. Billonnet, B. Jarry, S. E. Sussman-Fort, E. Rius, G. Tanné, C. Person, and S. Toutain, "Recent Advances in Microwave Active Filter Design. Part 2: Tunable Structures and Frequency Control Techniques," *International Journal of RF and Microwave Computer-Aided Engineering,* vol. 12, pp. 177-189, 2002.

[19] J. B. Yoon and C. T. C. Nguyen, "A High-Q Tunable Micromechanical Capacitor with Movable Dielectric for RF Applications," *International Electron Devices Meeting Technical Digest,* p. 489, 2000.

[20] H. Nieminen, V. Ermolov, K. Nybergh, S. Silanto, and T. Ryhanen, "Microelectromechanical Capacitors for RF Applications," *Journal of Micromechanics and Microengineering,* vol. 12, pp. 177-186, 2002.

[21] J. Y. Park, Y. J. Yee, H. J. Nam, and J. U. Bu, "Micromachined RF MEMS Tunable Capacitors Using Piezoelectric Actuators," *IEEE MTT-S International Microwave Symposium Digest,* vol. 3, p. 2111, 2001.

[22] Z. Feng, H. Zhang, K. C. Gupta, W. Zhang, V. M. Bright, and Y. C. Lee, "MEMS-based Series and Shunt Variable Capacitors for Microwave and Millimeter-Wave Frequencies," *Sensors and Actuators A: Physical,* vol. 91, p. 256, 2001.

[23] G. M. Rebeiz, "RF MEMS Switches: Status of the Technology," in *12th International Conference on TRANSDUCERS, Solid-State Sensors, Actuators and Microsystems*, 2003, pp. 1726-1729 vol.2.

[24] E. Marsan, J. Gauthier, M. Chaker, and W. Ke, "Tunable Microwave Device: Status and Perspective," in *The 3rd International IEEE-NEWCAS Conference*, 2005, pp. 279-282.

[25] F. Reggia and E. G. Spencer, "A New Technique in Ferrite Phase Shifting for Beam Scanning of Microwave Antennas," *Proceedings of the IRE,* vol. 45, p. 1510, 1957.

[26] J. D. Adam, L. E. Davis, G. F. Dionne, E. F. Schloemann, and S. N. Stitzer, "Ferrite Devices and Materials," *IEEE Transactions on Microwave Theory and Techniques,* vol. 50, p. 721, 2002.

[27] M. Daglish and T. Kemmitt, "Ferroelectric Thin Films - Research, Development and Commercialisation," *IPENZ Transactions,* vol. 27, 2000.

[28] R. Isom, M. Hawkins, J. Richins, S. McEwan, M. Iskabder, and R. Grow, "Comparative Evaluation of MEMS and Ferroelectric Technologies in Phase Shifter Design," in *IEEE Antennas and Propagation Society International Symposium*, 2000, pp. 808-811 vol.2.

[29] A. A. R. Elshabini-Riad, A. Elshabini, and F. D. Barlow, *Thin Film Technology Handbook*: McGraw-Hill Professional, 1997.

[30] G. M. Rebeiz, *RF MEMS: Theory, Design, and Technology*: John Wiley and Sons, 2003.

[31] R. Romanofsky, J. L. Volakis, R. C. Johnson, and H. Jasik, "Array Phase Shifters: Theory and Technology," in *Antenna Engineering Handbook*, 4 ed: McGraw-Hill Professional, 2007.

[32] A. B. Kozyrev, V. N. Osadchy, and D. M. Kosmin, "L-S Band Module for Phase/Amplitude Processing," *European Radar Conference,* p. 327, 2005.

[33] L. C. Cheng and M. J. Lancaster, "Computation of Parameters of a Ferroelectric-filled Microstrip by Finite Difference Method," *IET Microwaves, Antennas & Propagation,* vol. 1, pp. 453-457, 2007.

[34] A. K. Tagantsev, V. O. Sherman, K. F. Astafiev, J. Venkatesh, and N. Setter, "Ferroelectric Materials for Microwave Tunable Applications," *Journal of Electroceramics,* vol. 11, pp. 5-66, 2003.

[35] C. Paz de Araujo, J. F. Scott, and G. W. Taylor, *Ferroelectric Thin Films: Synthesis and Basic Properties*: Gordon and Breach, 1996.

[36] M. Kamlah, "Ferroelectric and Ferroelastic Piezoceramics – Modeling of Electromechanical Hysteresis Phenomena," *Continuum Mechanics and Thermodynamics,* vol. 13, p. 219, 2001.

[37] T. Remmel, R. Gregory, and B. Baumert, "Characterization of Barium Strontium Titanate Films Using XRD," *International Centre for Diffraction Data,* 1999.

[38] B. J. Kim, S. Baik, Y. Poplavko, Y. Prokopenko, J. Y. Lim, and B. M. Kim, "Epitaxial BSTO Thin Films for Microwave Phase Shifters," *Asia-Pacific Microwave Conference,* pp. 934-937, 2000.

[39] J. B. L. Rao, D. P. Patel, L. C. Sengupta, and J. Synowezynski, "Ferroelectric Materials for Phased Array Applications," *IEEE 1997 Antennas and Propagation Society International Symposium Digest,* vol. 4, pp. 2284-2287 vol.4, 1997.

[40] F. W. Van Keuls, C. T. Chevalier, F. A. Miranda, C. M. Carlson, T. V. Rivkin, P. A. Parilla, J. D. Perkins, and D. S. Ginley, "Comparison of the Experimental Performance of Ferroelectric CPW Circuits with Method-of-Moment Simulations and Conformal Mapping Analysis," *Microwave and Optical Technology Letters,* vol. 29, pp. 34-37, 2001.

[41] P. M. Suherman, T. J. Jackson, Y. Y. Tse, I. P. Jones, R. I. Chakalova, M. J. Lancaster, and A. Porch, "Microwave Properties of $Ba_{0.5}Sr_{0.5}TiO_3$ Thin Film Coplanar Phase Shifters," *Journal of Applied Physics,* vol. 99, p. 104101, 2006.

[42] N. M. Alford, S. J. Penn, A. Templeton, X. Wang, J. C. Gallop, N. Klein, C. Zuccaro, and P. Filhol, "Microwave Dielectrics," *IEE Colloquium on Electro-technical Ceramics - Processing, Properties and Applications,* pp. 9/1-9/5, 1997.

[43] S. J. Penn, N. McNalford, A. Templeton, N. Klein, J. C. Gallop, P. Filhol, and X. Wang, "Low Loss Ceramic Dielectrics for Microwave Filters," *IEE Colloquium on Advances in Passive Microwave Components,* pp. 6/1-6/6, 1997.

[44] S. S. Gevorgian, E. F. Carlsson, S. Rudner, U. Helmersson, E. L. Kollberg, E. Wikborg, and O. G. Vendik, "HTS/Ferroelectric Devices for Microwave Applications," *IEEE Transactions on Applied Superconductivity,* vol. 7, pp. 2458-2461, 1997.

[45] O. G. Vendik, E. Kollberg, S. S. Gevorgian, A. B. Kozyrev, and O. I. Soldatenkov, "1 GHz Tunable Resonator on Bulk Single Crystal STO Plated with YBCO Films," *Electronics Letters,* vol. 31, pp. 654-656, 1995.

[46] T. Chakraborty, I. Hunter, R. Kurchania, A. A. B. A. Bell, and S. Chakraborty, "Intermodulation Distortion in Wide-and Dual-mode Bulk Ferroelectric Bandpass Filters," *IEEE MTT-S International Microwave Symposium Digest,* p. 4 pp., 2005.

[47] M. K. Roy, C. Kalmar, R. R. Neurgaonkar, J. R. Oliver, and D. Dewing, "A Highly Tunable Radio Frequency Filter Using Bulk Ferroelectric Materials," *14th International Symposium on Applications of Ferroelectrics IEEE,* p. 25, 2004.

[48] D. M. Kosmin, V. N. Osadchy, and A. B. Kozyrev, "Switching Time of Bulk Ferroelectric Sandwich Varactors," *17th International Crimean Conference Microwave & Telecommunication Technology,* p. 533, 2007.

[49] J. B. L. Rao, D. P. Patel, and V. Krichevsky, "Voltage-Controlled Ferroelectric Lens Phased Arrays," *IEEE Transactions on Antennas and Propagation,* vol. 47, p. 458, 1999.

[50] K. S. K. Yeo, W. F. Hu, M. J. Lancaster, B. Su, and T. W. Button, "Thick Film Ferroelectric Phase Shifters Using Screen Printing Technology," in *34th European Microwave Conference*, 2004, pp. 1489-1492.

[51] W. Hu, D. Zhang, M. J. Lancaster, K. S. K. Yeo, T. W. Button, and B. Su, "Cost Effective Ferroelectric Thick Film Phase Shifter based on Screen-Printing Technology," *IEEE MTT-S International Microwave Symposium Digest,* pp. 591-594, 2005.

[52] W. Hu, D. Zhang, M. J. Lancaster, T. W. A. B. T. W. Button, and B. A. S. B. Su, "Investigation of Ferroelectric Thick-Film Varactors for Microwave Phase Shifters," *Microwave Theory and Techniques, IEEE Transactions on,* vol. 55, pp. 418-424, 2007.

[53] P. Scheele, S. Muller, C. Weil, and R. Jakoby, "Phase-shifting Coplanar Stubline-Filter on Ferroelectric-Thick Film," *34th European Microwave Conference,* vol. 3, pp. 1501-1504, 2004.

[54] M. Ohring, *Materials Science of Thin Films: Deposition and Structure*, 2nd ed.: Academic Press, 2002.

[55] W. T. Chang, S. W. Kirchoefer, J. A. Bellotti, and J. M. Pond, "(Ba,Sr)TiO_3 Ferroelectric Thin Films for Tunable Microwave Applications," *Revista Mexicana De Fisica,* vol. 50, pp. 501-505, 2004.

[56] C. L. Chen, J. Shen, S. Y. Chen, G. P. Luo, C. W. Chu, F. A. Miranda, F. W. V. Keuls, J. C. Jiang, E. I. Meletis, and H. Y. Chang, "Epitaxial Growth of Dielectric BSTO Thin Film on MgO for Room Temperature Microwave Phase Shifters," *Applied Physics Letters,* vol. 78, pp. 652-654, 2001.

[57] J. Kim, I. K. Yu, S. J. Lee, and K. Y. Kang, "Growth and Characterization of BSTO and YBCO/BSTO Thin Films on MgO (100) Substrates," *Journal of the Korean Physical Society,* vol. 32, pp. 183-185, 1998.

[58] J. Zhang, H. Zhang, K. J. Chen, S. G. Lu, and Z. Xu, "Microwave Performance Dependence of BST Thin Film Planar Interdigitated Varactors on Different substrates," in *2nd IEEE International Conference on Nano/Micro Engineered and Molecular Systems*, 2007, pp. 678-682.

[59] E. G. Erker, A. S. Nagra, L. Yu, P. Periaswamy, T. R. Taylor, J. Speck, and R. A. York, "Monolithic Ka-band Phase Shifter using Voltage Tunable BaSrTiO Parallel Plate Capacitors," *IEEE Microwave and Guided Wave Letters,* vol. 10, pp. 10-12, 2000.

[60] S. W. Kirchoefer, J. M. Pond, A. C. Carter, W. Chang, K. K. Agarwal, J. S. Horwitz, and D. B. Chrisey, "Microwave Properties of $Sr_{0.5}Ba_{0.5}TiO_3$ Thin-film Interdigitated

Capacitors," *Microwave and Optical Technology Letters,* vol. 18, pp. 168-171, 1998.

[61] F. A. Miranda, C. H. Mueller, C. D. Cubbage, K. B. Bhasin, R. K. Singh, and S. D. Harkness, "HTS/ferroelectric Thin Films for Tunable Microwave Components," *IEEE Transactions on Applied Superconductivity,* vol. 5, pp. 3191-3194, 1995.

[62] A. Tombak, F. Tito Ayguavives, J. P. Maria, G. T. Stauf, A. I. Kingon, and A. Mortazawi, "Low Voltage Tunable Barium Strontium Titanate Thin Film Capacitors for RF and Microwave Applications," *IEEE MTT-S International Microwave Symposium Digest,* vol. 3, pp. 1345-1348 vol.3, 2000.

[63] Y. Wang, N. Chong, Y. L. Cheng, H. L. W. Chan, and C. L. Choy, "Dependence of Capacitance on Electrode Configuration for Ferroelectric Films with Interdigital Electrodes," *Microelectronic Engineering,* vol. 66, pp. 880-886, 2003.

[64] H. D. Wu, Z. Zhang, F. Barnes, C. M. Jackson, A. Kain, and J. D. Cuchiaro, "Voltage Tunable Capacitors Using High Temperature Superconductors and Ferroelectrics," *IEEE Transactions on Applied Superconductivity,* vol. 4, pp. 156-160, 1994.

[65] B. Xu, R. G. Polcawich, S. Trolier-McKinstry, Y. Ye, L. E. Cross, J. J. Bernstein, and R. Miller, "Sensing Characteristics of In-plane Polarized Lead Zirconate Titanate Thin Films," *Applied Physics Letters,* vol. 75, pp. 4180-4182, 1999.

[66] I. Vendik, V. Pleskachev, and O. Vendik, "Figure of Merit and Limiting Characteristics of Tunable Ferroelectric Microwave Devices," in *Progress in Electromagnetics Research Symposium* Hangzhou, China, 2005, pp. 1-4.

[67] V. O. Sherman, T. Yamada, A. Noeth, N. Setter, M. Mandeljc, B. Malic, M. Kosec, and M. Vukadinovic, "Microwave Phase Shifters Based on Sol-Gel Derived $Ba_{0.3}Sr_{0.7}TiO_3$ Ferroelectric Thin Films," *European Microwave Conference,* pp. 1295-1298, 2007.

[68] O. G. Vendik, E. F. Carlsson, P. K. Petrov, R. A. Chakalov, S. S. Gevorgian, and Z. G. Ivanov, "HTS/Ferroelectric CPW Structures for Voltage Tuneable Phase Shifters," in *27th European Microwave Conference*, 1997, pp. 196-202.

[69] V. Sherman, K. Astafiev, A. Tagantsev, N. Setter, I. Vendik, and O. Vendik, "Design and Investigation of Ferroelectric Digital Phase Shifter," *31st European Microwave Conference,* pp. 1-4, 2001.

[70] B. H. Moeckly and Y. Zhang, "Strontium Titanate Thin Films for Tunable $YBa_2Cu_3O_7$ Microwave Filters," *IEEE Transactions on Applied Superconductivity,* vol. 11, pp. 450-453, 2001.

[71] G. Subramanyam, F. W. Van Keuls, and F. A. Miranda, "A K-band-frequency Agile Microstrip Bandpass Filter Using a Thin-film HTS/Ferroelectric/Dielectric Multilayer Configuration," *IEEE Transactions on Microwave Theory and Techniques,* vol. 48, pp. 525-530, 2000.

[72] I. Vendik, O. Vendik, V. Pleskachev, and M. Nikol'ski, "Tunable Microwave Filters Using Ferroelectric Materials," *IEEE Transactions on Applied Superconductivity,* vol. 13, pp. 716-719, 2003.

[73] V. Pleskachev and I. Vendik, "Figure of Merit of Tunable Ferroelectric Planar Filters," in *The 5th International Kharkov Symposium on Physics and Engineering of Microwaves, Millimeter, and Submillimeter Waves*, 2004, pp. 697-699 Vol.2.

[74] R. N. Simons, *Coplanar Waveguide Circuits, Components, and Systems*, 1st ed.: Wiley-

Interscience, 2001.

[75] C.-C. Tien, C. K. C. Tzuang, S. T. Peng, and C.-C. Chang, "Transmission Characteristics of Finite-Width Conductor-Backed Coplanar Waveguide," *IEEE Transactions on Microwave Theory and Techniques,* vol. 41, p. 1616, 1993.

[76] J.-S. Hong and M. J. Lancaster, *Microstrip Filters for RF/Microwave Applications*: John Wiley & Sons, 2001.

[77] K. C. Gupta, R. Garg, and I. J. Bahl, *Microstrip Lines and Slotlines*, 2nd ed. Norwood, MA: Artech House, Inc., 1996.

[78] E. Hammerstad and O. Jensen, "Accurate Models for Microstrip Computer-Aided Design," in *Microwave Symposium Digest, 1980 MTT-S International*, 1980, pp. 407-409.

[79] J. Svacina, "Analysis of Multilayer Microstrip Lines by a Conformal Mapping Method," *IEEE Transactions on Microwave Theory and Techniques,* vol. 40, p. 769, 1992.

[80] Sonnet Simulation Tools, *Sonnet Software*. Syracuse, NY, 2007.

[81] A. Weisshaar and V. K. Tripathi, "Perturbation Analysis and Modeling of Curved Microstrip Bends," *IEEE Transactions on Microwave Theory and Techniques,* vol. 38, p. 1449, 1990.

[82] R. J. P. Douville and D. S. James, "Experimental-Study Of Symmetric Microstrip Bends And Their Compensation," *IEEE Transactions on Microwave Theory And Techniques,* vol. 26, pp. 175-182, 1978.

[83] R. Chadha and K. C. Gupta, "Compensation Of Discontinuities In Planar Transmission-Lines," *IEEE Transactions on Microwave Theory And Techniques,* vol. 30, pp. 2151-2156, 1982.

[84] S. Gevorgian, L. J. P. Linner, and E. L. Kollberg, "CAD Models for Shielded Multilayered CPW," *IEEE Transactions on Microwave Theory and Techniques,* vol. 43, p. 772, 1995.

[85] C. Veyres and V. F. Hanna, "Extension of the Application of Conformal Mapping Techniques to Coplanar Lines with Finite Dimensions," *International Journal of Electronics,* vol. 48, pp. 47 - 56, 1980.

[86] S. Gevorgian, T. Martinsson, A. Deleniv, E. Kollberg, and I. Vendik, "Simple and Accurate Dispersion Expression for the Effective Dielectric Constant of Coplanar Waveguides," *IEE Proceedings Microwaves, Antennas and Propagation,* vol. 144, pp. 145-148, 1997.

[87] D. Harvey, "A Lumped Coplanar to Microstrip Transition Model for De-Embedding S-Parameters Measured on GAAS Wafers," *29th ARFTG Conference Digest-Spring,* vol. 11, p. 204, 1987.

[88] W. Wiatr, D. K. Walker, and D. F. Williams, "Coplanar-Waveguide-to-Microstrip Transition Model," *IEEE MTT-S International Microwave Symposium Digest,* vol. 3, p. 1797, 2000.

[89] L. Zhu, K. L. Melde, and J. L. Prince, "A Broadband CPW-to-Microstrip Via-less Transition for on Wafer Package Probing Applications," *Electrical Performance of Electronic Packaging,* p. 75, 2003.

[90] A. M. E. Safwata, K. A. Zaki, W. Johnson, and C. H. Lee, "Novel Design for Coplanar Waveguide to Microstrip Transition," *IEEE MTT-S International Microwave Symposium Digest,* vol. 2, p. 607, 2001.

[91] J. P. Raskin, G. Gauthier, L. P. Katehi, and G. M. Rebeiz, "Mode Conversion at GCPW-to-Mmicrostrip-Line Transitions," *IEEE Transactions on Microwave Theory and Techniques,* vol. 48, p. 158, 2000.

[92] D. F. Williams and T. H. Miers, "A Coplanar Probe to Microstrip Transition," *IEEE Transactions on Microwave Theory and Techniques,* vol. 36, p. 1219, 1988.

[93] G. Zheng, J. Papapolymerou, and M. M. Tentzeris, "Wideband Coplanar Waveguide RF Probe Pad to Microstrip Transitions Without Via Holes," *IEEE Microwave and Wireless Components Letters,* vol. 13, p. 544, 2003.

[94] Y. Wang and M. J. Lancaster, "Coplanar to Microstrip Transitions for On-wafer Measurements," *Microwave and Optical Technology Letters,* vol. 49, pp. 100-103, 2007.

[95] R. E. Collin, *Foundations for Microwave Engineering*, 2nd ed.: Wiley - Interscience, 2001.

[96] R. A. Pucel, D. J. Masse, and C. P. Hartwig, "Losses in Microstrip," *IEEE Transactions on Microwave Theory and Techniques,* vol. 16, pp. 342-350, 1968.

[97] G. Ghione, "A CAD-oriented Analytical Model for the Losses of General Asymmetric Coplanar Lines in Hybrid and Monolithic MICs," *IEEE Transactions on Microwave Theory and Techniques,* vol. 41, pp. 1499-1510, 1993.

[98] Y. Wang, "Superconducting Coplanar Delay Lines," in *Electronic, Electrical and Computer Engineering*. vol. Doctor of Philosophy Birmingham: University of Birmingham, 2005.

[99] S. S. Gevorgian, D. I. Kaparkov, and O. G. Vendik, "Electrically Controlled HTSC/Ferroelectric Coplanar Waveguide," *IEE Proceedings on Microwaves, Antennas and Propagation,* vol. 141, pp. 501-503, 1994.

[100] M. Y. Frankel, S. Gupta, J. A. Valdmanis, and G. A. Mourou, "Terahertz Attenuation and Dispersion Characteristics of Coplanar Transmission Lines," *IEEE Transactions on Microwave Theory and Techniques,* vol. 39, pp. 910-916, 1991.

[101] D. Grischkowsky, I. N. Duling Iii, J. C. Chen, and C. C. Chi, "Electromagnetic Shock Waves from Transmission Lines," *Physical Review Letters,* vol. 59, p. 1663, 1987.

[102] G. E. Ponchak, J. Papapolymerou, and M. M. Tentzeris, "Excitation of Coupled Slotline Mode in Finite-Ground CPW with Unequal Ground-Plane Widths," *IEEE Transactions on Microwave Theory and Techniques,* vol. 53, pp. 713-717, 2005.

[103] R. N. Simons and G. E. Ponchak, "Modeling of Some Coplanar Waveguide Discontinuities," *IEEE Transactions on Microwave Theory and Techniques,* vol. 36, pp. 1796-1803, 1988.

[104] M. F. Wong, O. Picon, and V. F. Hanna, "Spurious-free Finite Element Analysis of Multiaxial Coplanar Waveguide Discontinuities," in *European Microwave Conference, 1993. 23rd*, 1993, pp. 334-337.

[105] T. Becks and I. Wolff, "Full-Wave Analysis of Various Coplanar Bends and T-Junctions with Respect to Different Types of Air-Bridges," in *IEEE MTT-S International Microwave Symposium Digest*, 1993, pp. 697-700 vol.2.

[106] W. H. Haydl, "On the Use of Vias in Conductor-Backed Coplanar Circuits," *IEEE Transactions on Microwave Theory and Techniques,* vol. 50, pp. 1571-1577, 2002.

[107] M. Yu, R. Vahldieck, and J. Huang, "Comparing Coax Launcher and Wafer Probe Excitation for 10 mil Conductor Backed CPW with Via Holes and Airbridges," in *IEEE*

MTT-S International Microwave Symposium Digest, 1993, pp. 705-708 vol.2.

[108] R. Ott and R. Wordenweber, "Improved Designs of Tunable Ferroelectric Capacities for Microwave Applications," *Applied Physics Letters,* vol. 80, pp. 2150-2152, 2002.

[109] H. T. Su, M. J. Lancaster, F. Huang, and F. Wellhofer, "Electrically Tunable Superconducting Quasi-lumped Element Resonator Using Thin-Film Ferroelectrics," *Microwave and Optical Technology Letters,* vol. 24, pp. 155-158, 2000.

[110] M. F. Iskander, M. D. Morrison, W. C. Datwyler, and M. S. Hamilton, "A New Course on Computational Methods in Electromagnetics," *IEEE Transactions on Education,* vol. 31, pp. 101-115, 1988.

[111] F. Sandy and J. Sage, "Use of Finite Difference Approximations to Partial Differential Equations for Problems Having Boundaries at Infinity (Correspondence)," *IEEE Transactions on Microwave Theory and Techniques,* vol. 19, pp. 484-486, 1971.

[112] M. V. Schneider, "Computation of Impedance and Attenuation of TEM-Lines by Finite Difference Methods," *IEEE Transactions on Microwave Theory and Techniques,* vol. 13, pp. 793-800, 1965.

[113] D. H. Sinnott, G. K. Cambrell, C. T. Carson, and H. E. A. G. H. E. Green, "The Finite Difference Solution of Microwave Circuit Problems," *IEEE Transactions on Microwave Theory and Techniques,* vol. 17, pp. 464-478, 1969.

[114] J. W. Duncan, "The Accuracy of Finite-Difference Solutions of Laplace's Equation," *Microwave Theory and Techniques, IEEE Transactions on,* vol. 15, pp. 575-582, 1967.

[115] H. E. Stinehelfer, "An Accurate Calculation of Uniform Microstrip Transmission Lines," *IEEE Transactions on Microwave Theory and Techniques,* vol. 16, pp. 439-444, 1968.

[116] M. J. Beaubien and A. Wexler, "Unequal-Arm Finite-Difference Operators in the Positive-Definite Successive Overrelaxation (PDSOR) Algorithm," *IEEE Transactions on Microwave Theory and Techniques,* vol. 18, pp. 1132-1149, 1970.

[117] B. A. Carre, "The Determination of the Optimum Accelerating Factor for Successive Over-relaxation," *The Computer Journal,* vol. 4, pp. 73-78, 1961.

[118] A. Wexler, "Computation of Electromagnetic Fields," *IEEE Transactions on Microwave Theory and Techniques,* vol. 17, pp. 416-439, 1969.

[119] Y. C. Sung, S. Choi, and S. Nam, "Finite Element Analysis of Microstrip Line on Ferroelectric (Ba-Sr)TiO_3 Substrate," in *IEEE MTT-S International Microwave Symposium Digest*, 1995, pp. 1261-1264 vol.3.

[120] K.-B. Kim, T.-S. Yun, J.-C. Lee, H.-S. Kim, H.-G. Kim, and I.-D. Kim, "Integration of Coplanar (Ba,Sr)TiO_3 Microwave Phase Shifters onto Si Wafers TiO_2 Buffer Layers," *IEEE Transactions on Ultrasonics, Ferroelectrics and Frequency Control,* vol. 53, pp. 518-524, 2006.

[121] A. M. E. Safwat and L. Hayden, "Sensitivity Analysis of Calibration Standards for SOLT and LRRM," in *ARFTG Conference Digest-Fall, 58th*, 2001, pp. 1-10.

[122] Y. C. Shih and M. Maher, "Characterization of Conductor-Backed Coplanar Waveguide Using Accurate On-Wafer Measurement Techniques," in *IEEE MTT-S International Microwave Symposium Digest*, 1990, pp. 1129-1132 vol.3.

[123] F. Zimmermann, M. Voigts, C. Weil, R. Jakoby, P. Wang, W. Menesklou, and E. Ivers-

Tiffée, "Investigation of Barium Strontium Titanate Thick Films for Tunable Phase Shifters," *Journal of the European Ceramic Society,* vol. 21, pp. 2019-2023, 2001.

[124] H.-T. Lue and T.-Y. Tseng, "Application of On-wafer TRL Calibration on the Measurement of Microwave Properties of $Ba_{0.5}Sr_{0.5}TiO_3$ Films," *IEEE Transactions on Ultrasonics, Ferroelectrics and Frequency Control,* vol. 48, p. 1640, 2001.

[125] Z. Wang, J. Liu, T. Ren, L. Liu, and Z. Li, "$Ba_{0.5}Sr_{0.5}TiO_3$ Ferroelectric Thick Films with Uniform Thickness and its Applications to RF MEMS Devices," in *Proceedings of the 13th IEEE International Symposium on Applications of Ferroelectrics*, 2002, pp. 475-478.

[126] M. Ouaddari, S. Delprat, F. Vidal, M. Chaker, and W. Ke, "Microwave Characterization of Ferroelectric Thin-Film Materials," *IEEE Transactions on Microwave Theory and Techniques,* vol. 53, pp. 1390-1397, 2005.

[127] S. W. Kirchoefer, J. M. Pond, H. S. Newman, K. Won-Jeong, and J. S. Horwitz, "Ferroelectric-Ferrite Tunable Phase Shifters," in *IEEE MTT-S International Microwave Symposium Digest*, 2000, pp. 1359-1362 vol.3.

[128] A. Kozyrev, V. Osadchy, A. Pavlov, and L. Sengupta, "Application of Ferroelectrics in Phase Shifter Design," in *IEEE MTT-S International Microwave Symposium Digest*, 2000, pp. 1355-1358 vol.3.

[129] D. Kim, Y. Choi, M. G. Allen, J. S. Kenney, and D. Kiesling, "A Wide-Band Reflection-Type Phase Shifter at S-band using BST Coated Substrate," *IEEE Transactions on Microwave Theory and Techniques,* vol. 50, pp. 2903-2909, 2002.

[130] Glass Dynamics, "Pyrex® Corning 7740," New Jersey, USA: http://www.glassdynamicsllc.com/Pyrex%20Corning%207740.htm.

[131] MTI Corporation, "Lanthanum Aluminate, $LaAlO_3$, <100>orn. 10x10x1.0 mm substrate," California, USA: http://www.mtixtl.com/index.asp?PageAction=VIEWPROD&ProdID=483.

[132] SPI Supplies, "Magnesium Oxide Single Crystal Substrates, MgO (100) Substrate 10x10 x0.5 mm," Pennsylvania, USA: http://www.2spi.com/catalog/submat/magnesium-oxide.shtml.

[133] M. M. Tomeh, S. Goasguen, and S. M. El-Ghazaly, "Time Domain Optical Response of Electro-Optic Modulator using FDTD," in *IEEE MTT-S International Microwave Symposium Digest*, 2001, pp. 1049-1052 vol.2.

[134] C. M. Chorey, A. Ferendici, and K. Bhasin, "A High Frequency GaAlAs Travelling Wave Electro-Optic Modulator at 0.82 um," in *IEEE MTT-S International Microwave Symposium Digest*, 1988, pp. 735-738 vol.2.

[135] S. Gille, R. Radouani, J. P. Salvestrini, F. Abdi, L. Guilbert, and M. D. Fontana, "Optimization of Integrated Mach-Zehnder Interferometer Modulator: Electrical and Optical Studies," in *Conference on Lasers and Electro-Optics Europe*, 2003, p. 279.

[136] E. J. Wilkinson, "An N-Way Hybrid Power Divider," *IEEE Transactions on Microwave Theory and Techniques,* vol. 8, p. 116, 1960.

[137] D. M. Pozar, *Microwave Engineering*, 2nd ed.: New York: Wiley, 1998.

[138] H. A. Wheeler, "Formulas for the Skin Effect," *Proceedings of the IRE,* vol. 30, pp. 412-424, 1942.